# Deep implant localization and uplink data telemetry using ultrasound

Indulakshmi Subramaniam

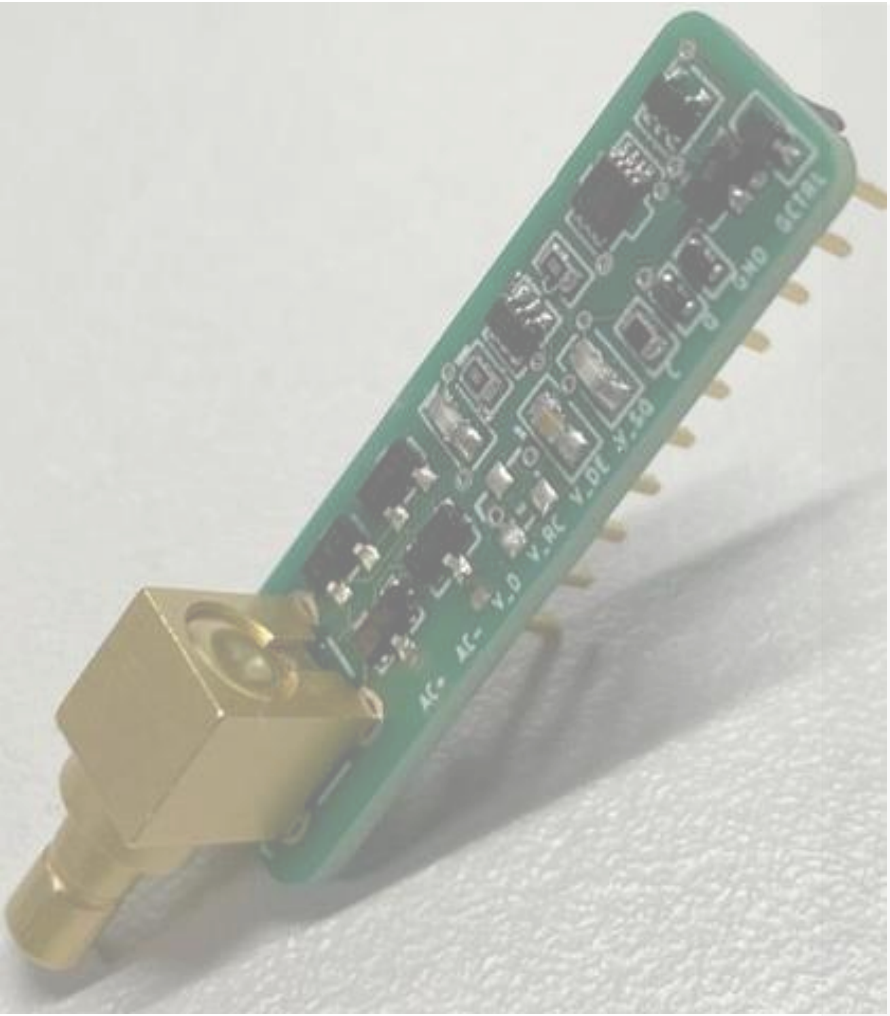

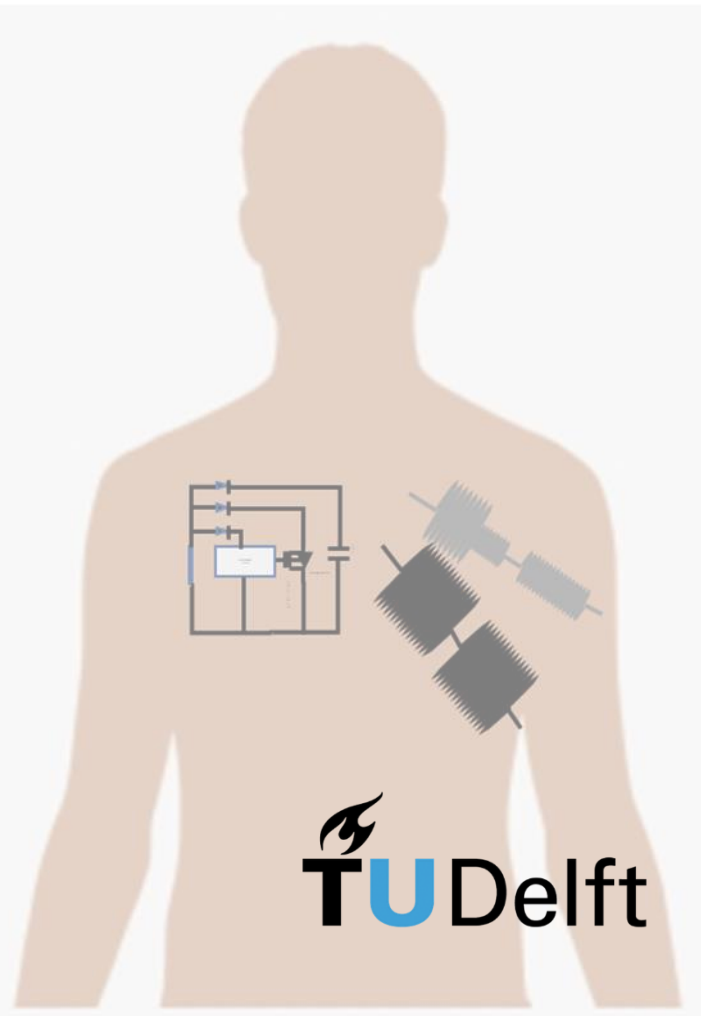

# Deep implant localization and uplink data telemetry using ultrasound

by

Indulakshmi Subramaniam

to obtain the degree of Master of Science at the Delft University of Technology, to be defended publicly on Friday August 27, 2021 at 2:00 PM.

| | | |
|---|---|---|
| Student number: | 4932846 | |
| Project duration: | October 15, 2020 - August 27, 2021 | |
| Supervisors: | Prof. dr. ir. Ronald Dekker, | TU Delft and Philips |
| | Ir. Shinnosuke. Kawasaki, | TU Delft |
| Thesis committee: | Prof. dr. ir. Ronald Dekker, | TU Delft and Philips |
| | Prof. dr. ir. Paddy French, | TU Delft |
| | Ir. Shinnosuke. Kawasaki, | TU Delft |



TU Delft

# Abstract

Active implantable devices are conventionally powered with batteries. The miniaturisation of implants necessitates the need to find an efficient way to transfer power wirelessly. Ultrasound energy transfer with its short wavelength, small receiving transducer size, beam forming capability make deep tissue penetration possible making it a good alternative for powering deep implants. There is also the advantage of using the reflected energy (ultrasound echo) from the implants to perform passive uplink data telemetry. The ultrasound power transfer efficiency depends on how well the energy is focused onto the implant. So, the implant needs to be located first and then an initial contact needs to be established that can then be used to fine tune beam forming attributes such as focus depth and steering angle.

In this work, a simple low power uplink data telemetry circuit to establish the 'first contact' that sends information on implant's energy status to the transmitter is designed. The telemetry uses load impedance modulation to passively transmit back information. This principle is tested using an experimental setup with a 4 MHz burst frequency and different resistive loads varied from 0 $\Omega$ to 2000 $\Omega$. Next, an algorithm was developed that automatically finds the optimal focus and steering angle settings so that the maximum amount of power is transferred to the ultrasound energy scavenger. This algorithm works based on the information sent from the uplink data telemetry circuit.

The results show that load impedance modulation can effectively be used for backscatter communication. A reflected energy change of upto 40% is observed between matched and mismatched load conditions. This load modulation was implemented in the uplink data telemetry circuit. A simple low power circuit that consumes less than 0.5 µW was designed for this. The uplink telemetry protocol uses pulse width modulation to send the storage capacitor voltage which powers the implant, and an almost linear correlation was found between the pulse width and the supply voltage. The algorithm produces a heat plot showing the maximum power transferred at the location where CMUT was placed and gives the optimal value of focus and steering angle.

**Keywords : uplink, ultrasound, focus, steer, load modulation, pulse width**

# Acknowledgments

I would like to thank my thesis supervisor, Ronald for his guidance and support throughout the project. Your suggestions have been invaluable to my work. I have learnt a lot from you and you are an incredible mentor. Thanks for being patient with me and for giving me an opportunity to do a thesis with Philips research. I have enjoyed all our conversations from your µtracer to the spin wheel that I went in.

A debt of gratitude to my daily supervisor, Shinnosuke Kawasaki who has taught and helped me throughout the year. I learnt a lot from you and thanks for always taking the time to answer all my questions. I also have enjoyed our conversations at HTC during lunchtimes.

I thank Raja for helping me understand the Verasonic and giving me suggestions that improved my work. I am grateful to you for the time you spent teaching me. I also thank Youri who guided me in the beginning and being helpful.

Eugene, you have made my days in Philips cheerful. You have always checked on us and make jokes that make our day. Also, thanks for all the baked cakes that you gave me to taste :).

I would like to acknowledge Marion, Hans, Johan who helped me with all the administrative processes and also for all the good conversations. I am also grateful to Frank and Maarten for recommending tips for my project.

I want to thank Jia-Jun for being such a good friend and who has always been very supportive, I will miss our coffee breaks. I also want to thank Jian, Marta, Dino, Eric, Sevda who were great company during my time at Philips.

Last and most importantly, my Amma, Appa, Kishore and Hemanth always had faith in me and have constantly encouraged me to be better every day. I also thank all my friends from Delft who has made my stay in the Netherlands enjoyable and colourful.

*Indulakshmi Subramaniam*
*August, 2021*

# Contents

# List of Figures

# List of Tables

# 1 Introduction

**Keywords:** implantable device, wireless power transfer, backscattered ultrasound, beamforming.

## 1.1. Active implantable biomedical devices

The development of sub-millimeter sized implantable devices has gained traction over the recent years. Some of them include vagus nerve stimulators, deep brain stimulators and gut biosensors [34]. Figure 1.1 shows an example of such an active implantable device.

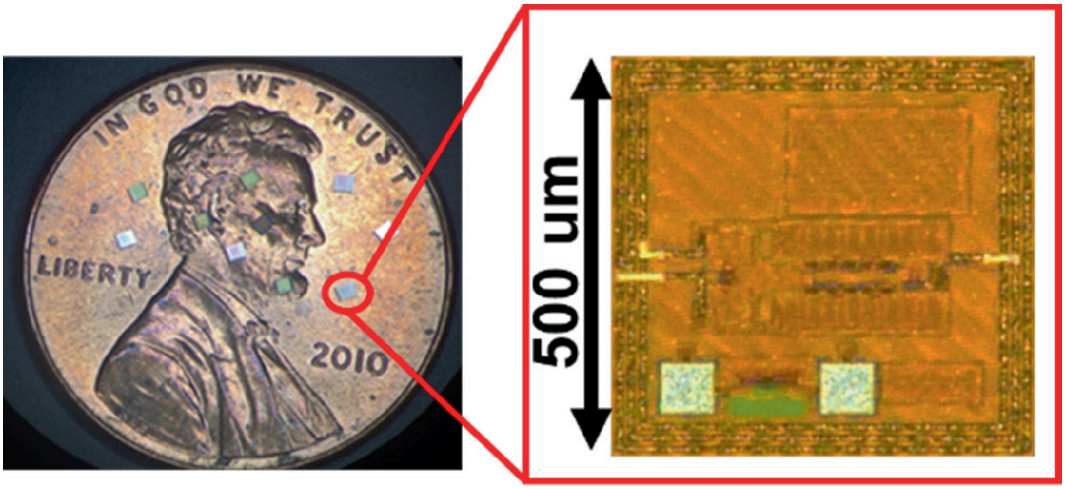


Figure 1.1: Example of an active implantable sub-millimeter sized device [1].

Conventionally, active implantable biomedical devices have been powered by batteries which can occupy up to 80% of the volume of the implant [35], [36]. Apart from this, battery depletion requires surgical intervention for replacement that causes discomfort [37]. These issues can be resolved by various alternatives such as finding an alternative storage element to power the implant or an efficient way to wirelessly transfer power. Powering implants wirelessly is an option that can be considered to reduce the size of the implant and at the same time provide data telemetry.

## 1.2. Biophysics of ultrasound

Ultrasound waves are pressure waves with a frequency above 20 kHz [38]. The interaction between ultrasound waves and biological tissues in human body can cause effects such as absorption, reflection, refraction and scattering that forms the fundamentals for imaging, power transfer and therapeutic applications [39]. Reflected ultrasound waves are termed as echo or backscattered ultrasound. Ultrasound energy harvesters absorb ultrasound for powering deep implants. Biological tissues and water molecules inside the body can absorb/scatter ultrasound causing attenuation [40]. Due to this, the amplitude of ultrasound waves decrease with distance.

### 1.2.1. Acoustic waveforms

Ultrasound waves have two generation modes, namely, continuous wave ultrasound (CW) and pulse wave ultrasound (PW) [41]. In CW, ultrasound is continuously generated at a certain frequency. In PW, ultrasound is generated for a short time duration with a long repetition time. In both modes, an electrical signal with a specific amplitude at a certain frequency is given to an external ultrasound transducer which generates the ultrasound waves. For power transfer, pulsed wave ultrasound is generally used as it can be easily used for backscatter communication and will have lower thermal effects on body tissues compared to continuous wave . Also known as bursts, high frequency sine waves repeat for ‘n’ number of pulse cycles existing for a short duration; for example, see Fig.1.2.

- **Pulse Repetition Time (PRT)**
  It is the time duration between two consecutive burst signals [42]. Pulse repetition frequency (PRF) is the reciprocal of PRT.

- **Pulse period**
  The time taken for one cycle to occur is called the pulse period. It is the reciprocal of ultrasound frequency (f).

- **Pulse cycles**
  The total number of pulses in a burst is termed as the number of pulse cycles (n).

- **Pulse duration**
  If the number of pulse cycle is ’n’ and the time taken by each cycle is the time period given by ’T’, then the pulse duration ($\tau$) is given by by Eqn.1.1.

$$\tau = n * T \tag{1.1}$$

- **Duty factor**
  The duty factor is the ratio of one burst duration to the pulse repetition time, see Eqn.1.2.

$$\begin{aligned} DF &= \tau / PRT \\ &= \tau * PRF \end{aligned} \tag{1.2}$$

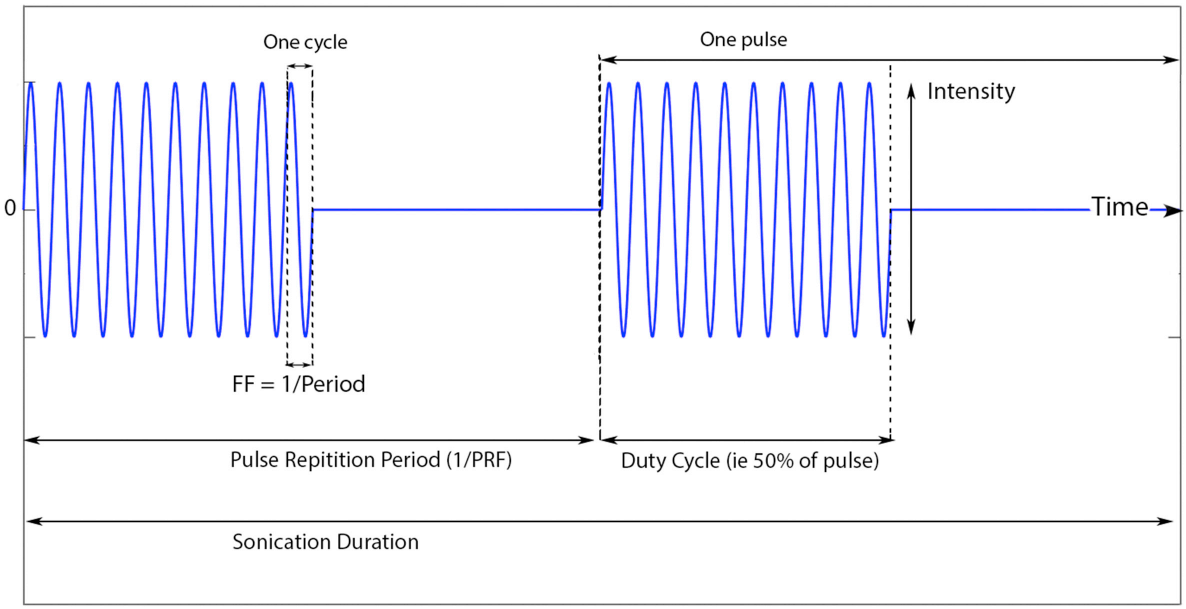


Figure 1.2: Representation of a sinusoidal ultrasound burst signal [2].

In this work, a 4 MHz sine wave of 24 pulse cycles with a 1 ms pulse repetition frequency is used. This frequency was chosen due to external transducer having frequency range of 4-7 MHz and the CMUT can work well between 3-9 MHz. Pulse number was set to maximum possible (24) and longer burst lengths are preferred as it facilitates modulation (PWM). The pulse repetition frequency of 1 ms was chosen such that external movements did not interfere with the communication using backscattered ultrasound.

### 1.2.2. Acoustic impedance and intensity

The acoustic impedance mismatch of a material is the resistance of particles to get displaced due to propagation of an ultrasound wave [43]. This impedance depends on the material density ($\rho$) as well as the velocity of wave propagation (C). The acoustic impedance (Z) is given by Eqn.1.3.

$$Z = \rho C \tag{1.3}$$

If the acoustic impedance between the interface of two mediums is high, then there will be more reflection and less transmission [44]. The transmission coefficient (T) is defined as Eqn.1.4 [45].

$$T = \frac{p_t}{p_i} = \frac{2Z_2}{(Z_2 + Z_1)} \tag{1.4}$$

where $p_t$ is transmitted wave pressure and $p_i$ is the incident wave pressure. Theoretically, the reflection coefficient (R) is given by Eqn.1.5 [45].

$$R = \frac{p_r}{p_i} = \frac{(Z_2 - Z_1)}{(Z_2 + Z_1)} \tag{1.5}$$

where Z1 and Z2 represents the acoustic impedance (Pa·s/m$^3$) of medium 1 and 2 respectively.

Acoustic intensity is the average power over an area that is perpendicular to the direction of wave propagation, it is given by Eqn.1.6 [46], [45], [47].

$$I = p^2/2Z \tag{1.6}$$

In terms of intensity, the reflection coefficient is given by Eqn.1.7 [45].

$$\alpha = \frac{I_r}{I_i} = \frac{(Z_2 - Z_1)^2}{(Z_2 + Z_1)^2} \tag{1.7}$$

### 1.2.3. Ultrasound beamforming

Beamforming is the spatial distribution of a signal from a sensor or sensor array [48], [49]. Ultrasound beamforming is primarily performed to improve the imaging quality. It involves changing the depth and angular parameters of the ultrasound beam. In ultrasound terms, they are called the focus and steer parameters of the beam. Fine tuning of transmit beamforming parameters is essential to transfer maximum power towards the implant. Beamforming essentially has to do with the shaping of the spatial distribution of the acoustic pressure in the region of interest and the subsequent recombination of the received ultrasound echoes for image reconstruction and in this particular case, for establishing an efficient ultrasonic power link [50]. Beamforming helps to improve lateral and axial resolution. The acoustic field intensity profile for a rectangular linear array beamformed at the natural focus is illustrated in Fig.1.3.

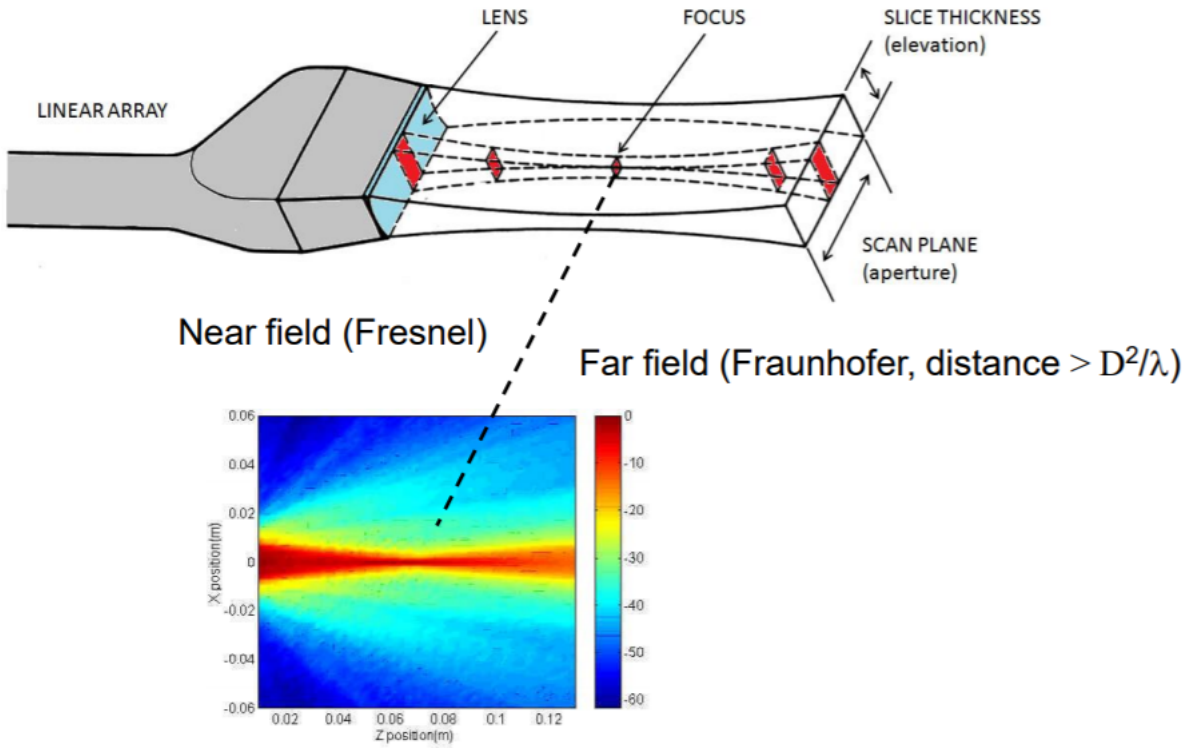


Figure 1.3: Linear array probe with pressure field at different focal zones: the beamwidth is large in pre-focal and post-focal zones, it is the narrowest at the point of natural focus [3].

## Transmit focusing

Focusing is performed to increase the power density at the location of the target. This reduces the beamwidth in the region of interest. Focusing is the result of constructive interference of ultrasonic pulses from multiple transducer elements that converge at a certain depth. Each array element is associated with a time delay corresponding to the focus depth. Figure 1.4 shows an eight element array with ultrasound wave-fronts propagating at different delays to converge at a given focal depth. Focusing can be categorised into three regions:

- Pre-focal (near Fresnel)
- Focal (focal Fraunhofer)
- Post-focal (far Fresnel)

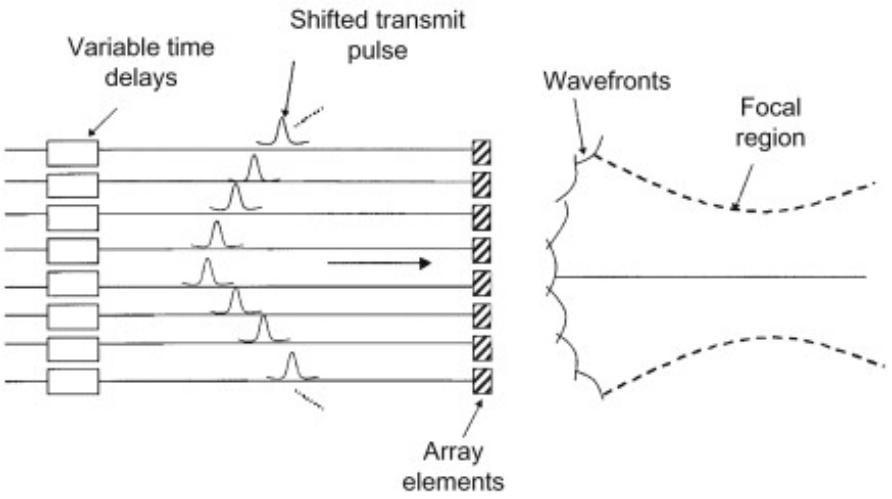


Figure 1.4: Focusing of ultrasound beam from an eight element linear array with each element giving a different time delay to transmit the pulse to a specific point [4].

Focusing is effective in the pre-focal zone and the near field depth is given by Eqn.1.8.

$$N = \frac{D^2}{4\lambda}\left[1 - \left(\frac{\lambda}{D}\right)^2\right] \tag{1.8}$$

The distance at which the beam is fully formed is called the Rayleigh distance given by Eqn.1.9, it represents the natural focus of the beam. The condition is such that $\lambda \ll D$ where D stands for the aperture diameter, L represents the depth of natural focus and $\lambda$ is the wavelength of ultrasound wave propagation [51].

$$L = \frac{D^2}{4\lambda} \tag{1.9}$$

The natural focus occurs at the Fraunhofer zone and this is ideally the location of the receiver. The beamwidth is narrowest at natural focus. The beam decays with distance once it passes this point towards the far Fresnel zone. Focusing an ultrasound beam improves spatial resolution, signal-to-noise ratio (SNR) and depth of penetration thereby improving the power transfer efficiency [50]. The spatial resolution decreases as the beam is moved away from the transmit focus [52].

### Transmit steering

Steering changes the direction of propagation of an ultrasound beam by altering the time delays of the excitation pulses from each of the transmitting elements of an array. The scanning angle determines the directional shift of the ultrasound beam. It is given by the angle between the perpendicular axis to the middle element of the array and the direction of ultrasound wave propagation. The scan angle or the steering angle can be represented as $\vartheta$. Consider Fig.1.5 with 8 elements, each element has a different time delay. If p denotes the distance of separation between two elements, n enumerates individual transducer elements in both directions from the center element represented by +/-1,+/-2 etc, then the time delay ($t_n$) is given by Eqn.1.10 [53].

$$\Delta t_n = n\frac{p}{c}\sin\theta + t_0 \tag{1.10}$$

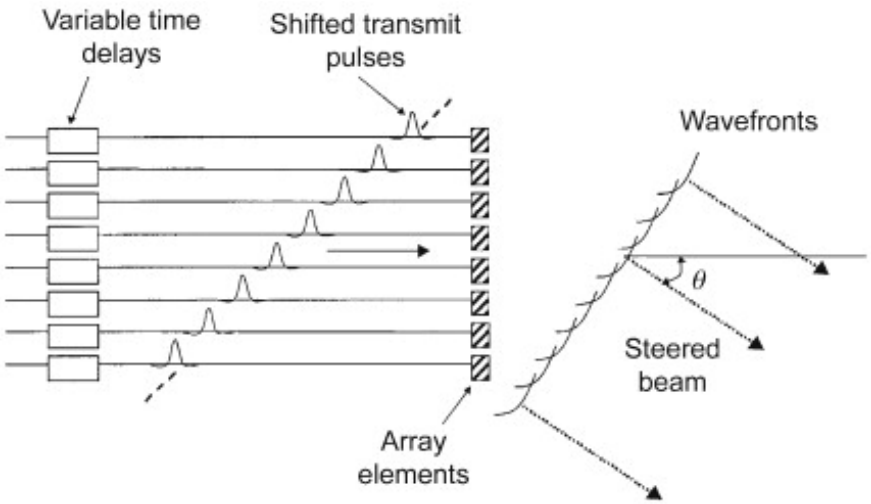


Figure 1.5: Steering of ultrasound beam from a linear array [4].

To summarize, to establish a good power link, ultrasound transmit beamforming parameters such as focusing and steering angle can be changed according to the implant location such that the implant is at the natural focus of the ultrasound beam.

## 1.3. Ultrasound for wireless power transfer in IMD

Technologies such as inductive coupling and radio waves have been commonly used due to their ease of implementation and power transfer efficiency. But, inductive coupling works well only for short distances which is a limiting factor for application in deep implants. To efficiently transfer power by means of radio waves, it is necessary to focus the energy on the implant. To focus the energy of a centimeter size device it will be necessary to go to very high frequencies (> 10 GHz). Unfortunately at these frequencies radio waves are highly absorbed by body tissues. An emerging alternative is to use acoustic power transfer. Figure 1.6 shows common methods of wireless power transfer technique used with respect to depth, implant size and received power.

Ultrasound is best known for non-invasive diagnostic imaging. Although it is extensively used in clinical applications, ultrasound has also shown to be a promising

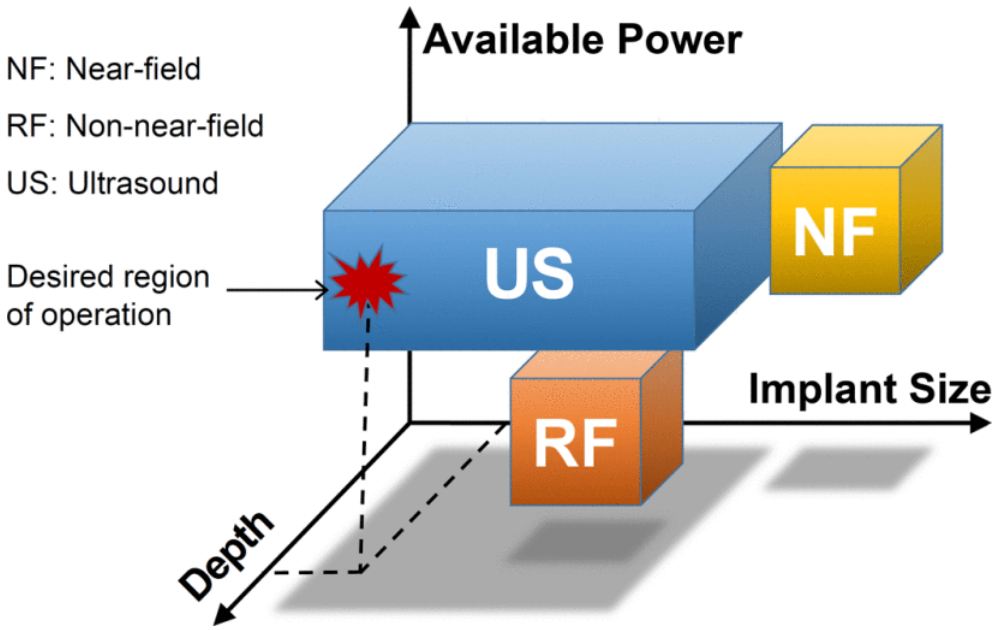


Figure 1.6: Comparison of between different wireless power transfer techniques with respect to power, depth and implant size [5].

method for wireless power transfer for implantable devices [54]. An important feature of ultrasound power delivery is that the transducer size could be miniaturized due to shorter wavelengths of ultrasound waves. For example an ultrasound wave with a frequency of 4 MHz has a wavelength of 3.75 mm (see Eqn.1.11):

$$\begin{aligned} \lambda &= c/f \\ &= 1500/(4 * 10^6) \\ &= 3.75 * 10^{-3}\ m = 3.75\ mm \end{aligned} \tag{1.11}$$

where $\lambda$ is wavelength of ultrasound wave (in m), c is the speed of ultrasound in the medium (in this case, water) (in m/s) and f is the frequency of ultrasound wave (in Hz).

Most importantly, ultrasound waves are directable implying that when focused accurately, power can be efficiently transferred. Since ultrasound has shorter wavelengths compared to RF, it is possible to focus energy to a small focal spot such as a sub-millimeter sized implant. To focus energy deep inside the body, ultrasound is a good alternative compared to radio waves that are heavily absorbed at high frequencies. Ultrasound used in the frequency range of 1 MHz to 10 MHz offers low attenuation in the order of 0.5-1 dB/cm/MHz [29]. According to the Food and Drug Administration (FDA), diagnostic ultrasound is safe on human body if the acoustic exposure levels given by the spatial peak temporal intensity ($I_{SPTA}$) is less than 720 mW/cm$^2$ [55].

The general setup for the experimental ultrasound power transfer consists of a transmitting system that includes an ultrasound probe connected to a signal generator/ pulser/ ultrasound research system, a tissue/ tissue phantom, and an implant consisting of an ultrasound energy harvester (UEH). Figure 1.7 shows a general schematic for acoustic power transfer. The receiver consists of an ultrasonic transducer, a harvesting circuit and the implant circuitry. The energy harvesting circuit converts acoustic

energy to its electrical equivalent. In its simplest form, it consists of a rectifier that converts the AC signal to a pulsating DC voltage, followed by a capacitor that stores the charge and supplies voltage to drive the implant.

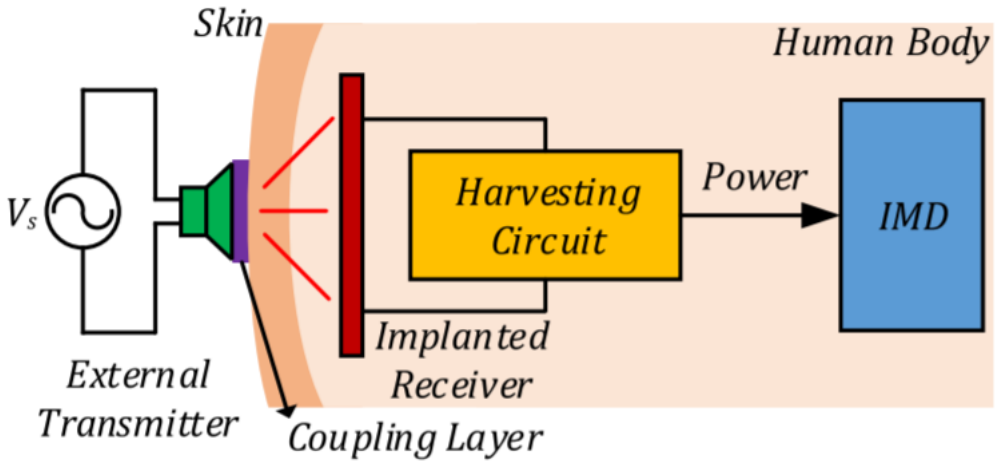


Figure 1.7: Acoustic power transfer illustrating an external transducer interfaced at the tissue boundary and the implantable medical device inside body which consists of ultrasound energy harvester and the energy harvesting circuit [6].

## 1.4. Scope

For efficient power transfer in deep implants, most of the studies published either know the implant location or transmit a high intensity unfocused ultrasound beam [24], [32]. The directional sensitivity of the ultrasound energy harvester necessitates a method to locate the implant precisely. The power transfer efficiency also depends on the size of the transmitter's focus point. Comparable sizes of focal spot and the implant will improve the power link. For instance, a 2 MHz external ultrasound transducer with 1 cm aperture diameter, focusing on a 6 cm deep implant, will have -3 dB half-power beam width less than 3 mm [17]. In this scenario, it means that the focus must be given at least 3 mm around the implant, if not, there will be degradation in energy transfer efficiency. Therefore, it is essential to focus the ultrasound beam accurately so that energy transferred falls in the half-power beam width. This implies that a slight misalignment can degrade the power transfer efficiency. A three step scheme for wireless power transfer in an ultrasonic implant is described to resolve this:

- Locate the implant;
- Establish first contact with implant;
- Switch to main circuit functioning.

The process of finding the ultrasonically powered implant, the uplink communication that is necessary to send information on the implant's energy status and using this data to fine tune the depth and angular parameters of the ultrasound beam is shown in Figure 1.8. This is an iterative process that continues until the ideal beamforming values are found. Once the implant has sufficient energy to perform main functions,

the initial uplink telemetry circuit is turned off and the main circuit starts working. This could be physiological sensing, and now a new communication protocol to send data about the implant is used.

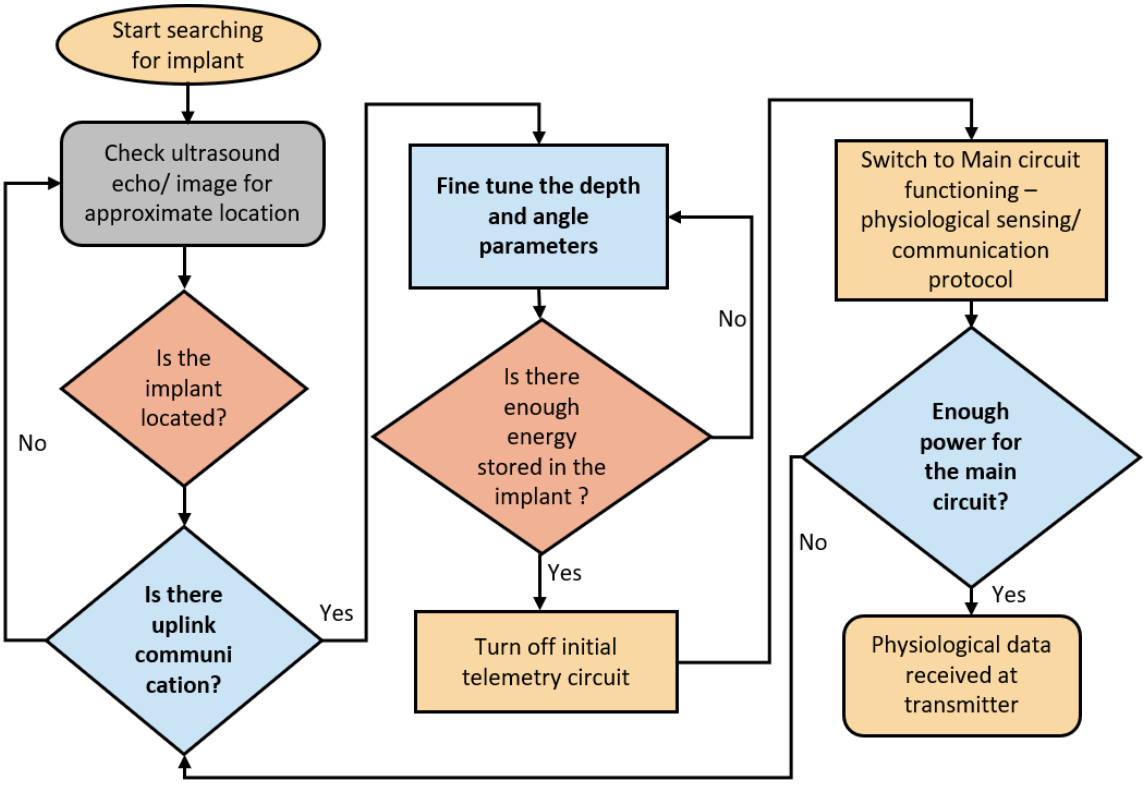


Figure 1.8: Flowchart for the three step scheme of finding the implant, establishing the first contact for fine tuning beamforming parameters followed by functioning of a main circuit.

### 1.4.1. Locating the implant

Techniques such as ultrasound imaging, time of arrival (ToA), time difference of arrival (TDoA) and received signal strength (RSS) indicator can be used to find the approximate location of the implant [56]. Ultrasound brightness (B-mode) imaging is extensively used to visualize diffused reflections from internal organs inside the human body by a method of variation in acoustic impedance. An implant inside the human body acts as a specular reflector [57]. This can cause specular artifacts, namely, ghost images and inaccurate visibility of the implant at certain angles. B-mode as a standalone method will not be able to differentiate between the implant and other objects seen in the image. Other methods such as ToA and TDoA assume line of sight (LoS) and the accuracy of RSS is low. Though these methods can approximately locate the implant, a feedback mechanism is still required such that a robust power link is maintained.

### 1.4.2. Initial uplink data telemetry

A simple low power circuit integrated into the implant can establish the first contact with the transmitter using backscattered ultrasound to fine tune the beamforming parameters. The circuit is activated as soon as it receives minimal energy from the transmitter. Then, the uplink communication takes place by modulation of backscattered

ultrasound energy. Most literature utilise a method of variation of the load impedance where amplitude modulation is used [28], [24]. The implant's load impedance is varied between short and open circuit conditions which,in turn, reflects more or less acoustic energy back to the transmitter respectively. Load impedance modulation can also be used to ensure that the signal is actually from the implant and not from other objects.

## Pulse width modulation (PWM) to send data on implant's energy

The simplest scheme to send information on the energy stored in the implant through backscattered ultrasound is to use pulse width modulation. The backscattered ultrasound signals could have artifacts due to the presence of scatterers, attenuators in the medium or even due to a person's breathing movements. But, by setting a pulse repetition time of 1 ms between two consecutive burst signals (signal N and signal N+1), it can be assumed that no significant change will happen during this time frame. Figure 1.9 shows the proposed telemetry protocol for initiating the first contact with the implant. Once two consecutive bursts are incident on the implant, the modulation circuit will alternatively change the load impedance and alter the pulse width defined by the time constant ($\tau(V_{dd})$) of signal (N+1) depending on the storage capacitor voltage ($V_{dd}$).

At the transmitter, taking the envelope difference of two adjacent reflected signals (signal N and signal N+1), the envelope pulse width is given by T - $\tau(V_{dd})$ containing the information on the implant's energy.

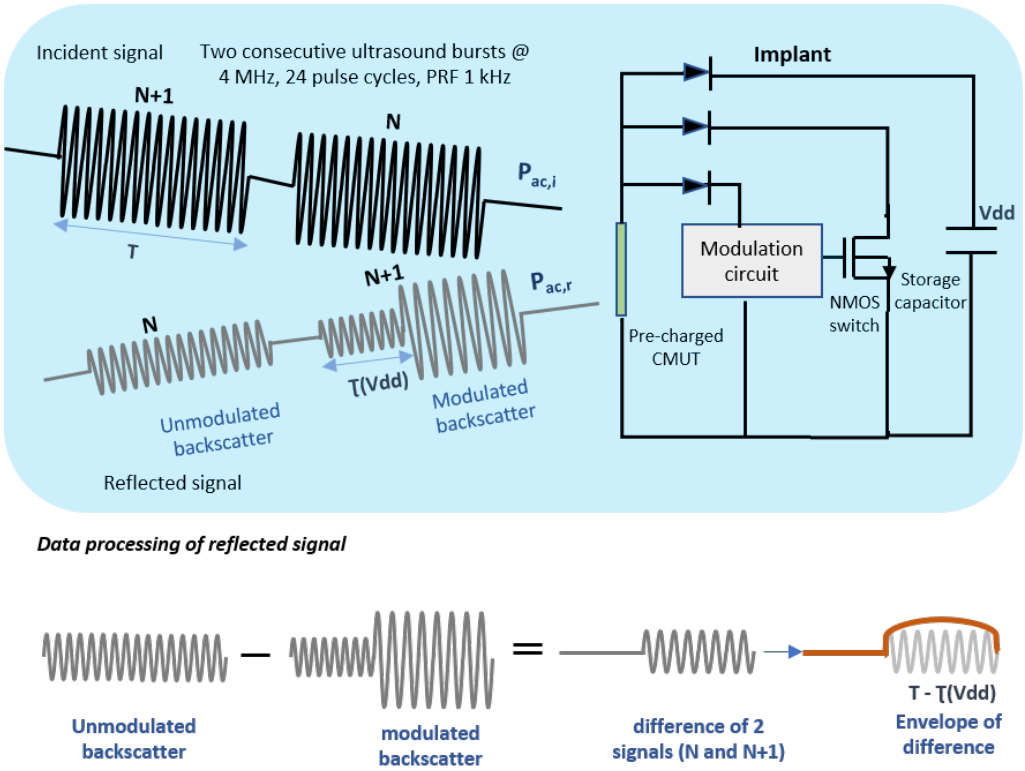


Figure 1.9: Telemetry protocol showing a) two consecutive sine bursts (N and N+1) incident on an ultrasound energy harvester (here, a pre-charged CMUT) that is connected to a modulation circuit that alternatively turns ON the MOSFET and changes the pulse width based on storage capacitor voltage ($V_{dd}$); b) data processing of backscattered ultrasound.

### Fine tuning of the beamforming parameters

Once the low power circuit starts giving energy information, the ultrasound beamforming parameters can be changed to track the implant location until an efficient power link is established. Sweeping the focus (depth) and the steer (angle) values in a plane is a first step where a heat map shows voltage information at different locations. From this, the location can be narrowed down to a hot spot where an efficient tracking algorithm determines the exact location of the implant.

## 1.5. Research goals

The research goals for this project were to develop a ”first contact” telemetry protocol and system and to test, and use the mechanism of load impedance modulation for back communication. This thesis is organized in the following chapters:

- First, an experimental setup is designed to observe the effects of load impedance on the reflection coefficient which affects the echo amplitude, this is described in Chapter 2.
- Second, a simple low power uplink data telemetry circuit is designed using discrete components. The circuit implementation and simulations are given in Chapter 3.
- Finally, a heat map on the implant’s energy at different locations are visualised and verified using The Verasonic ultrasound research system is described in Chapter 4.

Chapter 5 summarizes the thesis work. For the future work, a proposal for tracking algorithm and a new communication protocol is described.

# 2

# Effect of load impedance variation on reflected acoustic energy

An important aspect for backscatter communication is the response of the reflection coefficient of the ultrasound energy harvester on the load impedance of the uplink data telemetry circuit. In this chapter, experiments to understand the fundamentals of how the reflected ultrasound energy changes with respect to a variation in electrical impedance (a resistive load) is explained.

## 2.1. Materials

In this section, a description on the materials and equipment used in the measurements is given.

### 2.1.1. Pre-charged CMUTs

Ultrasonic energy harvesters such as piezoelectric ones have a high power transfer efficiency. The most commonly used piezoelectric transducers contain Lead Zirconate Titanate (PZT) which is non bio-compatible due to presence of lead. New types of ultrasound transducers such as a Capacitive Micromachined Ultrasound Transducer (CMUTs) have been proposed due to their bio-compatibility, ease of fabrication and the fact that they can be easily integrated with Application Specific Integrated Circuits (ASICs). In this project, a CMUT has been used as the ultrasonic energy harvester.

A CMUT is a parallel-plate capacitor with a fixed electrode at the bottom and a vibrating top electrode suspended above a cavity. The top electrode is a thin movable membrane suspended over the bottom electrode via a vacuum gap. When an AC voltage superimposed on a DC voltage is applied between the top and bottom electrodes, the membrane will deflect due to the electric field which, in turn, generates ultrasonic waves [58]. For higher sensitivity, collapse-mode CMUTs which have a bias voltage that is high enough to pull in the top membrane towards the bottom electrode are used. A single CMUT cell can act both as transmitter and receiver. The working principle of CMUT is demonstrated in Fig.2.1.

## Transmit mode

The operation of CMUTs is based on electro-mechanical forces. During transmission, a DC bias is applied to the CMUT. When it is applied to the electrodes, the top electrode and the bottom electrode are attracted to each other due to electrostatic force. An opposing force which is mechanical in nature resists this attraction [59]. This force is due to the stiffness of the the membrane. This mechanical stress is in the opposite direction of electrostatic force [60]. By applying an AC voltage, the transducer undergoes flexural vibrations [61]. This leads to generation of an ultrasound wave. Since, the electrostatic force is proportional to the square of voltage, the transducer can oscillate with double the frequency applied [62]. In the current setup, the CMUT works in the receive mode. It takes in the acoustic energy and converts it into electrical energy.

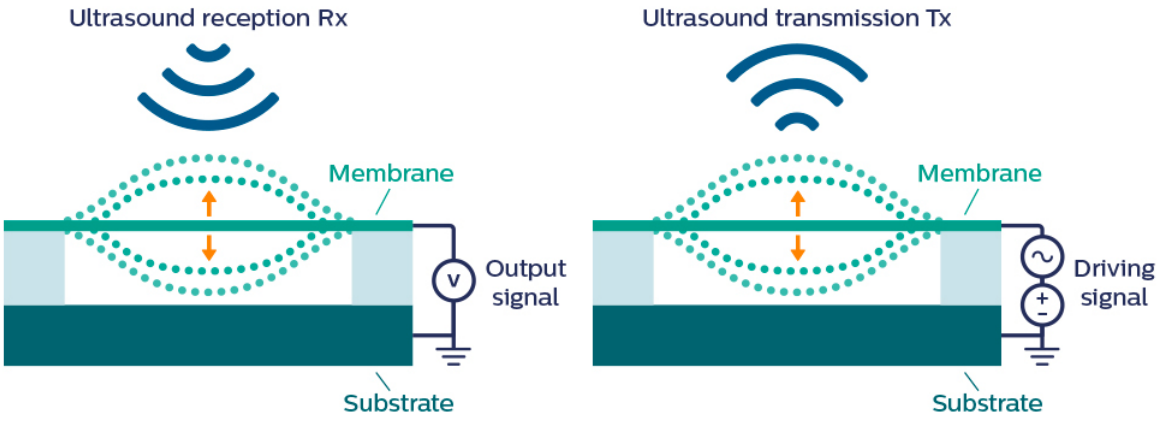


Figure 2.1: Working principle of CMUT showing a) receive mode; b) transmit mode [7].

## Receive mode

During reception, an ultrasound wave is received by the top plate. This results in membrane deflection which leads to a change in capacitance between the plates. This will result in a movement of electric charges between the substrate and the top plate. This in turn will produce an electric current under a particular DC bias voltage. A bias voltage and electric field is required to generate the displacement current [63].

For the present work, a **pre-charged CMUT** has been used, see Fig.2.2. A pre-charged CMUT incorporates a special layer in which charge is trapped thereby eliminating the need for an external DC bias. Therefore, the CMUT is always in collapse mode. The charge storage layer is a 200 nm thick $Al_2O_3$ fabricated in between the top and bottom electrode. The CMUT is mounted on a PCB and each drum has a diameter of 135 µm. CMUT employed in this study is a broadband device and hence can have multiple resonant frequencies. The CMUT is matched with an inductor that defines the working frequency. In this setup, the resonance frequency of the CMUT is 4 MHz (L=3.3 µH). Six columns of CMUT with each column consisting of 56 CMUTs arranged in parallel are connected to an SMB connector that is on PCB. The total surface area of CMUTs used is 6.3 $mm^2$. A microscopic photograph of the CMUT is given in Fig.2.3.

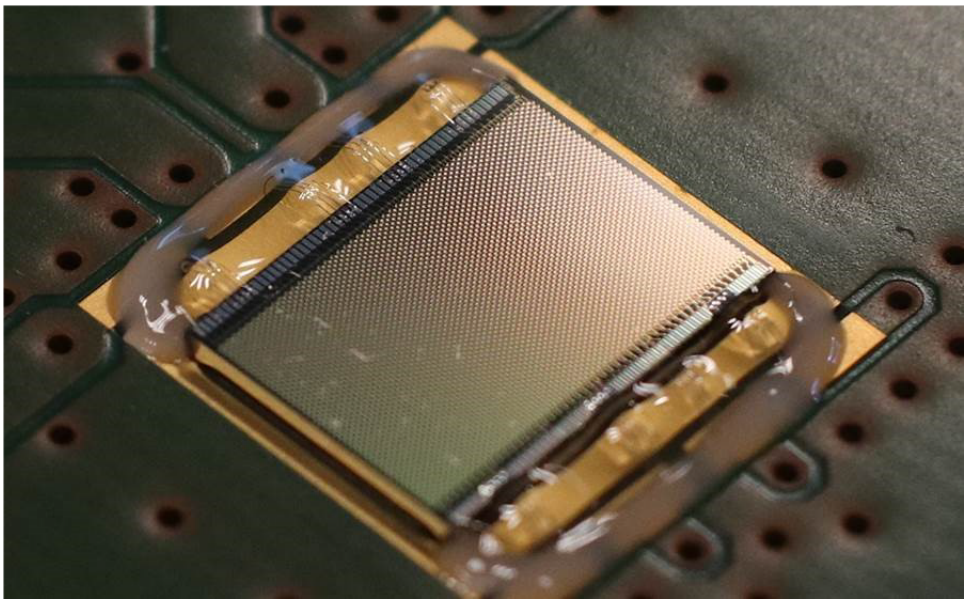

Figure 2.2: Pre-charged CMUT- 56 rows and 128 columns of CMUTs with every six columns connected in parallel constituting 336 elements wire-bonded to the PCB with a PDMS coating (protects CMUT from the tissue phantom); all CMUTs are in collapse mode used for reception of ultrasound waves (from Philips Research).

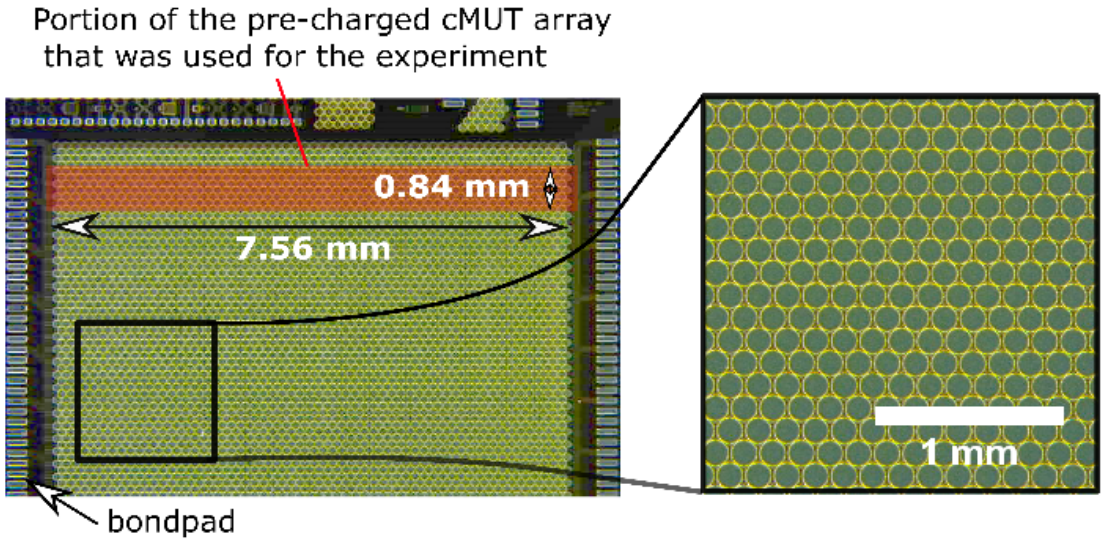


Figure 2.3: Microphotograph of CMUT with a disk diameter of 135 µm, 0.8 mm * 7.56 mm is the area of 336 CMUT drums [8].

### 2.1.2. The L7-4 linear ultrasonic transducer

A linear array piezoelectric transducer (L7-4, Philips, The Netherlands) with a bandwidth of 4-7 MHz is used in this experiment. It consists of 128 piezoelectric elements (Fig.2.5) with a spacing of 0.28 mm between elements and a total aperture size of 35.84 mm.

Figure 2.4: The L7-4 piezoelectric ultrasound transducer (Philips, The Netherlands).

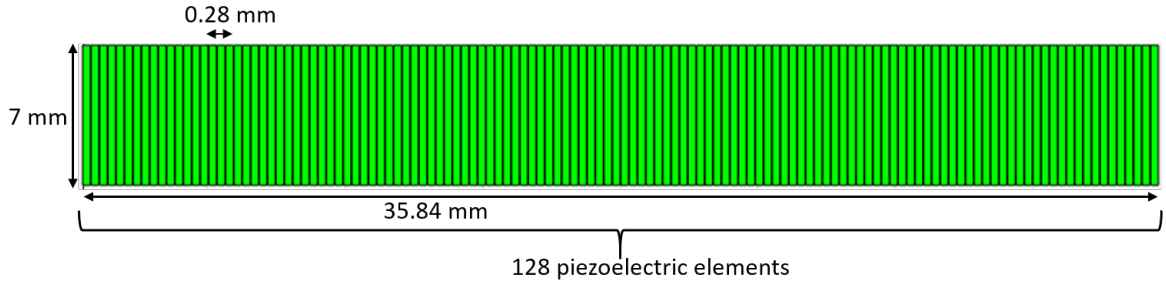


Figure 2.5: The dimensions of the probe.

### 2.1.3. The Verasonic vantage ultrasound research system

The Verasonic ultrasound research system can be used to receive, transmit and process ultrasound information [9]. Real time visualization and storage of received ultrasound data is possible. The programmable sampling frequency can go upto 62.5 MHz and the current sampling frequency used is 15.625 MHz (default setting). The vantage 128-HW configuration consists of 128 transmit channels and 128 receive channels that can be programmed independently. For this experiment, all the transmit channels have been used and the backscattered energy is observed at receive channel 64. The parameters of the ultrasound wave transmission such as focus, steering angle, time gain compensation, and delay can be controlled using a graphical user interface (GUI). The system has two connector ports available for use and one of the connectors

is connected to the L7-4 probe. The Verasonic communicates with the host PC using a peripheral component interconnect (PCI). All the commands to be performed by the Verasonic system are coded in MATLAB. The working of the Verasonic is based on a sequence of events such as acquisition, processing, image reconstruction. There are in-built structures and objects that can be used to customize the code for a specific application.

Figure 2.6: The Verasonic vantage ultrasound research system [9].

The ultrasound beamforming parameters can be varied in a custom-made GUI shown in Fig.2.7. Some of the important user defined icons including the focus depth, angle of the wave, frequency, number of pulse cycles and transducer voltage are highlighted in the GUI. TX.focus is the depth of focus of ultrasound signal. TX.steer denotes the direction of the signal. The high voltage P1 corresponds the amplitude of the pulses applied to the L7-4 ultrasound transducer. The pulse frequency can be varied in the user interface and the range depends on the bandwidth of the external transducer connected to the Verasonic. The number of pulse cycles can be set in the GUI with a maximum limit of 24 pulse cycles.

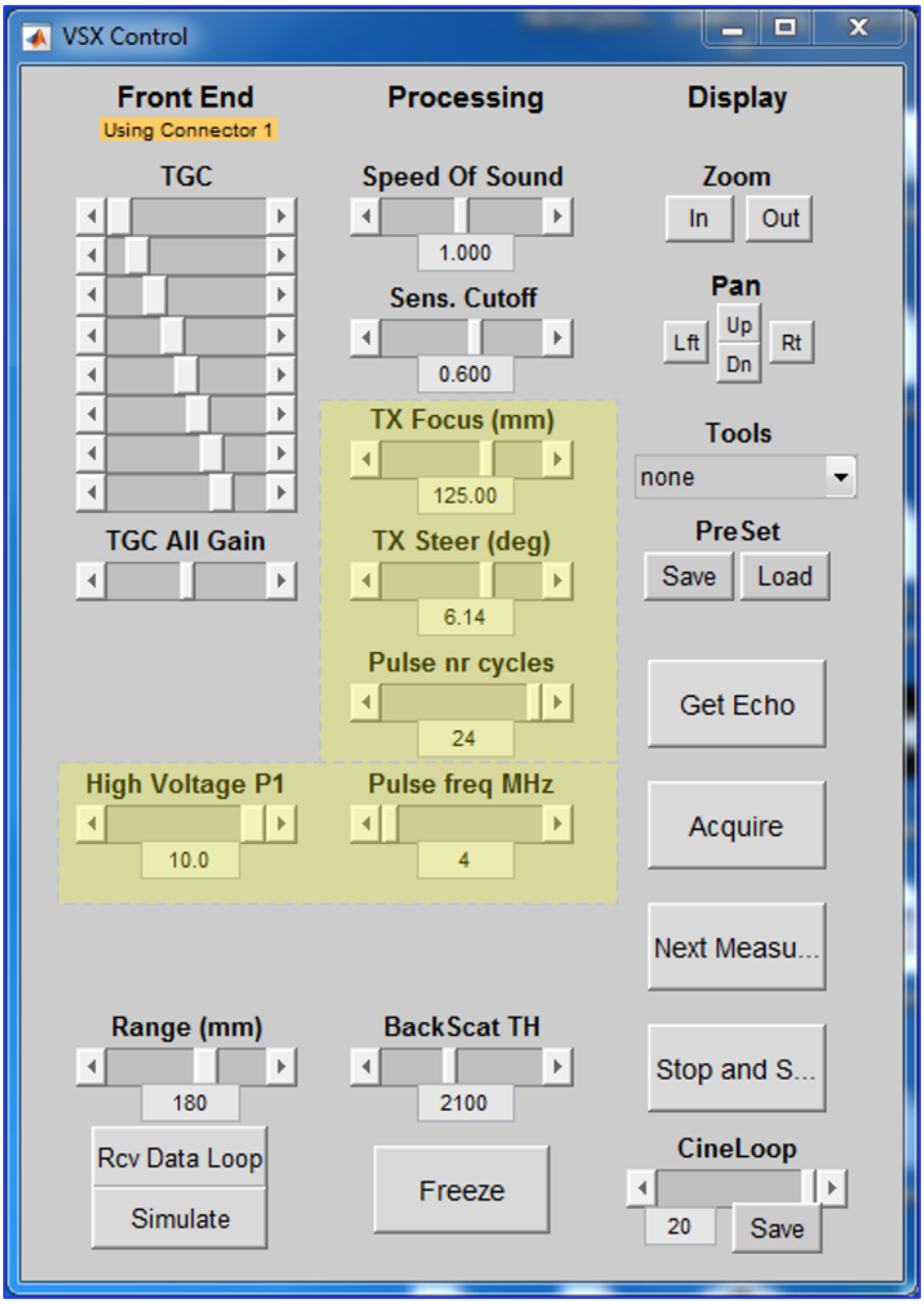


Figure 2.7: Graphical User Interface (GUI) to vary ultrasound signal parameters (Courtesy : Youri Westhoek).

## 2.2. Measurement setup

The total setup consists of the L7-4 linear probe connected to the Verasonics, a tissue phantom and a receiver consisting of the ultrasound energy harvester. The harvester consists of a pre-charged CMUT (Philips Research, The Netherlands) connected to a circuit used for adjusting the load impedance, see Fig.2.8. The linear array probe can be fully programmed using Verasonics where the commands are given in a MATLAB environment. The probe is placed on an XY translation stage universal motion controller (Model ESP300, Newport, Irvine, USA) and the receiving CMUT is placed on a rotary stage. The linear and rotary stage allows for a variation in the tissue phantom size which is useful for changing the distance between the transmitter and the receiver. The tissue phantom is made of candle gel (Rayher Hobby GmbH, Germany) which contains 95% of paraffin oil with 5% of organic constituents. Figure 2.9 shows a close up of the experimental setup with the linear array probe, tissue phantom and the CMUT mounted on the PCB. An acoustic coupling gel is usually applied to the probe to improve the acoustic coupling at the interface of two mediums.

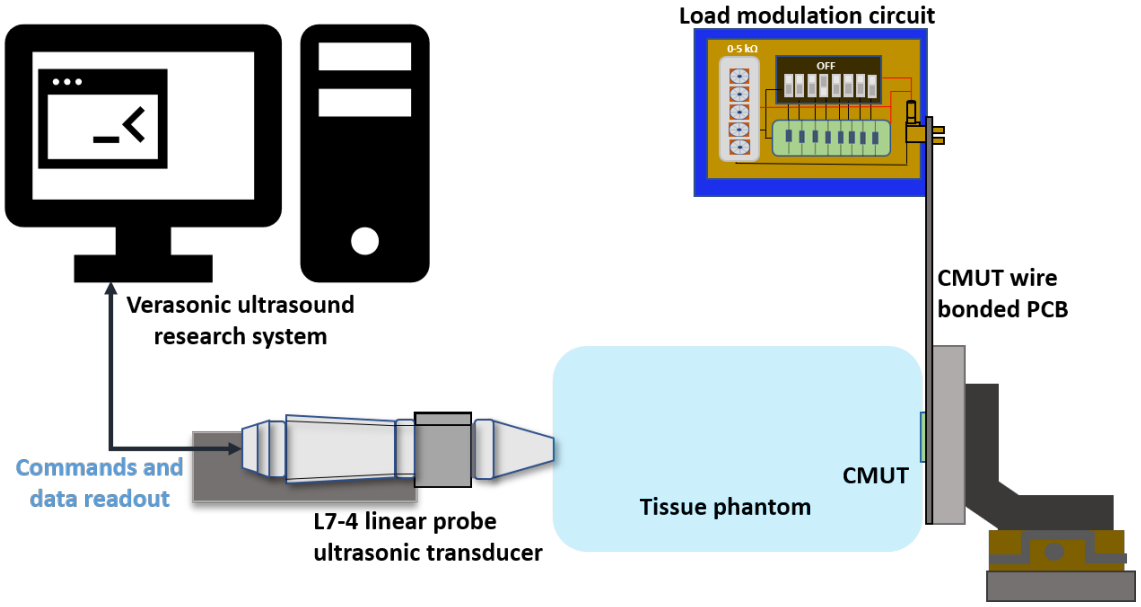


Figure 2.8: System overview for the reflection coefficient experiment.

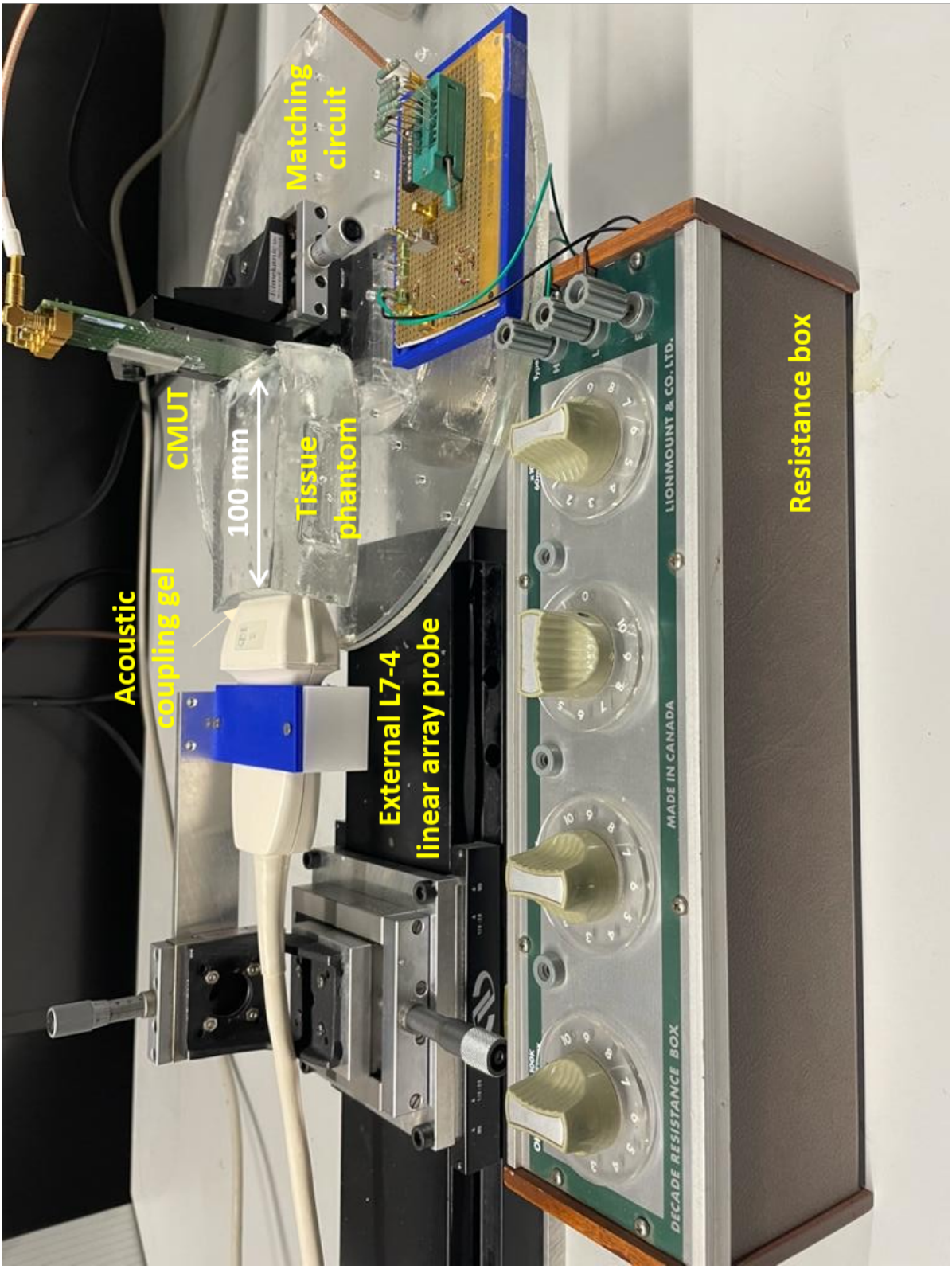


Figure 2.9: Close up view of experimental setup.

## 2.3. Theoretical background

When the ultrasound transducer in an implant receives acoustic energy, some of the energy is absorbed and some energy is reflected back (see Fig.2.10). In the ideal situation of a lossless medium, if reflected energy corresponds to X%, then the absorbed energy is (100-X)%. Reflection of ultrasound waves is quantified in terms of reflection coefficient and this can be controlled by adjusting the electrical load impedance. In this way a back communication channel can be created that does not require any transmit power.

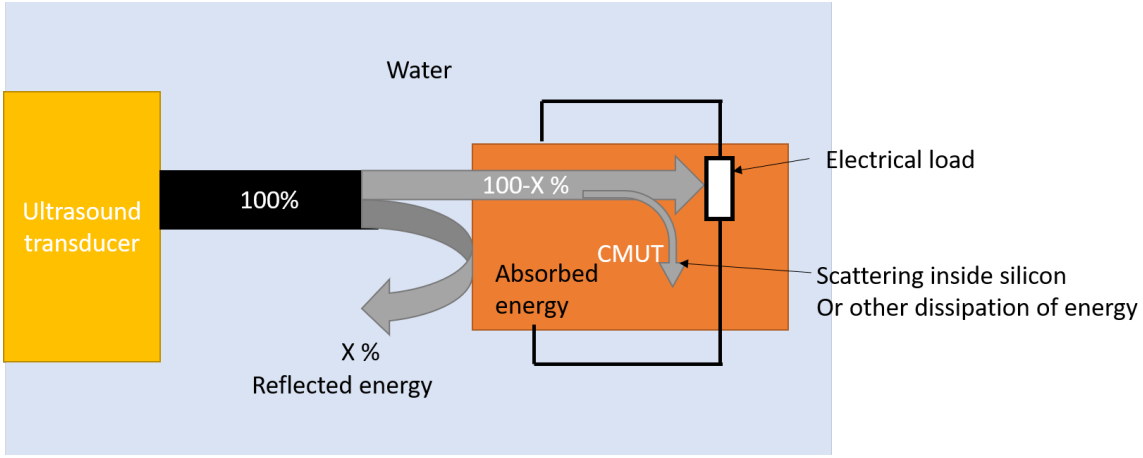


Figure 2.10: Representation of reflection and transmission of ultrasound waves in a medium (Courtesy: Shinnosuke Kawasaki).

To vary the reflection coefficient, the electrical load impedance of the ultrasound transducer is modulated by the implant circuitry as shown in the simplified circuit diagram given in Fig.2.11. This will result in an amplitude modulation of the echo. Consider an ultrasound burst signal that is transmitted to the implant. If the switch is closed, more ultrasound energy is reflected back than if it is open. The proof of concept is presented in this chapter.

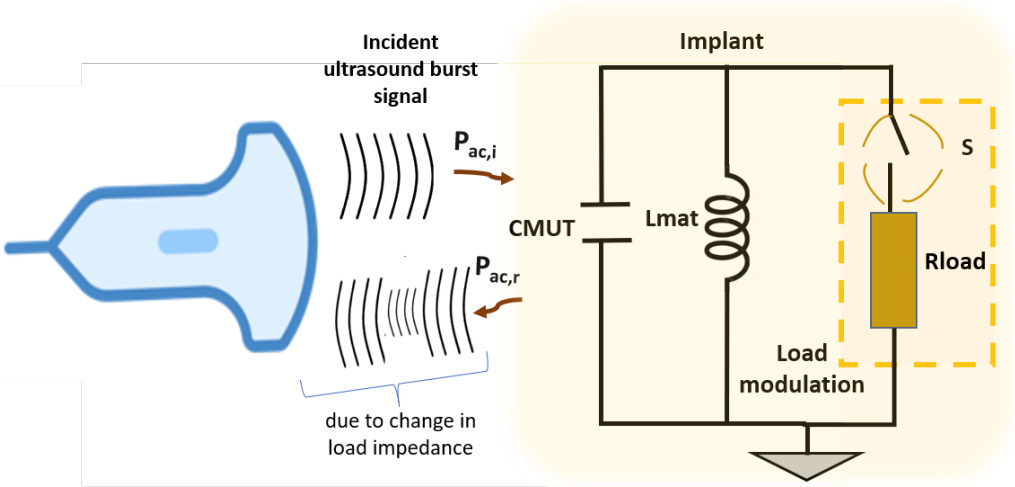


Figure 2.11: Simplified circuit diagram showing the principle of load modulation.

## 2.4. Experimental procedure

For the first experiment, the pre-charged CMUT mounted on a PCB is connected to a matching inductance and a variable resistor, see Fig.2.12. For the second experiment, a half-wave rectifier is added to the circuit to see the effect of the diode on the reflected ultrasound energy. The experiments are conducted for an input frequency of 4 MHz. A resistance box used to vary the resistance in the range of 0-2 kΩ. A rectangular tissue phantom with 100 mm length is placed between the external ultrasound transducer and the pre-charged CMUT which are properly aligned.

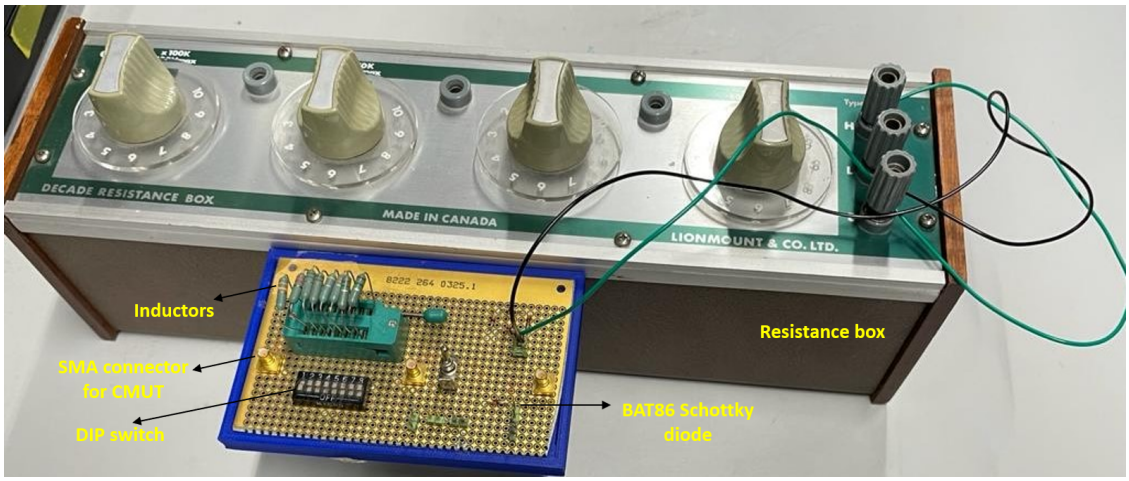


Figure 2.12: Practical circuit used for load modulation in reflection coefficient experiment.

An electrical equivalent of CMUT at series resonance connected to a load, Z is given in Fig.2.13. The source impedance ($Z_s$) is denoted by a series connection of $C_m$, $R_m$, $L_m$ and $C_e$. $C_m$, $R_m$, $L_m$ represents the electrical equivalent of a mass-spring-damper (m-k-b) system that characterises CMUT's mechanical behaviour where $C_m$ stands for the electrical equivalent of the spring (k), $R_m$ is equivalent of damper (b) and $L_m$ is the equivalent of mass (m) [8]. At the device's resonance frequency, $C_m$ and $L_m$ compensate each other. In that case the source impedance is represented by $R_m$ and $C_e$. A matching inductance, $L_{mat}$ is chosen such that Ce is compensated at resonance frequency of CMUT. $R_{load}$ represents the load impedance and when $R_m$= $R_{load}$, maximum power transfer takes place. From work done in the past, for a 4 MHz resonance frequency, the calculated capacitance is 465 pF [8]. The inductance is found using formula in Eqn.2.1.

$$\omega_r = \frac{1}{\sqrt{L_{mat}C_e}}$$

$$L_{mat} = \frac{1}{\omega_r^2 C_e}$$

$$= \frac{1}{(2\pi f)^2 C_e} \tag{2.1}$$

$$= \frac{1}{(2*3.14*4*10^6)^2 * 465*10^{-15}}$$

$$= 3.3\mu H.$$

where $\omega_r$ is the angular frequency, f is the resonance frequency.

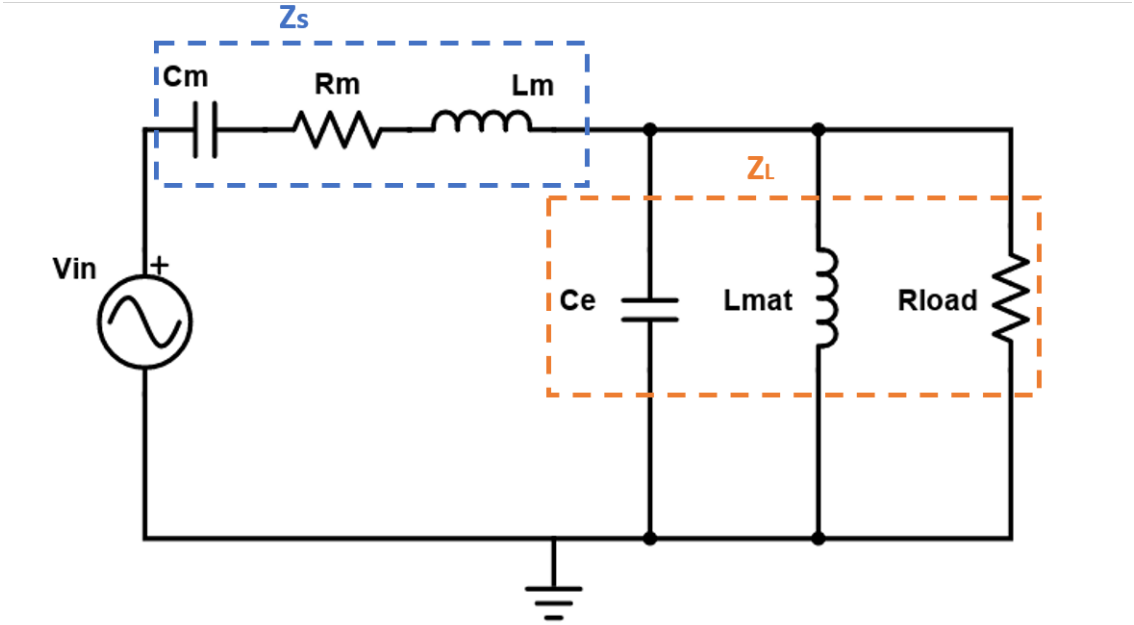


Figure 2.13: Electrical equivalent of CMUT [8].

Simplifying the CMUT as a capacitor, the circuits used for the experiments are given in Fig.2.14a and Fig.2.14b. According to Eqn.2.1, a matching inductance of 3.3 µH is selected for the 4 MHz resonance frequency. The resistance box value was changed from 100 Ω to 2000 Ω in the steps of 100 Ω. The voltage delivered by the CMUT to the load is measured with a digital storage oscilloscope (DSO).

In the experiment, a 10 V peak to peak voltage 4 MHz ultrasound sinusoidal burst signal with 24 pulse cycles with a pulse repetition frequency of 1 kHz is generated by the Verasonics and delivered to all 128 channels of the L7-4 ultrasound transducer. At the transmitter side, the reflected ultrasound energy received at channel 64 (located in the center of the linear array probe) of the ultrasound transducer is visualised and processed in Verasonic's MATLAB environment. The focusing depth of ultrasound is kept at 120 mm and the steering angle is assigned to 0°. The events occurring in Verasonic for this experiment include 'Transmit', 'Receive' and 'Process'. In the transmit event, all the 128 channels send ultrasound burst signals with a certain time delay to the focus set in the program. In the receive event, reflected ultrasound signal is acquired and stored into the host computer's local memory. In the process event, the RFData which corresponds to the reflected signals, are used for visualization and for calculating the energy. This experiment is repeated after adding a half wave rectifier to the circuit.

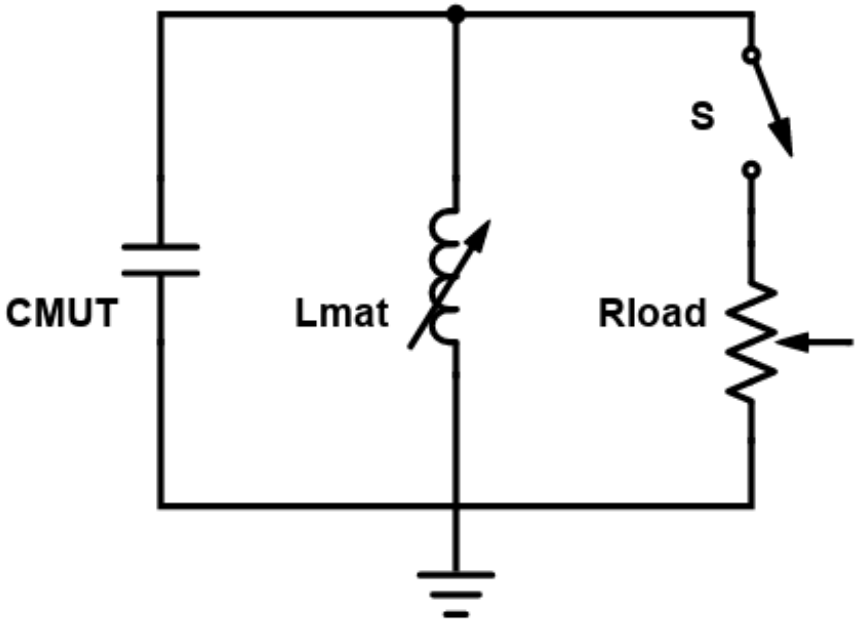


(a)

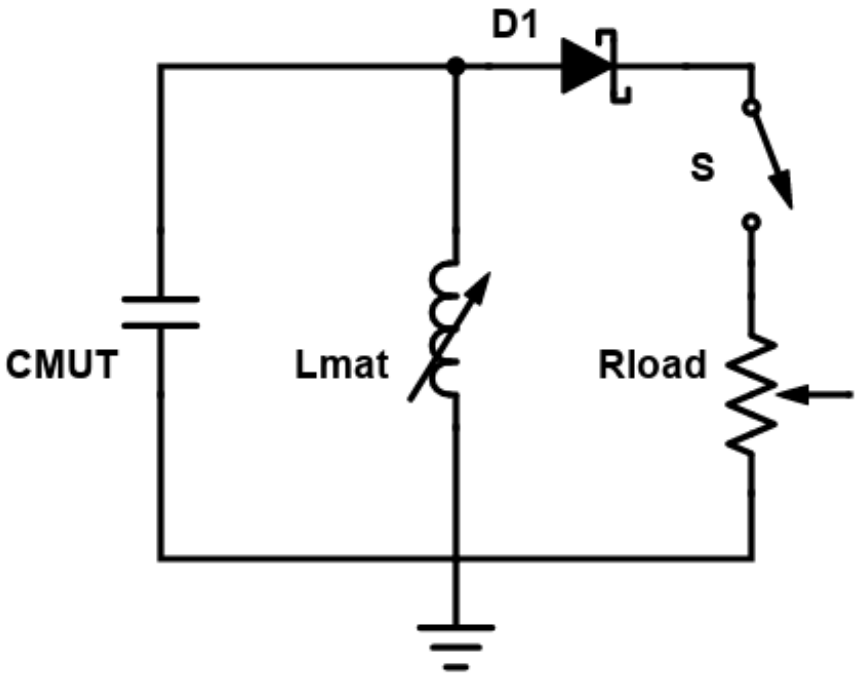


(b)

Figure 2.14: Circuit diagram a) with variable inductance and a resistive load; b) with half wave rectifier.

## 2.5. Results

The experimental results are given in terms of energy delivered to the CMUT, given by $E_{rec}$ and the amount of energy reflected back to the L7-4 probe, given by $E_{ref}$. The energy values for a single sinusoidal burst over a time duration of 1 ms is calculated. Measurements are provided in terms of energy as it remains constant and power keeps varying during the burst. It should be noted that the only source of power received by the CMUT is the acoustic energy from the L7-4 probe. The acoustic ultrasound energy delivered to the CMUT and transferred to a resistive load ($R_{load}$) with resistance values between 0 $\Omega$ to 2000 $\Omega$ is calculated from the data from the digital storage oscilloscope. The resistive load values are changed with the resistance box. By taking the instantaneous voltage ($V_{rec}$) delivered to the load by the CMUT over a time duration of the burst (T) for a specific $R_{load}$, the received energy is given by Eqn.2.2. An example of the voltage seen at the resistive load connected to CMUT is illustrated in Fig.2.15.

$$E_{rec}\ [J] = \int_{t=0}^{t=T} \frac{V_{rec}^2}{R_{load}} dt \tag{2.2}$$

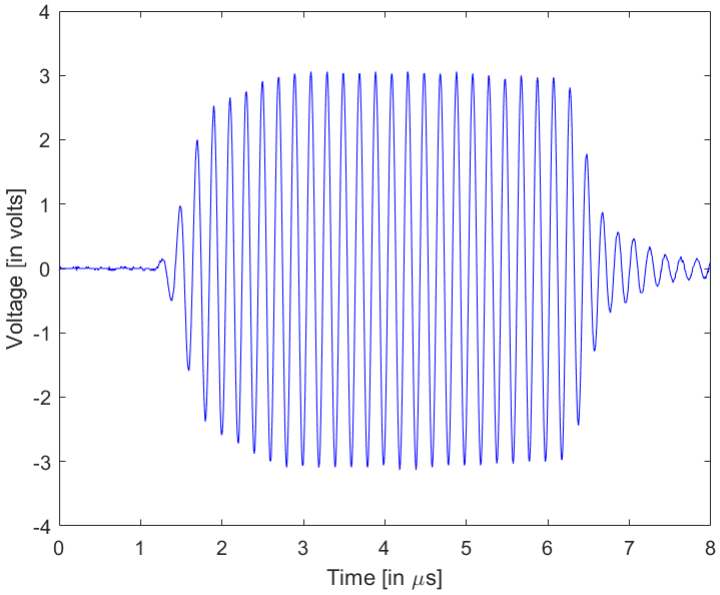


Figure 2.15: Measured voltage for a resistive load of 100 $\Omega$.

The reflected ultrasound signal is amplified with respect to time by Time Gain Controlled (TGC) amplifiers which provides a gain (G) that is constant for all the reflected signals. Although this gain is unknown, it is constant, so to make a qualitative comparison of the reflected gains possible, the reflected energy is given in arbitrary units. These signals are digitized by a 14 bit analog to digital converters (ADC) sampled at 15.625 MHz. These signals are reconstructed for visualization [11]. The total reflected energy can be calculated by measuring the echo amplitude at each sample point ($A_{ref}$) for a particular resistance for the time duration of the burst, in this case 1 ms. G denotes the gain contributed by the time gain controlled amplifier. Figure 2.16 shows an example of a reflected ultrasound signal visualized at receive channel 64 of

the L7-4 ultrasound transducer. The amplitude and gain of each sample point seen in the signal is squared and integrated over the duration of the burst.

$$E_{ref}\ [arb] = \int_{t=0}^{t=T} (G * A_{ref}(t))^2 dt \tag{2.3}$$

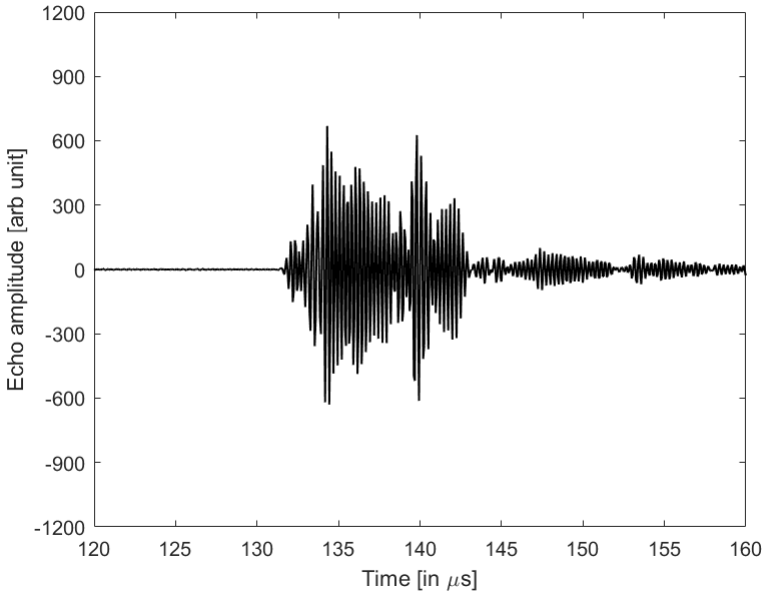


Figure 2.16: Reflected ultrasound signal visualized in Verasonic system.

## 2.5.1. Measurements at 4 MHz

Figure 2.17 shows the total energy delivered by CMUT for different loading conditions and also the total reflected energy seen by the L7-4 probe, see Fig.2.14a for the circuit schematic.

When the resistance was close to 0 Ω (short), the CMUT received 20.32 nJ of energy in a single burst. Maximum energy of 267 nJ was transferred when $R_{load}$ was 100 Ω. Also at this resistance value, the energy harvested was maximum and the reflected energy was minimum. But, once the optimum load was further increased, the received energy decreased. The received energy varied 41.58% and the reflected energy changed 33% between $R_{load}$=10 Ω and $R_{load}$=1000 Ω. Overall, the received energy varied from 20.32 nJ to 267 nJ. It is clear from the measurements that received energy by the CMUTs tends to follow a symmetrical pattern near the matched load and that the received energy is lowest when $R_{load}$ is low and after the matched load, the received energy decays.

The energy of the reflected ultrasound for each loading condition was also recorded, and it was found that the reflection was maximum when the load resistance was close to 0 Ω. The reflected energy tends to increase after the matched load condition. Between the matched and mismatched load conditions, a maximum of 40% change in reflection was observed (see Fig.2.18a and Fig.2.18b).

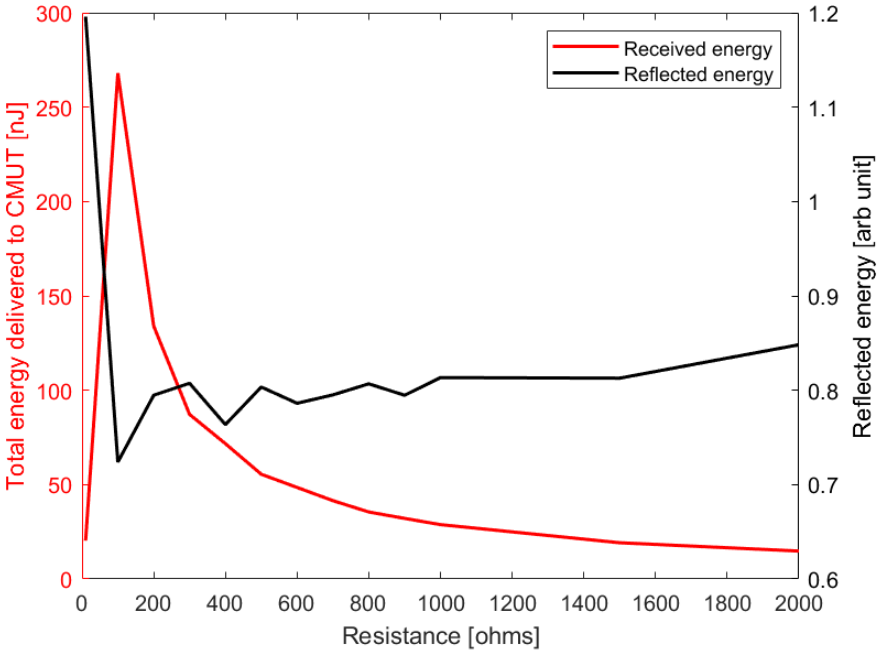


Figure 2.17: Reflected ultrasound energy measured at Verasonic is provided on the right y-axis and received energy by CMUT as a function of load resistance is provided in the left y-axis.

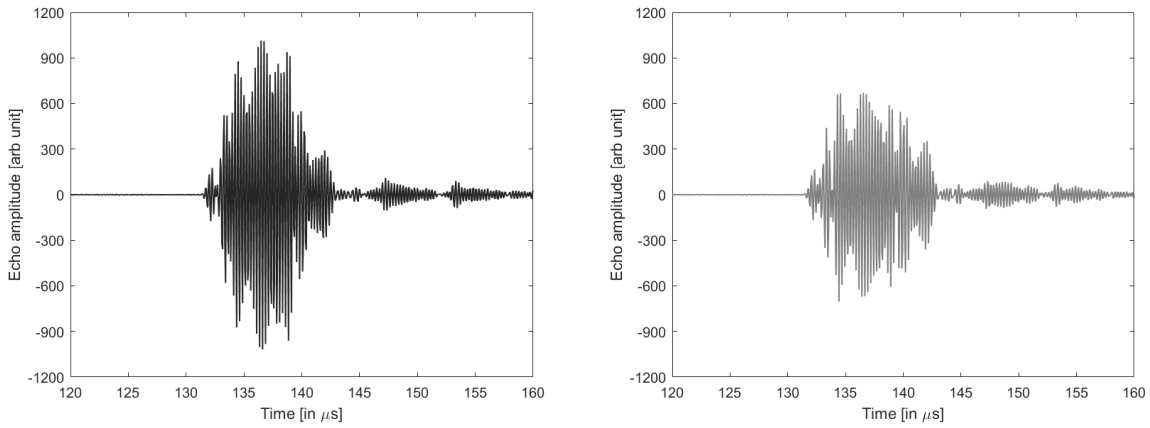


(a) (b)

Figure 2.18: Reflected ultrasound energy at a) $R_{load}$= 0 Ω; b) $R_{load}$ = 100 Ω.

### 2.5.2. Measurements at 4 MHz with a half wave rectifier

In the next measurement a small signal Schottky germanium diode (BAT86, Vishay Semiconductors) was inserted in between the CMUT and inductor combination and the load resistor, see Fig.2.14b for circuit schematic. Figure 2.19 shows an example of a signal seen at the resistive load for $R_{load}$=1000 $\Omega$.

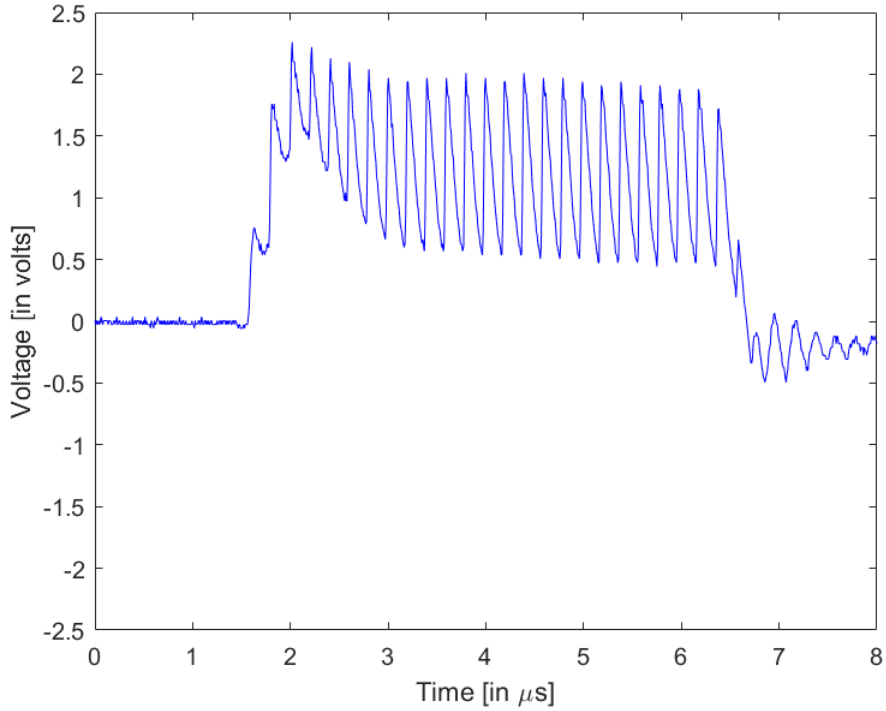


Figure 2.19: Voltage measured in the oscilloscope at a resistive load of 1000 $\Omega$.

A maximum energy of 122 nJ was delivered to the CMUT for a resistive load of 100 $\Omega$. In theory, this is expected to be half the value observed in the previous experiment due to addition of a half wave rectifier. The optimal load was found to be 100 $\Omega$ with maximum energy harvesting and minimum reflection. A maximum reflection change of 37.5% between matched and mismatched load settings. The reflected energy curve tends to stay constant after the matched load unlike the previous measurement. This could be due to the fact that diode only allows current to flow in one direction. During the positive half-cycle, the load resistance gets optimally matched with $R_m$ as the diode allows the signal to pass through. Therefore, the reflected energy characteristic becomes similar to that of circuit with only resistive load. But during the negative half-cycle, this matching does not happen as the diode doesn't conduct current and therefore all the energy is being reflected back. So, the reflected energy plot for the negative half cycle, would have shown high reflections. So, the right y-axis of Fig.2.20 is a combination of two curves from the positive and negative half-cycles of the burst signal.

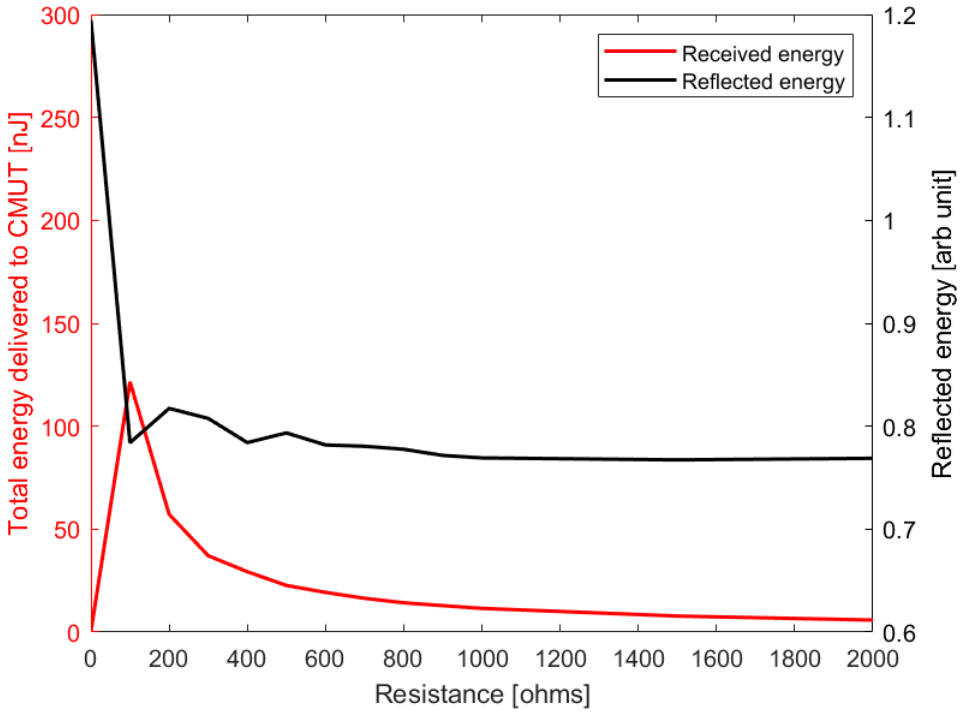


Figure 2.20: Reflected ultrasound energy measured at Verasonic is provided on the right y-axis and received energy by CMUT as a function of load resistance is provided in the left y-axis for the circuit with diode.

## 2.6. Discussion and conclusions

A large variation in the reflected acoustic energy was observed in both the experiments. A significant and detectable change of upto 40% reflection was seen by adjusting the load from short to a resistance value of 100 $\Omega$. It was found that a matched electrical load harvests maximum energy and also minimizes the ultrasound energy reflected back. In both the measurements, this occurred at a resistance value of 100 $\Omega$. As a result, the amount of reflection is smallest at optimum load, $R_{load}$=$R_m$. The measurements with resistive load harvested a maximum of 267 nJ and the half wave rectifier harvested 122 nJ. The measured energy value at the half-wave rectifier circuit was slightly lower than the expected value (=267 nJ/2).

There are several limitations that affected the experiment. The alignment of the probe to the CMUT played an important role in how the reflections were measured. In the experiments, it was assumed that all the reflected signals received by the probe originated from the CMUT, but there could have been scatterers, e.g. bubbles in the tissue phantom which impacted the observed value.

Despite these limitations, there are few takeaways that becomes a stepping stone for the backscatter communication. Varying the load impedance between short and a high resistance value significantly impacts the reflected acoustic energy. These two states can be decoded as '1' and '0' thereby showcasing data transfer. Therefore, electrical load impedance modulation can be used for passive communication using ultrasound.

# 3

# Data telemetry uplink

In this chapter, a very simple low power circuit that establishes the first contact with the implant is discussed. For this, an uplink data telemetry circuit is designed to send information from implant back to the transmitter using backscattered ultrasound. It sends storage capacitor voltage information to external ultrasound probe using pulse width modulation. Commercially available low power discrete components have been chosen to build this circuit.

## 3.1. Experimental setup

The materials and the total setup used in this experiment are same as discussed in Chapter 2. Instead of the resistive load, a telemetry circuit is connected to the CMUT. The complete setup consists of the L7-4 linear probe connected to the Verasonics, a tissue phantom and a receiver consisting of the ultrasound energy harvester with the uplink data telemetry circuit (Fig.3.1). The probe and the CMUT are perfectly aligned to observe the proper working of the circuit. Figure 3.2 shows a closeup photo of the experimental setup to test the uplink communication and Fig.3.3 shows the circuit.

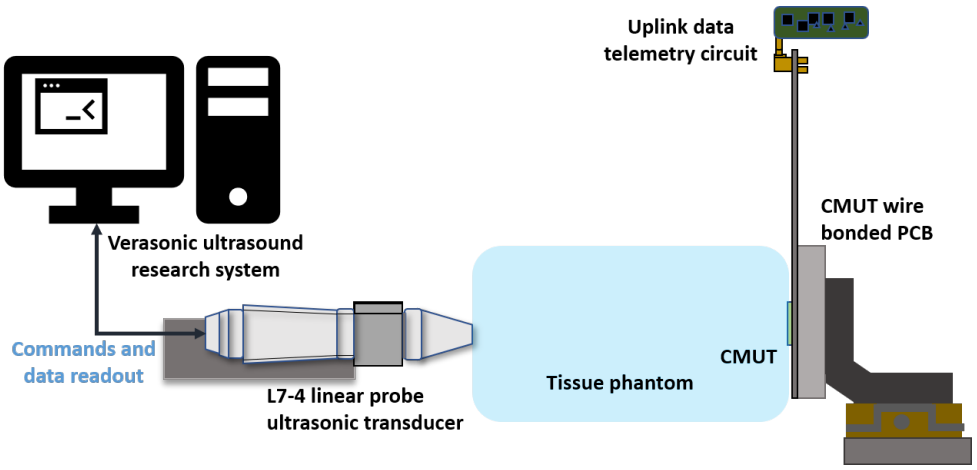


Figure 3.1: Experimental schematic showing the linear array probe connected to the Verasonic, and the CMUT array mounted on a PCB that is connected to the uplink data telemetry circuit.

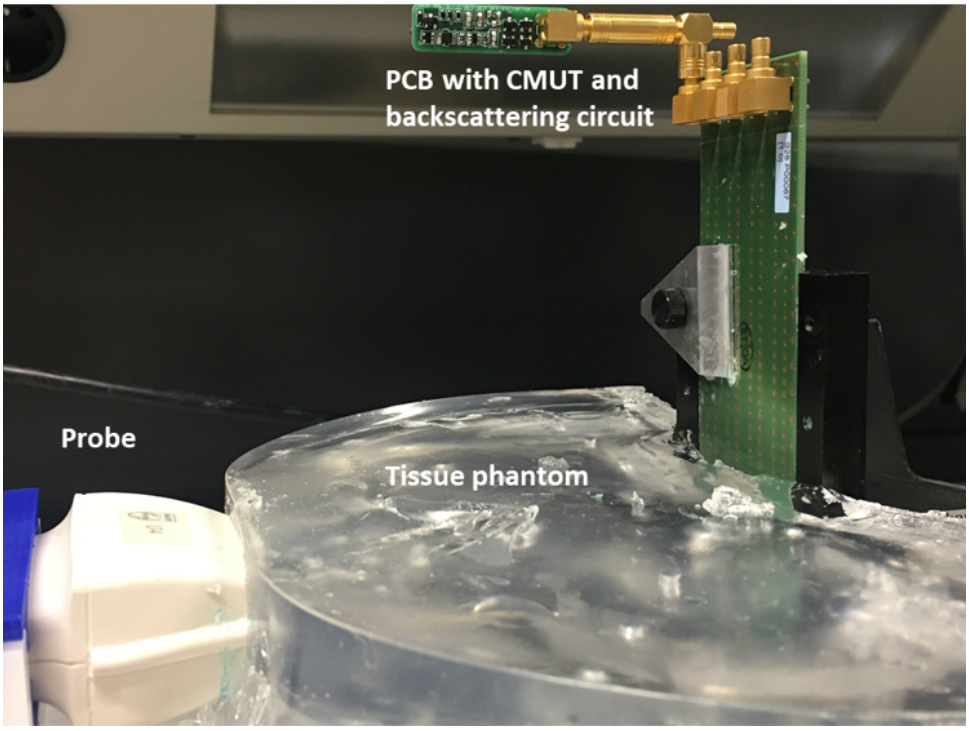


Figure 3.2: Experimental setup showing a) the linear array probe fixed on an XY linear stage; b) the tissue phantom made of candle gel; c) the ultrasound energy harvester consisting of a CMUT array mounted on a PCB connected to the uplink data telemetry circuit.

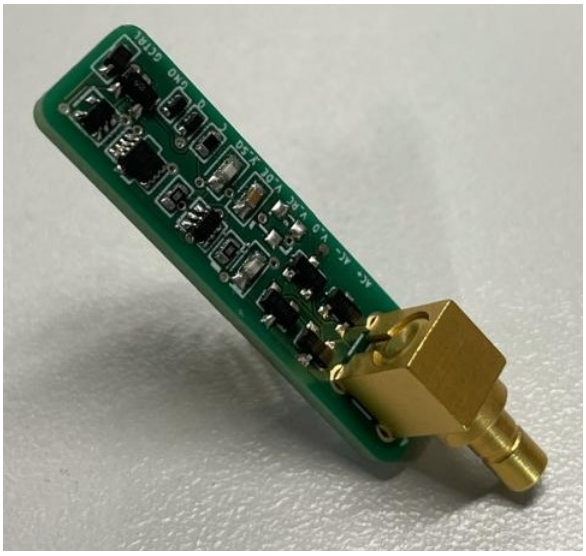

Figure 3.3: The uplink data telemetry circuit.

## 3.2. Circuit implementation

The circuit has mainly two functions - to modulate every consecutive incoming burst, and to change the pulse width (time constant) as a function of supply voltage of the implant. This circuit can be used to establish an initial communication between the implant and the ultrasound transmitter outside the body. For acoustic power transfer in implants, the initial telemetry will aid in focusing the ultrasound waves towards the CMUT to maintain a robust power link.

To reduce the power consumption, the circuit was designed using advanced ultra low power (AUP) logic components obtained from NXP Semiconductors. The power consumption of circuit is as low as 0.5 µW. A 4 MHz sine burst with 24 pulse cycles with a pulse repetition frequency of 1 kHz is the input signal. So, each sinusoidal burst lasts for 6 µs. Figure 3.4 shows the circuit diagram. Figure 3.5 shows the waveforms at the nodes labelled in the circuit diagram. The electrical equivalent of CMUT is modelled as a voltage source ($V_{in}$) with source impedances $C_m$, $L_m$, $R_m$ and $C_e$ where at the device's resonance frequency, $C_m$ and $L_m$ are compensated. For the 4 MHz input frequency used in this experiment, $L_{mat}$ is chosen as 3.3 µH to compensate for $C_e$= 465 pF [8]. The CMUT with the matching inductance is connected to a full-wave rectifier which is divided into a common anode (BAT754A) and three common cathode branches (BAT754C).

The energy harvesting circuit converts acoustic energy into electrical energy. A full wave rectifier consisting of D1 to D4 converts the incoming burst signal into a pulsating DC voltage. The storage capacitor accumulates the charge and supplies voltage ($V_{cc}$) to drive the complete circuit. The circuit is solely powered by the burst signal from the L7-4 probe. A 3.6 V rated Zener diode ($D_z$) is connected in parallel to the storage capacitor to protect the circuit from a too high supply voltage. All the diodes used for rectification are Schottky diodes that have a very low turn on voltage ( 0.4 V).

The second branch with common cathode is connected to a MOSFET. The MOSFET is turned ON/OFF depending on the logic circuitry controlling its gate voltage. In the third branch, the sine burst is rectified and an envelope of the signal is retained. The resistive and capacitive values (Eqn.3.1) were chosen such that the time constant ($\tau_{env}$) of envelope detector was larger than the burst signal duration. This signal is converted into a sharply defined square wave using a Schmitt trigger (74AUP2G17GW).

$$\begin{aligned} \tau_{env} &= R * C \\ &= 100 * 10^{3} * 82 * 10^{-12} \\ &= 8.2\ \mu s \end{aligned} \tag{3.1}$$

To design a circuit for modulating the pulse width depending on the voltage of the storage capacitor, a suitable component needed to be found. Variable capacitors diodes exist that alters their capacitance based on its reverse bias voltage. Hence, a low voltage variable capacitance diode BB202 (NXP Semiconductors) was chosen for modulating the pulse width based on the voltage of the storage capacitor. It has a very steep capacitance-voltage curve, see Fig.3.6 [10]. As the reverse bias voltage is increased capacitance decreases down to 10 pF and then remains constant. Small

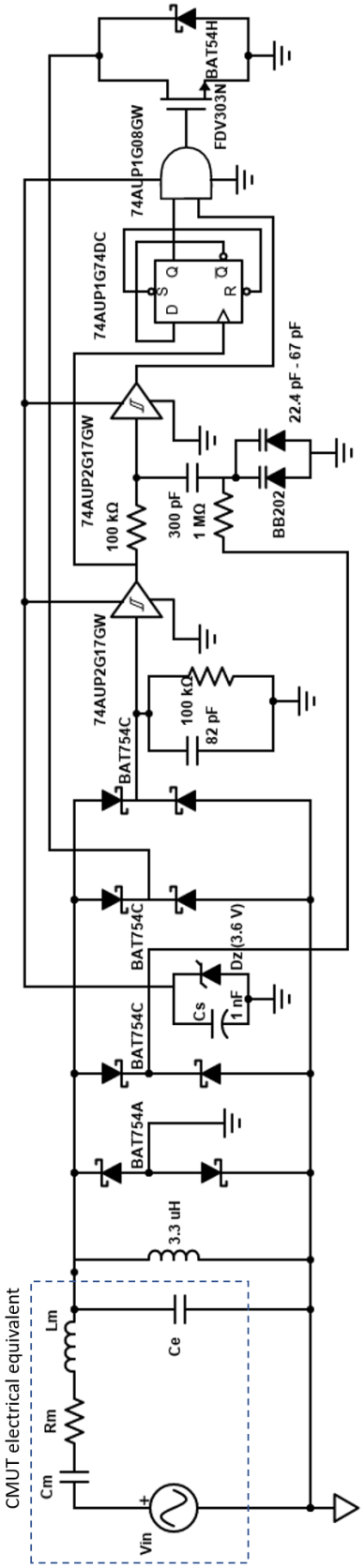


Figure 3.4: Circuit diagram for uplink data telemetry circuit.

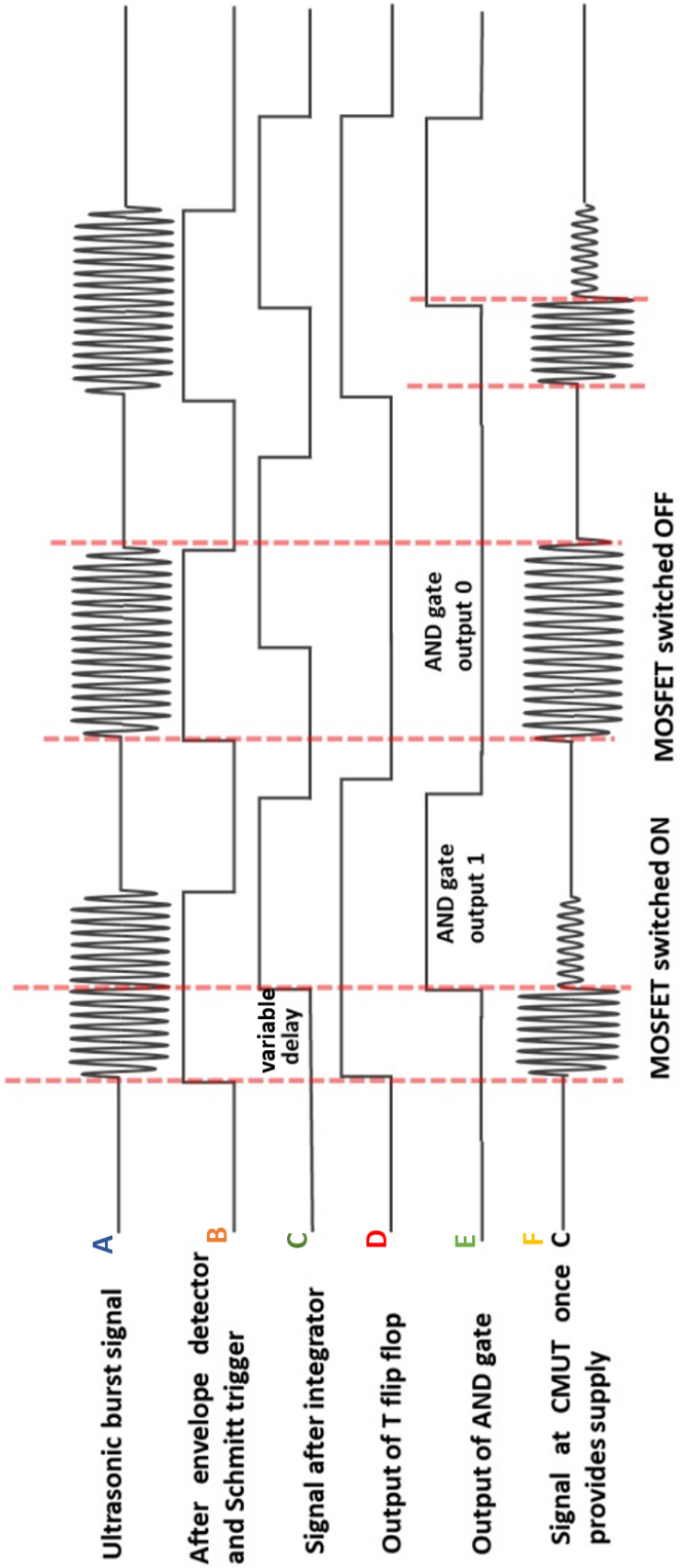


Figure 3.5: Timing diagram.

variations in voltage up to 3 V can be deciphered accurately based on the capacitance value from the curve characteristic. A single varactor diode has a capacitance range of 11.2 pF to 33.5 pF. In this circuit, two varactor diodes are connected in parallel to get a range between 22.4 pF to 67 pF which results in a delay of up to 6.64 µs in combination with a 100 kΩ resistor. The pulse is delayed using an RC filter, which

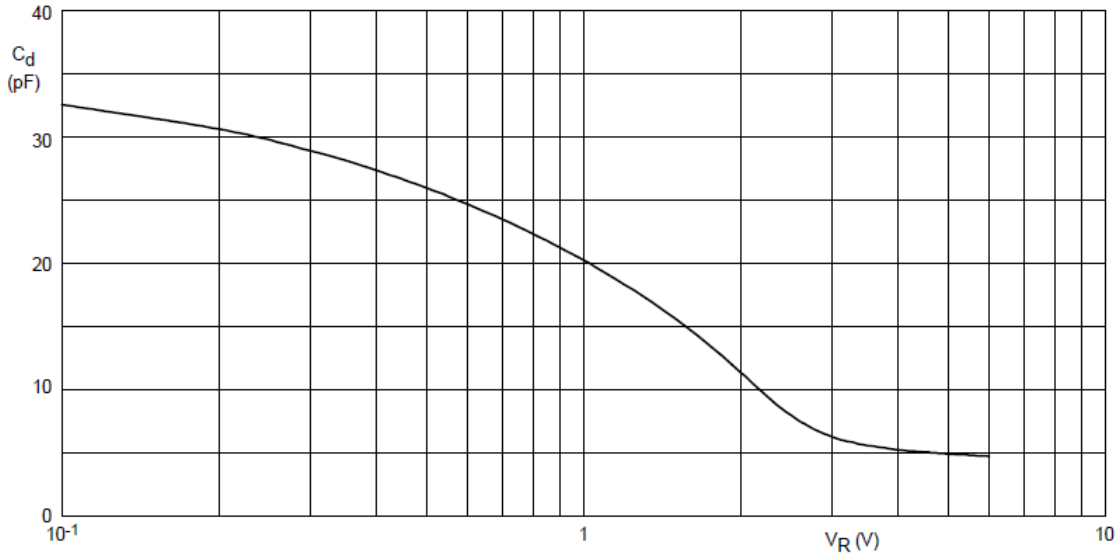


Figure 3.6: Capacitance of diode ($C_d$) as a function of reverse voltage ($V_R$) for BB202 [10].

is controlled by a 100 kΩ resistor and a series capacitance due to 300 pF capacitor and capacitance (22 pF to 66.4 pF) from a varactor diode ($C_{diode}$). The series capacitance value will be dominated by the lower capacitance value, in this case the varactor diode. The diode capacitance is modulated by $V_{cc}$ via a 1 MΩ resistor connected to its cathode terminal that will change the delay as a function of $V_{cc}$. The delay can be calculated from $\tau_{var}$ = 100 Ω * $C_d$. This signal is input to a second Schmitt trigger (ST2) making it a sharply defined square wave. The output of ST2 is one of the inputs of an AND gate (74AUP1G08GW).

Next, the complementary (Q') and individual data (D) pins of a positive edge triggered D-type flip-flop (74AUP1G74DC) are connected making it a T-type flip-flop which toggles for every positive edge of the clock pulse (CP). The clock is given by the output of ST1. The flip flop's output, Q is connected to the second input of the AND gate. The AND gate output is connected to the gate of a MOSFET (FDV303N, On Semiconductors). This low threshold voltage transistor short circuits the CMUT when the output of the AND gate is high.

To summarise, at every odd instance of the incoming ultrasound burst the MOSFET is turned ON thereby modulating the backscattered signal with a variable time delay $\tau(V_{cc})$, whereas at every even instance the MOSFET is turned OFF.

## 3.3. Results

In this section, the simulations for verifying the working of the circuit, and the data processing done in the Verasonic are discussed.

### 3.3.1. LT-spice simulation

The circuit was simulated using LT Spice (Linear Technology, USA). For the spice analysis, the CMUT was modelled as an AC source with a resistance of 400 Ω. The components chosen for the simulation were default components available in LT Spice. The variable capacitance diode was modelled using information retrieved from its datasheet. A transient analysis was performed on the circuit given in Fig.3.7. Figure 3.8 shows the waveforms at different nodes of the circuit. The input signal given was a sine burst with 24 pulse cycles with PRF = 1 kHz. $V_{ac+}$ $V_{ac-}$ denotes the AC signal source and AC ground respectively.

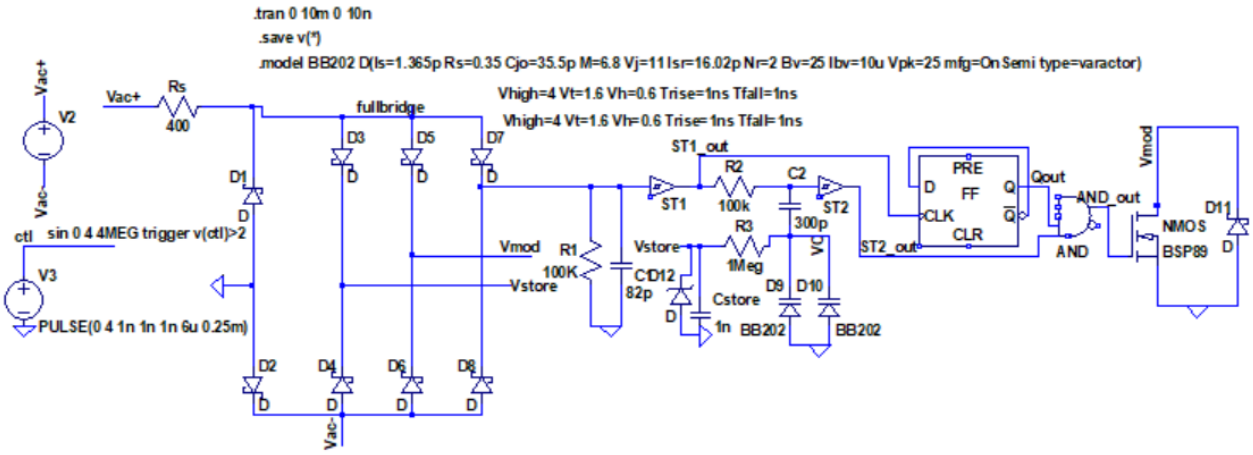


Figure 3.7: Schematic used for the LTspice simulation using pulse width.

Assuming t=0, the 300 pF capacitor starts charging slowly towards the maximum voltage. Once t= $T_{rise}$, the capacitor further accumulates charge and acts like a small battery since its value is large compared to the capacitance of the varactor diode. In this way, the voltage stored at the 300 pF capacitor is doubled and remains that way until a specific time constant. This time constant is determined by the 300 pF capacitor and the 1 MΩ resistor. This 1 MΩ resistor between the storage capacitor and the diode has a value 10 times larger than the resistor used for the integrator, which is 100 kΩ. The 300 pF capacitor is also much larger than the capacitance of the varactor diode. These capacitive and resistive values have been selected such that the time constant (Eqn.3.2) is large enough to keep the reverse bias voltage over the varactor diode constant during the burst period. By doing this, the voltage at the integrator and the varactor diode becomes a function of the supply voltage. Figure 3.9 shows the simulated reverse voltage seen at the cathode terminal of varactor diode ($V_{vc}$), voltage at the storage capacitor ($V_{vstore}$).

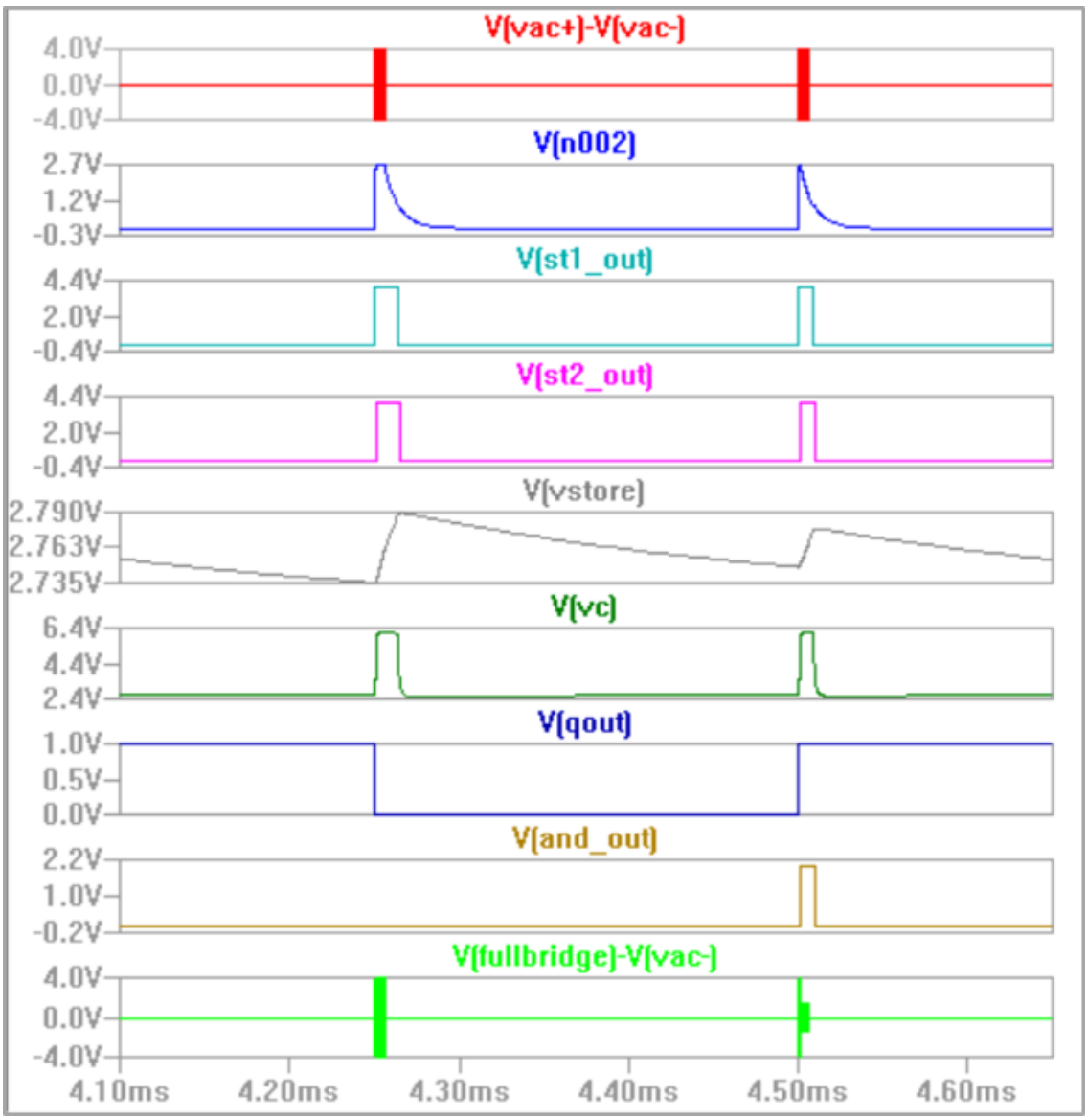


Figure 3.8: Simulation results showing: a) the input burst signal; b) signal after the envelope detector; c) sharply defined square wave after ST1; d) signal after ST2; e) voltage of the storage capacitor with a value of 1 nF; f) reverse voltage seen by the variable capacitance diode; g) output of the T-type flip-flop; h) AND gate output; i) modulated waveform seen after the voltage source and resistance representing CMUT.

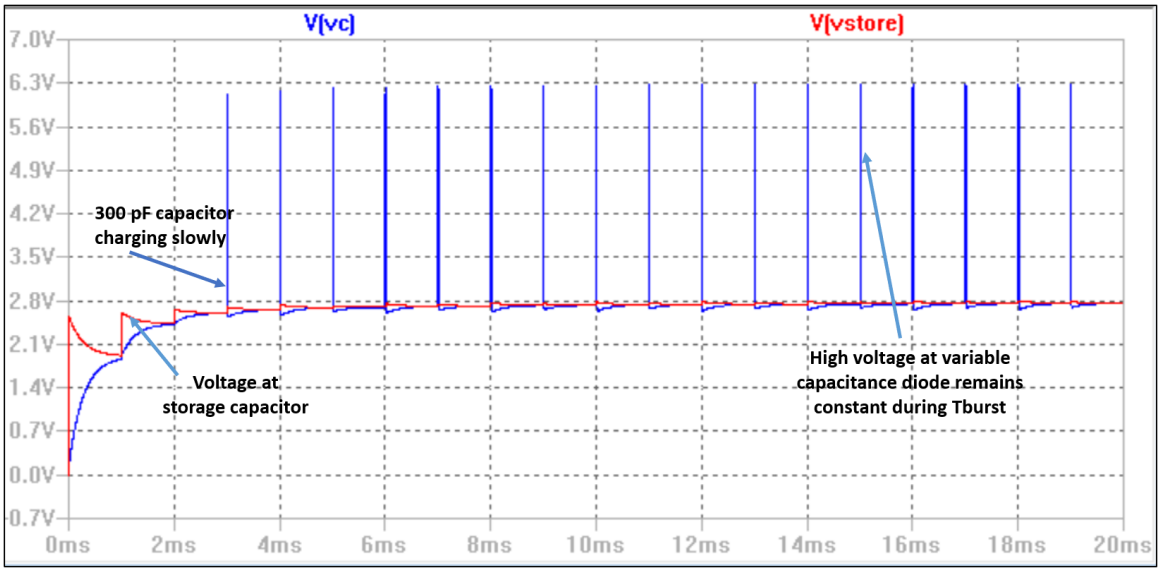


Figure 3.9: Simulated $V_{vc}$ is about twice the $V_{vstore}$ due to 300 pF capacitor during the burst period.

$$\begin{aligned} \tau &= R * C \\ &= 1 * 10^{6} * 300 * 10^{-12} \\ &= 0.3\ ms \end{aligned} \tag{3.2}$$

Figure 3.10 and Fig.3.11 shows the dependency of the pulse delay on the storage capacitor voltage ($V_{vstore}$). To vary $V_{vstore}$ in the simulation, a transient analysis was performed for two input voltages ($V_{p\text{-}p}$) of 4 V and 5 V. Comparing the two modulated waveforms, the delay due to different voltages can be observed.

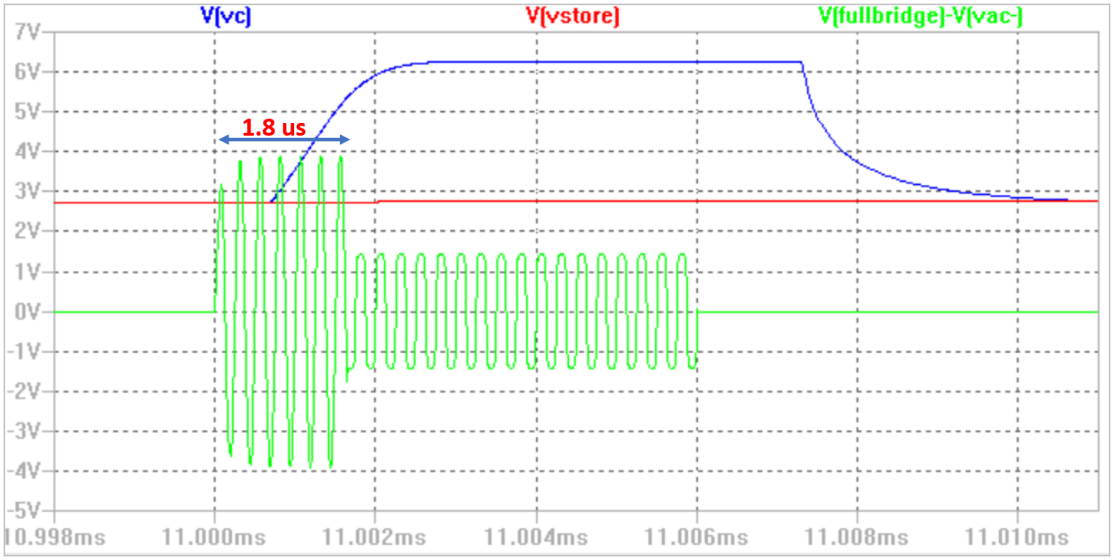


Figure 3.10: Modulated waveform ($V_{fullbridge}$-$V_{ac-}$), storage capacitor voltage ($V_{vstore}$), reverse bias voltage at varactor diode with a delay of 1.8 µs for $V_{vstore}$= 2.7 V.

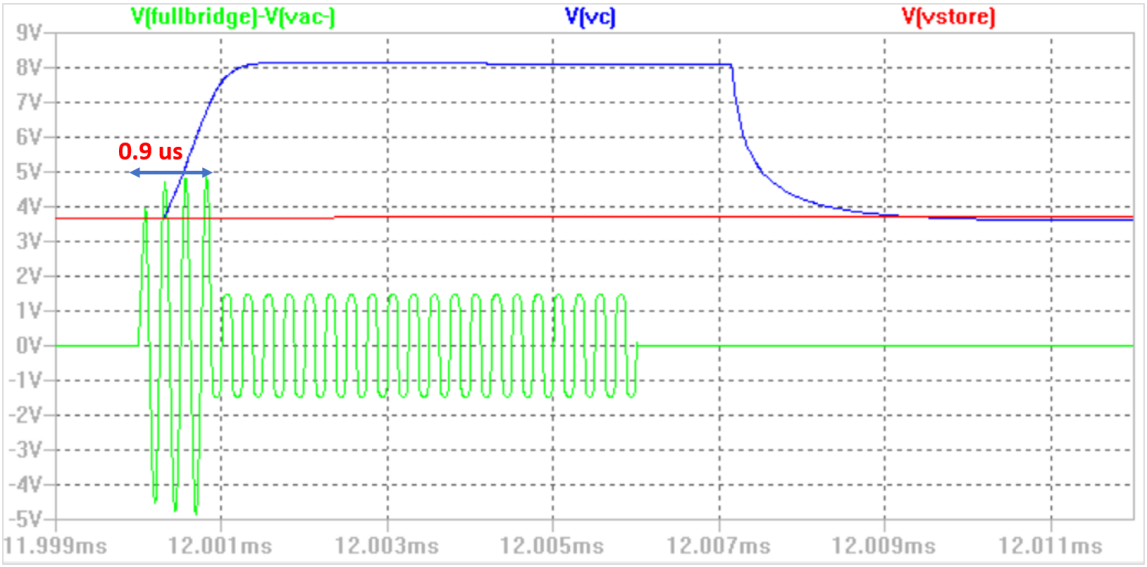


Figure 3.11: Modulated waveform ($V_{fullbridge}$-$V_{ac-}$), storage capacitor voltage ($V_{vstore}$), reverse bias voltage at varactor diode with a delay of 0.9 µs for $V_{vstore}$ = 3.7 V.

### 3.3.2. Signal at uplink data telemetry circuit

The modulation circuit with ultra low power components starts working when the storage capacitor voltage is about 0.8 V. Below this voltage, the circuit doesn't have enough power to start modulation. The waveforms are measured by using a digital storage oscilloscope (DSO). Figure 3.12 shows an unmodulated signal and Fig.3.13 shows a modulated signal with a 3 µs delay. More waveforms from the circuit are given in Appendix B.

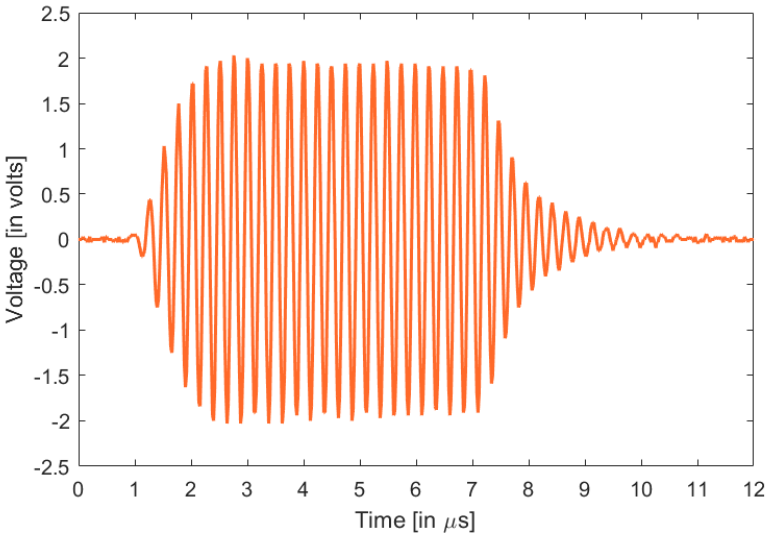


Figure 3.12: An unmodulated signal measured at the two terminals of CMUT.

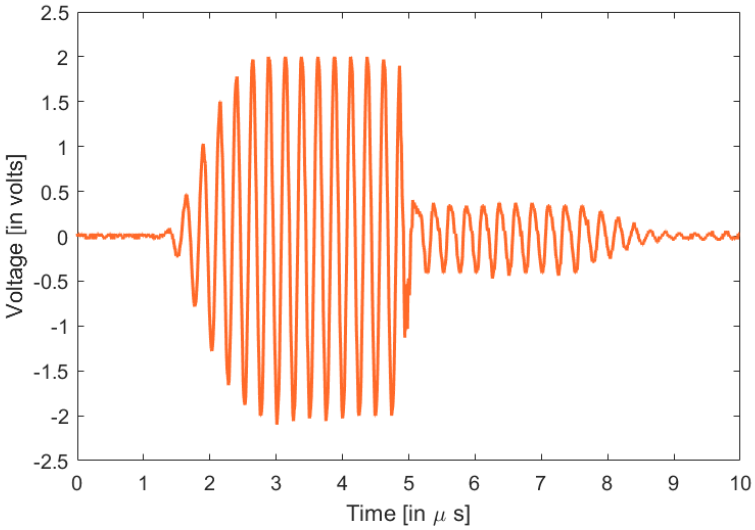


Figure 3.13: A modulated signal measured at the two terminals of CMUT.

### 3.3.3. Signal acquisition in the Verasonic

From every ultrasound burst signals that hits the CMUT array, some energy is reflected back, and this backscattered ultrasound is received by the L7-4 probe. This data can be visualized in the Verasonic. For data visualization, the Verasonic code runs a sequence of transmit, receive and process events. Transmit and receive are solely based on the hardware sequencer which is an FPGA in the Verasonic system and the process event happens in software sequencer (the host PC). The process event defines an external function in the Verasonic to acquire the RF data at all channels and to store it in the local memory of the host PC which is accessible through the MATLAB workspace. The backscattered ultrasound is collected in all of the 128 receive channels of L7-4 probe at a sampling frequency of 15.625 MHz where each acquisition takes 4096 samples. Knowing the sampling frequency, the timing of the signal is calculated. Figure 3.14 shows an ultrasound echo received at receive channel 64, which is located in the center of L7-4 probe. Ideally, the backscattered ultrasound can be considered as a complement of the signal at telemetry circuit but this is not the case in a lossy medium due to presence of scatterers and other reflectors.

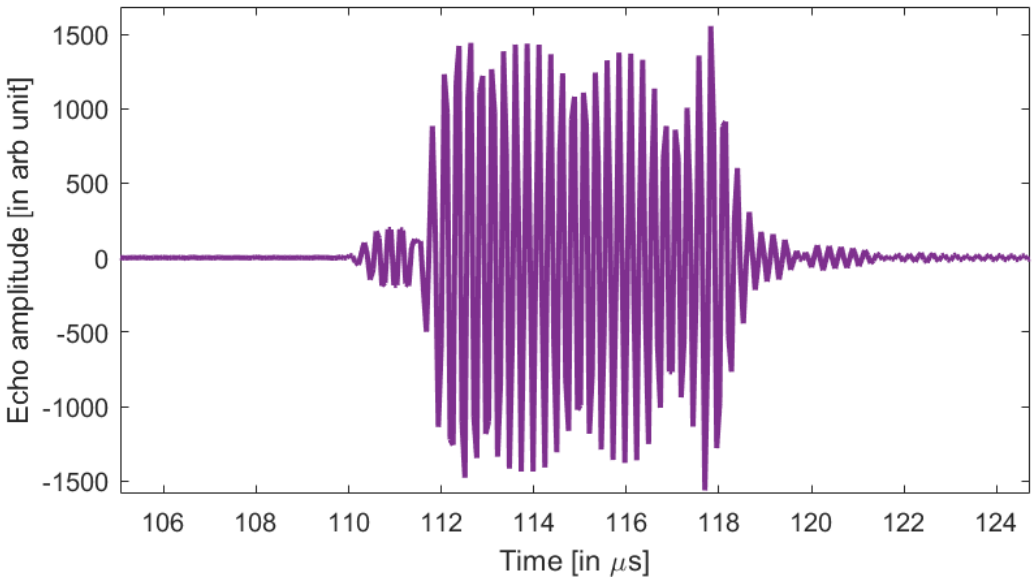


Figure 3.14: Ultrasound echo for an unmodulated signal received at channel 64 of L7-4 probe.

### 3.3.4. Signal processing

To observe the modulation in the backscattered ultrasound the difference of two consecutive bursts is calculated. This takes place in the external function defined in an Verasonic MATLAB environment. Unmodulated and modulated echoes are difficult to differentiate in a lossy medium, so taking the difference can filter out any unwanted noise, and it can be assured that the signal is from the CMUT given the pulse repetition time is 1 ms. A Hilbert transform is applied to the difference signal which results in the envelope of the signal. The signal processing toolbox in MATLAB was utilised for this task. Next, the absolute value of the envelope is calculated. Figure 3.15 shows two consecutive bursts, signal N (unmodulated) and signal N+1 (modulated) with the

processing.

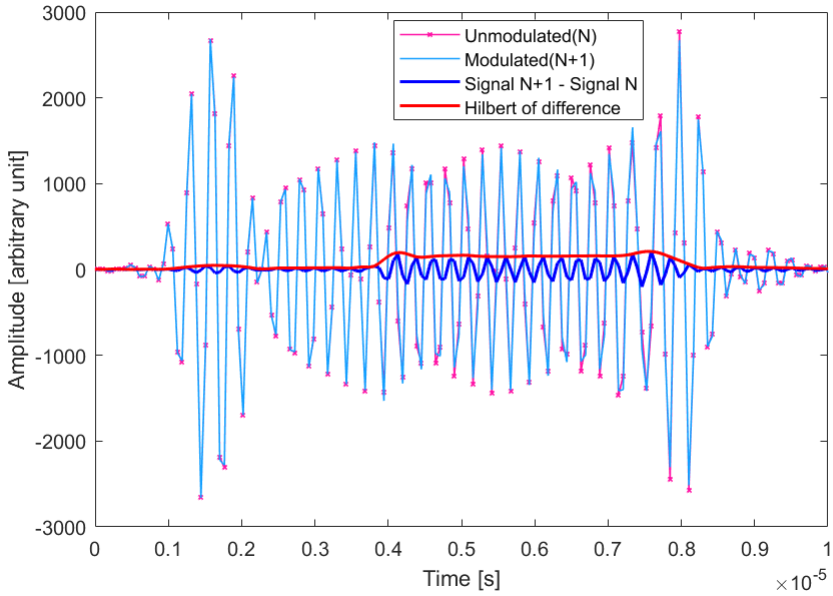


Figure 3.15: a) Unmodulated echo; b) modulated echo; c) difference between the two signals; c) absolute value of envelope of the signal visualized in MATLAB.

Once the envelope is calculated, the pulse width variation based on supply voltage can be determined. The envelope pulse width is calculated by detecting the first and last instance of 0.3 times*(peak value of envelope). This threshold was chosen such that it would not take into account spikes from noise. The $\tau$(Vcc) is delay observed in the circuit and the envelope visualized in the Verasonic has a pulse width given by $T_{burst}$ - $\tau$(Vcc) where $T_{burst}$ is the duration of burst signal (6 µs). Signals powered with different supply voltages including 6.5 V, 8.5 V, 10.5 V and 12 V were given from Verasonic to the CMUT. Then, the pulse width differences of the envelopes of two consecutive signals (one modulated and the next unmodulated) were determined in MATLAB and Fig.3.16 shows the results. As the storage capacitor voltage increased due to increased power transmitted from L7-4 probe, the delay decreases and therefore envelope pulse width increases. Here, a variation of 2 µs can be observed due to change in voltage.

The relation between the envelope pulse width and the storage capacitor voltage is given in Fig.3.17 and can be expressed as $V_{store}$ = 0.15*(PW) + 0.75 (with correlation coefficient, $R^2$=0.99). Envelope pulse width from a value of 0.35 µs to 1.96 µcan be detected. For instance, if the pulse width detected is 1.55 µs, then it can be concluded that the storage capacitor voltage is 1 V. It can be seen that this detection can occur only when the circuit has received minimal power (in this case, 0.8 V). Once powered, the pulse width mostly varies linearly with the storage capacitor voltage. After a pulse width of 2 µs, the delay in the circuit does not change anymore. The storage capacitor voltage does increase slightly if a higher supply voltage is given but this doesn't affect the delay anymore.

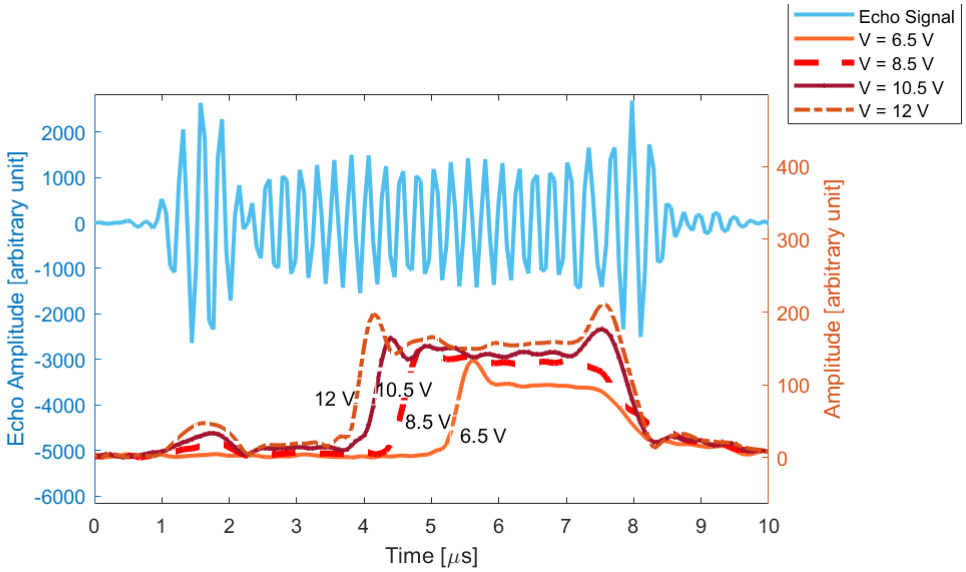


Figure 3.16: The left of y-axis corresponds to an echo signal for reference, the right of y axis has the envelope of difference of two consecutive signals for different input voltages and pulse width variation is evident.

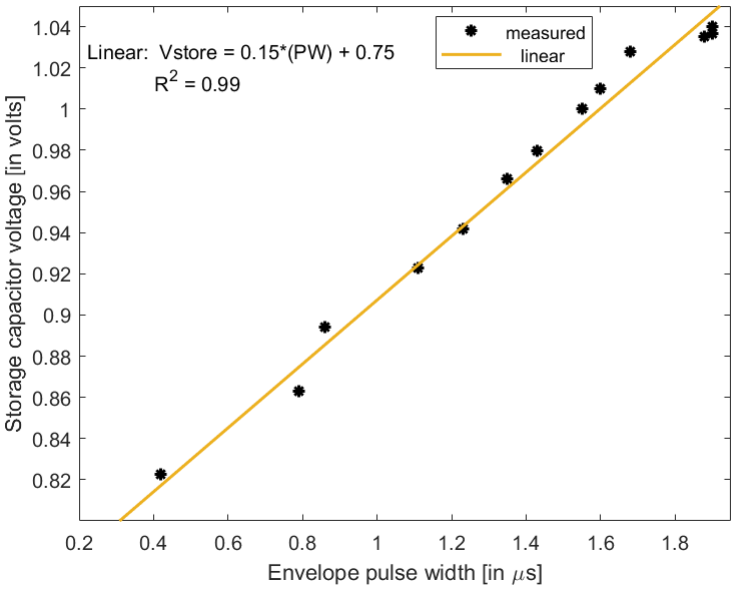


Figure 3.17: Relation between the envelope pulse width and the storage capacitor voltage.

## 3.4. Discussion and conclusions

An uplink telemetry circuit was designed to send the energy status of an implant using pulse width variation on the backscattered ultrasound. The circuit consumed less than 0.5 µW and a voltage as low as 0.8 V. The circuit exploited two types of modulation for uplink communication; by shunting and opening the CMUT, amplitude modulation (load impedance variation) and PWM based on delay variation over voltage. In the measurements done to check the pulse width as a function of different supply voltages given from the Verasonic, apart from PWM, an amplitude modulation is also seen. This is due to the fact that an increased voltage from the transmitter tends to increase the echo intensity. Variable capacitance diodes were used to modulate the pulse width. According to simulations, the delay variation should be between 2.2 µs and 6.7 µs given the time constant constituted by two diodes and a 100 k$\Omega$ resistor, but a delay change from 4 µs to 6 µs was observed in the measurements. Therefore, the range of detecting different storage capacitor voltages was limited by this. This range reduction may have been due to parasitic capacitances from the PCB or due to a 1 M$\Omega$ measurement probe connected to DSO. A small noticeable change in the delay was seen when multi-meter was connected to measure the storage capacitor voltage. Nevertheless, a linear relation between envelope pulse width and storage capacitor voltage was established using this circuit.

# 4

# Automatic implant localization

In this chapter, an algorithm is developed that automatically finds the optimal focus and steering angle settings so that a maximum amount of power is transferred to the CMUT ultrasound power scavenger.

## 4.1. System overview

A close up of the experiment setup with a 10 cm rectangular shaped tissue phantom between probe and the CMUT can be seen in Fig.4.1). Figure 4.2 shows a schematic overview of the setup. The waveform parameters such as frequency of wave, pulse cycles, pulse repetition frequency remains the same as mentioned in Chapter 3.

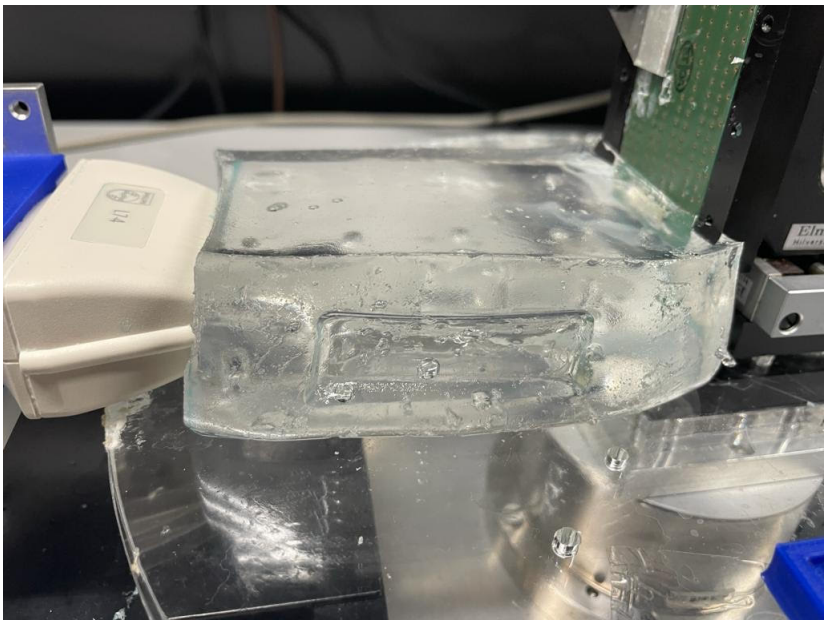

Figure 4.1: Close up of the setup.

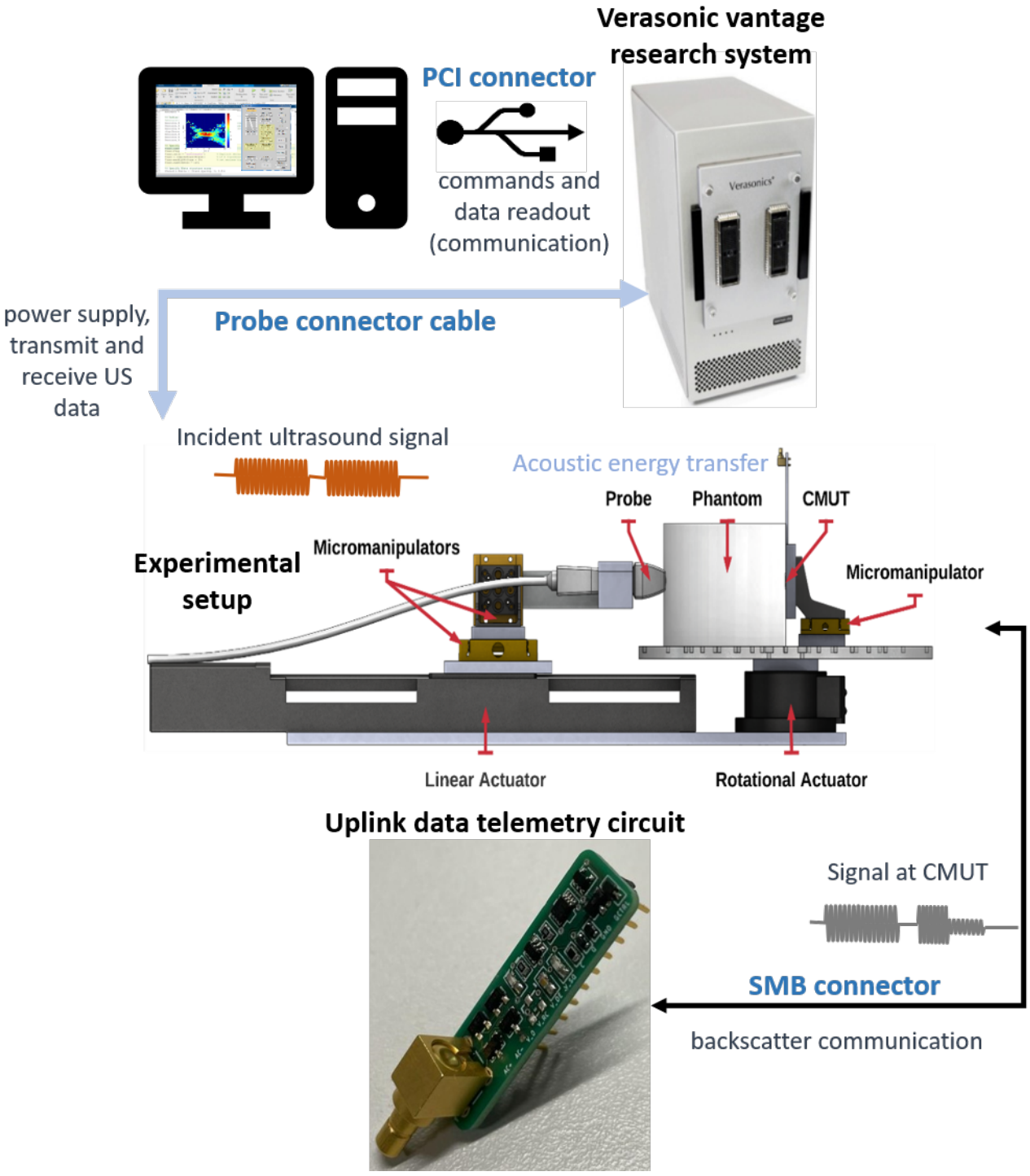


Figure 4.2: The host PC communicates with the Verasonic using a PCI connector; the L7-4 probe gets power and commands from and gives ultrasound echo data back to the Verasonic through the 128 channel containing connector cable; the Verasonic has two 128 channel connector slots; the experimental setup showing alignment of probe and CMUT; CMUT connected to the uplink data telemetry circuit (Setup courtesy : Youri Westhoek).

## 4.2. Verasonic system components

Figure 4.3 shows the hardware components in the Verasonic system which has different modules that are interconnected to each other.

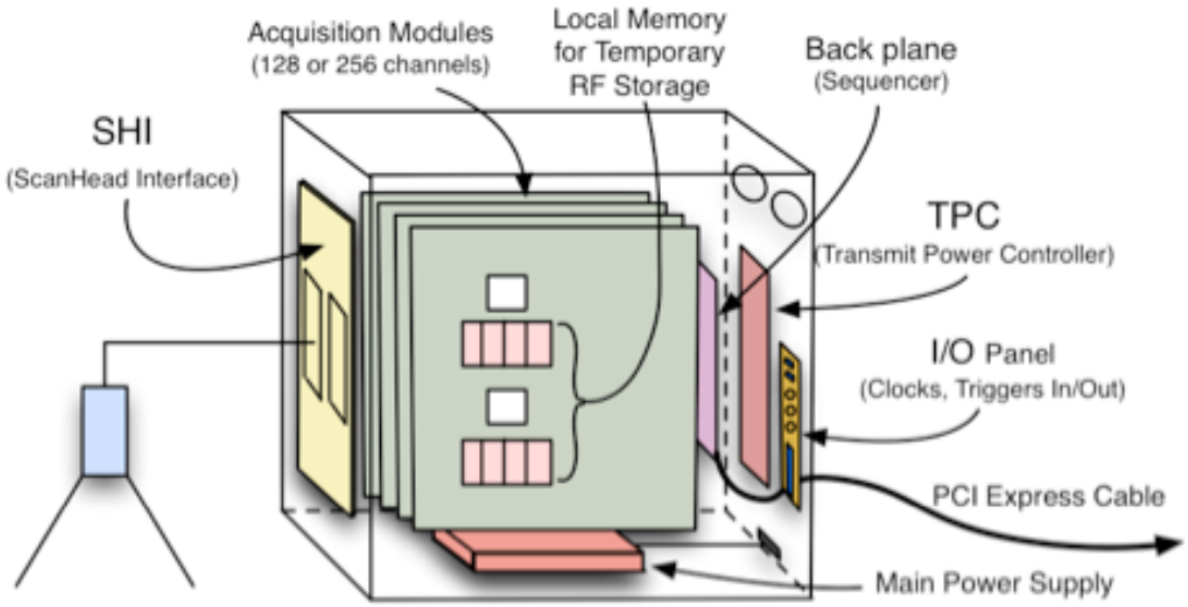


Figure 4.3: Hardware components of a Verasonic vantage ultrasound system [11].

A scan-head interface (SHI) consists of two transducer connector slots where a 64 or 128 channel transducer can be connected. In this experiment, a 128 channel L7-4 probe is connected. The acquisition module contains electronic circuits that control the transmit and receive delays and also does filtering and conditioning of the acquired data. It includes local memory for temporary storage of ultrasound data (RF-Data). The back plane comprises the hardware sequencer which gives commands to the acquisition module for its functioning. Most importantly, this module connects the host PC with the acquisition module for data transfer through Peripheral Component Interconnect (PCI) bus. The Transmit Power Controller (TPC) powers the external probe with a voltage specified in the Verasonic Scripts execution (VSX) GUI. The input/output panel (I/O) can be used for external clock/ trigger signal from other devices.

## 4.3. Script execution

To execute the beamforming script, structures and global parameters need to be defined for sequential program execution. These objects define the attributes required for running the Verasonic script. The global objects include the resource parameters that define the storage buffers in the local memory. RcvBuffer acts as the memory buffer to store acquired ultrasound echo data from all 128 channels. ImgBuffer usually consists of multiple acquisition data that can be used for image reconstruction. Information about the transducer used (L7-4), frequency of operation, delay computation is given in the 'Trans' structure. The 'Media' structure is used for simulation mode only. For the event objects, important information to be specified includes the transmit waveform parameters, delays associated with each channel (since L7-4 is a 'known' transducer, Verasonic automatically computes the delay for focusing and steering);

the receive parameters including Time Gain Control (TGC) that sets the gain for the receiving amplifier; the process to be performed which is processing of echo data and the frame that needs to be processed (defined in an external function). All of these attributes are customizable. Figure 4.4 gives an overview of the event list where each event has a number of functions to be performed before it goes to the next event. The

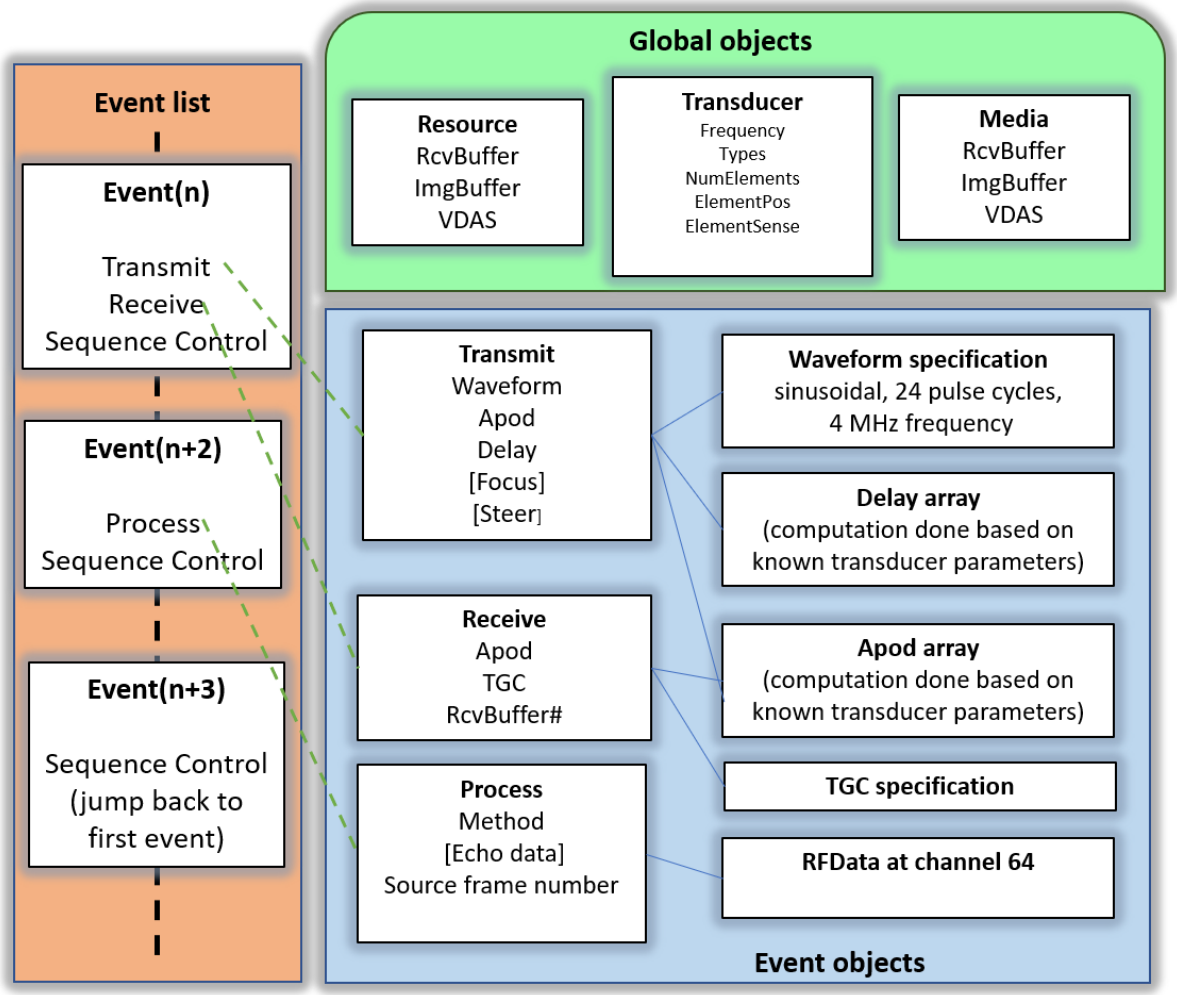


Figure 4.4: a) Event list describing the function of Verasonic in a sequential order; b) global objects to set resource parameters and providing information on the transducer used and c) different event objects with multiple parameters defined under each object required for execution of VSX script (Adapted from Verasonic Programming Manual [11], [9]).

events included in the script are transmission (TX), reception (RX), sequence control and processing. The transmission and reception are managed by the acquisition module, whereas the processing is done by the software in the host PC. The sequence control decides the flow of events in the program. The most important part of the script involves defining the 'external function'. This is a user-defined function. It is a process that has two main functions: processing of RFData and updation of the beamforming attributes.

## 4.4. Algorithm flowchart

To verify the concept of the power telemetry, a MATLAB script was written that sweeps the steering angle and focus depth of an ultrasound beam through an area surrounding the CMUT transducer. In each point the information on the storage capacitor voltage received back from the CMUT connected to the telemetry circuit was recorded and eventually collected in a so called ”heat plot”. The pulse amplitude in the Verasonic was set to 7 V. A pre-defined column vector with focus depth and steering angle values was used as input for the transmit beamforming. Each condition (TX.focus(n) and TX.steer(n)) is updated every 2 ms.

In this script, first; the transmission of an ultrasound beam with a specific focus distance (TX.focus(n)) and steering angle (TX.steer(n)) takes place. Next, the ultrasound echo is received at channel 64 of the L7-4 probe, and the hardware sequencer is updated for transmit and receive function. Finally, a ’transfertoHost’ command in the sequence control moves the received data from the RcvBuffer of the Verasonic Data Acquisition Module (VDAS) to the RcvData variable in the MATLAB workspace of the host PC. This echoed data (RcvData) is saved into a user-defined variable (prevRFData) and this operation takes place in the external function. After a 1 ms interval, another echo data is acquired and stored (currRFData). Finally, these two RFData sets are processed by the calculation of the differences in the envelopes of the two signals followed by pulse width extraction. The envelope PW is detected by taking the first and last value that corresponded to 0.3 times the maximum value of the envelope. Once, the processing is completed, the next focus depth (TX.focus(n+1) and steering angle (TX.steer(n+1)) are assigned, and this task continues until all pre-defined input parameters are updated. A color map is updated real-time for each combination and at the end of the last loop iteration, the color map gives an insight into energy received by the CMUT. It is created from a user defined matrix in which the different pulse width values measured from the received signals are stored for each location. For locations where the envelope is not detected, a null value is assigned.

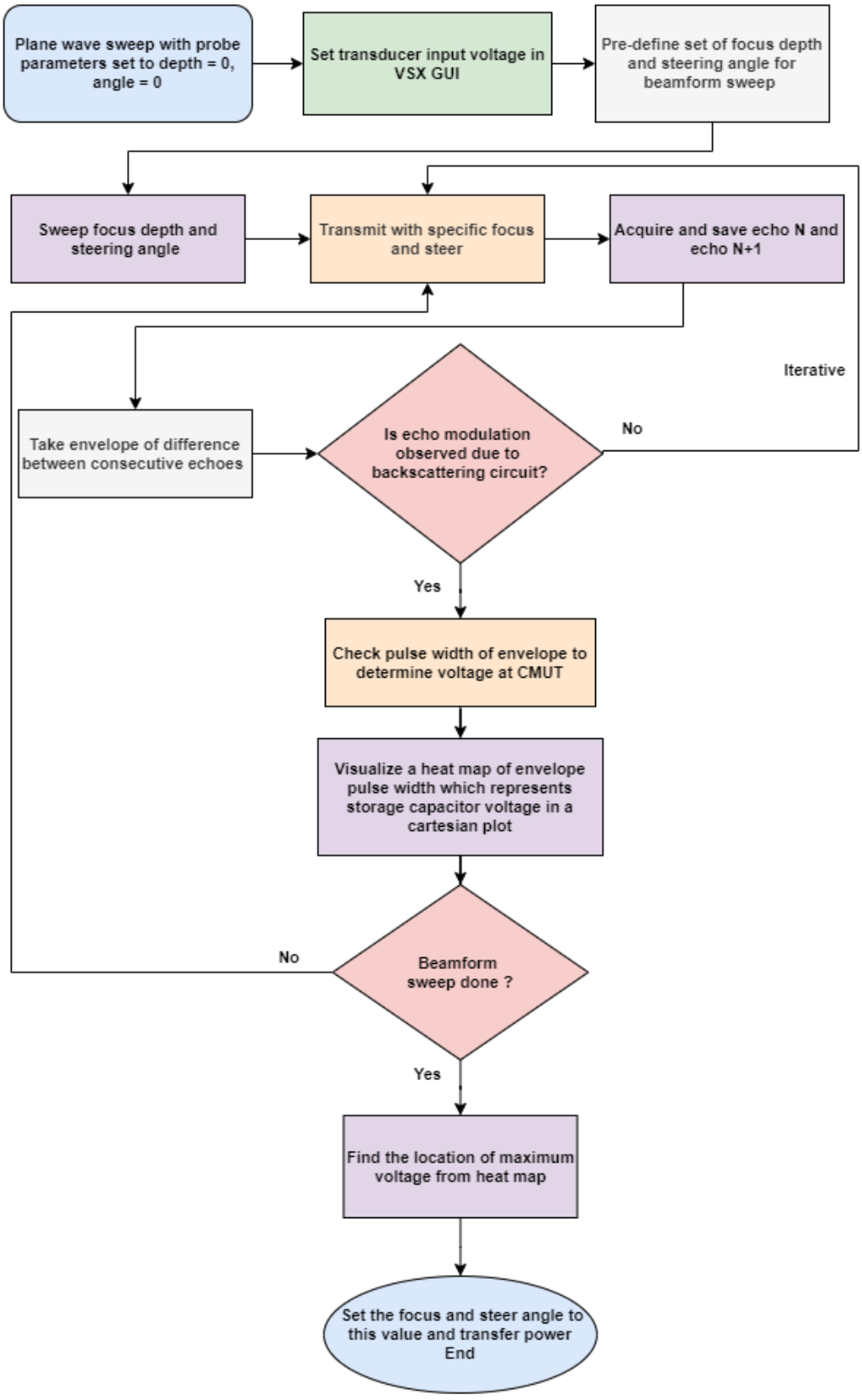


Figure 4.5: Algorithm used for ultrasound beamform sweep at different locations.

## 4.5. Results

In this section, the measured results from the ultrasound beamforming sweep are presented and compared to simulations. The user defined inputs were given in Cartesian coordinates. The distance (z-axis) was varied between 80 mm and 150 mm. The steering direction (y-axis) was varied between -2 mm and 2 mm. The measurements were initially conducted for a larger steering direction range from -1 cm to 1 cm, but it was found that the detectable signals lied in the range of -2 mm to 2 mm. There were 55 steps each between the highest and the lowest value. They are converted to polar coordinates to set the beamforming attributes. For better visualization, the results were mapped in Cartesian coordinates. With 55 steps, the map resolution for z-axis (focus) was 0.29 mm (= 70 mm/55 steps) and the y-axis (steer) was 0.07 mm (= 4 mm/55 steps).

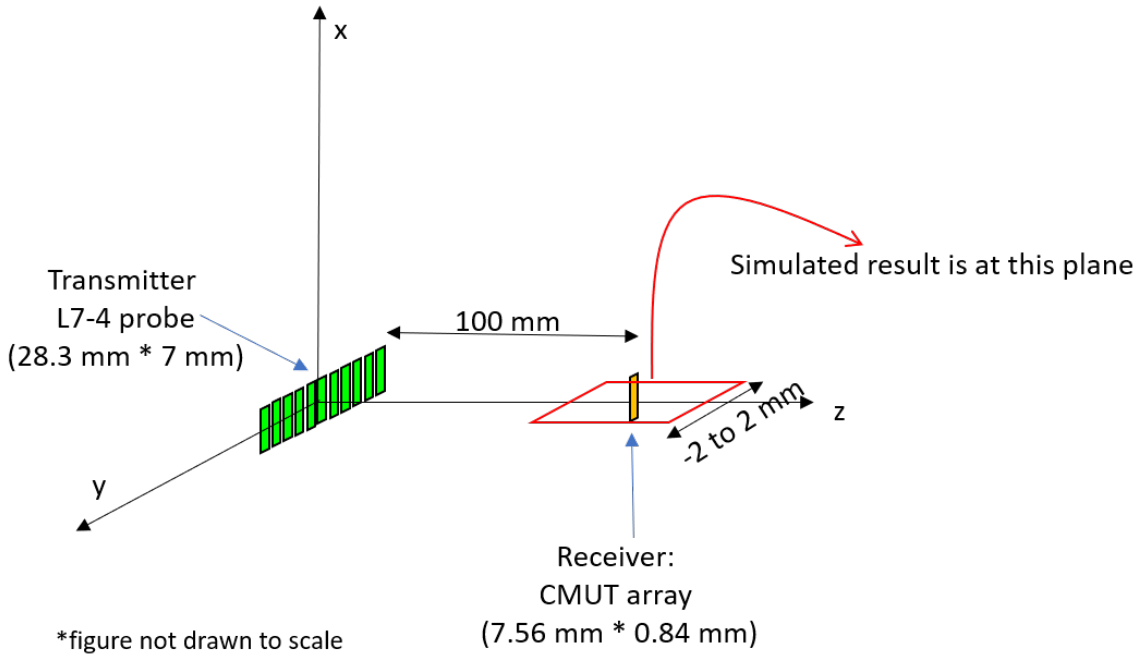


Figure 4.6: Placement of transmitter and receiver used as the basis for simulation.

A FOCUS simulation was performed to calculate the power received over the area of the CMUT. FOCUS (Fast Object-oriented C++ Ultrasound Simulator) is an ultrasound simulator that can be work in MATLAB developed by Michigan State University [64], [65], [66]. The parameters of the L7-4 probe, such as the number of channels (128), kerf width (0.025 mm) which denotes the spacing between two channel elements, aperture size (28.3 mm), and probe height (7 mm) were used to define the transmitter. The simulation was done at 4 MHz in continuous wave mode with the speed of sound set to 1409 m/s. A 2D plane was defined at 10 cm distance from the transmitter with the surface area of the CMUT used in the experiment. The simulation shows the normalized power received over the area of the transducer as a function of a parametric sweep of the focusing depth (z-axis) from 80 mm to 150 mm and for steering direction (y-axis) between -2 mm and 2 mm. The step size for simulation was kept the same as the real-time measurements for fair comparison. Figure 4.6 illus-

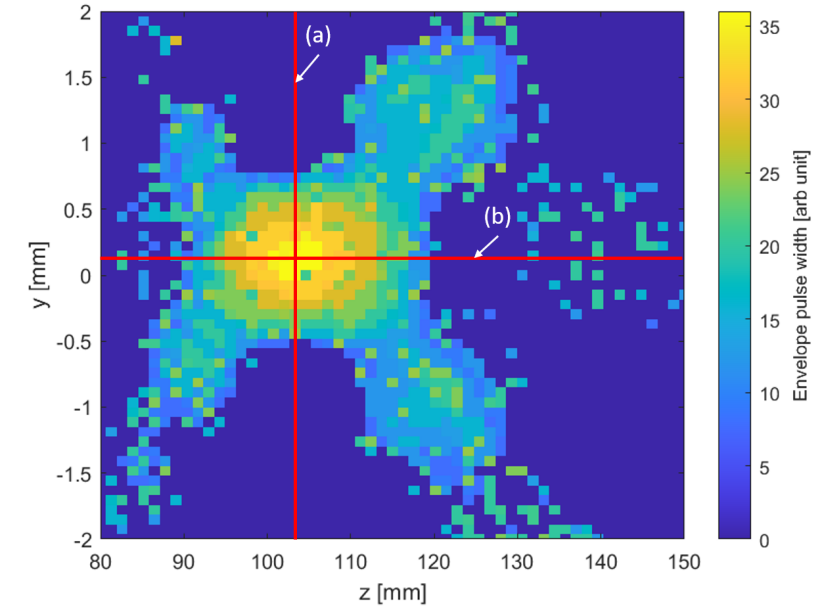


(a)

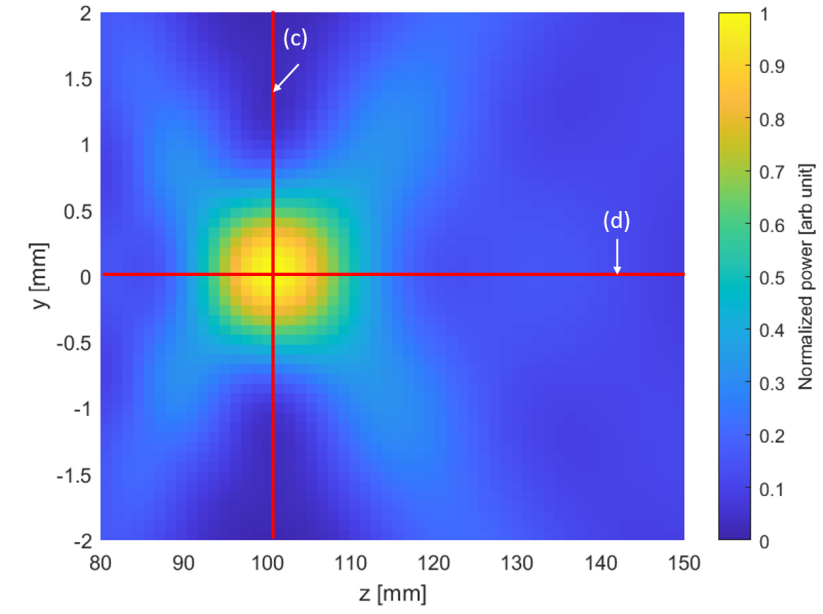


(b)

Figure 4.7: (a) Envelope pulse width measured at different locations; b) Simulation results of the normalized power received on a plane with the surface area of the CMUT. Both represent the received power over the CMUT at each location. The red lines labelled from (a) to (d) are used to find the -3 dB width in z-axis and y-axis and their results are explained below.

trates the placement of transmitter and receiver for the simulation. A lossless medium with no attenuation was assumed in the simulations.

Figure 4.7a shows the results of the received pulse widths on different locations of the focus and angle sweep. The maximum value in the heat plot is 36 (sample number), converting it into time using a sample frequency of 15.625 MHz gives 2.24 µs. So, the maximum pulse width was found to be 2.24 µs, which corresponds to a storage capacitor voltage of 1.09 V. The maximum value was observed at multiple points near the actual focus depth. One of the locations where this PW was found is at (102.5 mm, 0.15 mm). Figure 4.7b shows the FOCUS simulation results for the parametric sweep over a plane showing the normalized power received over the area of the CMUT. In the simulations, the maximum power received is when the ultrasound beam is exactly focused at the CMUT transducer.

There is a great similarity between the measurement and simulations results. Apart from the main lobe where there is a high correlation between the measurements and simulations, some side lobes can be seen in the measurements that are not fully filled compared to the simulation. In the simulations there is a smooth transition between the side lobes and rest of the simulation plane, but in case of the measurements, this transition is abrupt. This is caused by the fact that in the dark blue regions the CMUT does not receive enough energy to work correctly at all. The high intensity region in the measurement takes an elliptical shape whereas this area has a circular shape in the simulations. This might be due to a slight offset in the alignment of the probe to the CMUT receiver during the measurements.

The half power width along the focus and steer direction were compared between simulation and measured data. In Fig.4.7a and Fig.4.7b, the red lines labelled (a) to (d) represent lines passing through the point of maximum power (located in the center) so as to determine the half power width. For simulation, maximum power transfer location was at (0 mm, 100 mm) and for measured data (0.07 mm, 100.74 mm). For good comparison, the measured data has been normalized.

Figure 4.8a shows normalized amplitude for the measured and simulated data over y-direction. The -3 dB width in the steering direction was 1.05 mm for the measurement data and 1.15 mm for the simulations. The curve fit is similar except for the bottom region where the graph is smooth in simulation and not so in the measurements. The plot width is narrow given the half power width along y direction is 1.15 mm. It can be implied that CMUT is sensitive to steering and can work well only within a small range. This can also be seen in the heat map where as the focus gets narrow in the center. Figure 4.8b shows normalized amplitude for the measured and simulated data over z-direction. The -3 dB width along z-direction was found to be 18 mm for the simulation and 25 mm for the measured data. The curve trend is similar but there are some peaks observed on either sides of measured data that are smooth in the simulation. This is due to the circuit not having enough power to transmit and therefore, the plot had a null value. The measured data plot is wider than the simulated plot which could be due to the offset of 0.07 mm.

To summarize, the power received by the CMUT becomes half the maximum value when the elliptical shape near the natural focus has its minor axis set to 1.15 mm and major axis to 25 mm. Therefore, it must be beamformed within this region (to achieve power transfer without much degradation.

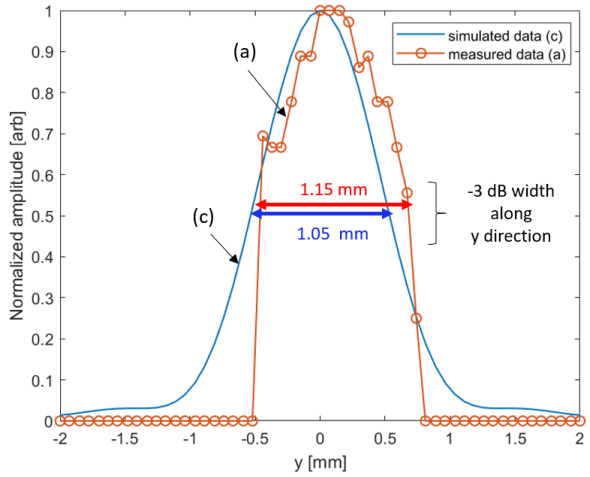


(a)

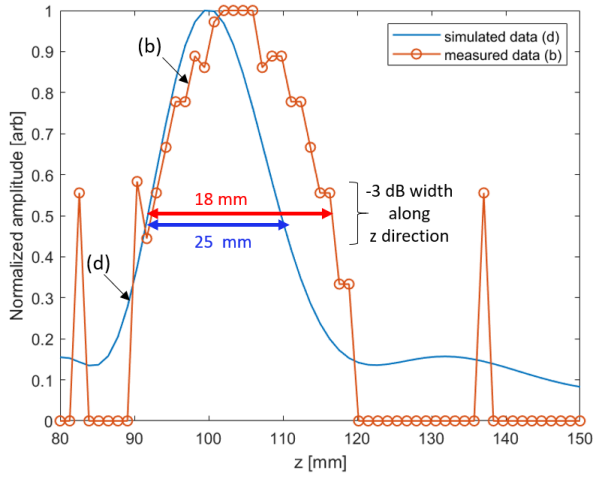


(b)

Figure 4.8: a) Normalized power in y-direction when z is set to 100 mm with -3 dB width in steer direction set to 1.15 mm for measured data and 1.05 mm for simulations; b) power plot when y is set to 0 mm with -3 dB width in focus direction to be 18 mm for simulations and 25 mm for measured data. The labels marked from (a) to (d) refers to the red lines in the heat plot that gives the location at which these plots are visualized.

## 4.6. Discussion and conclusion

To verify the concept of the power telemetry a MATLAB script was written that sweeps the angle and focus of an ultrasound beam over an area surrounding the CMUT transducer. In each point the information on the voltage on the storage capacitor received back from the CMUT connected to the telemetry circuit was recorded and eventually collected in a so called ”heat plot.” It was found that the maximum voltage occurred at multiple locations around the natural focus and sending bursts at any of these locations transmitted maximum energy to the CMUT. A comparison of measurements and simulations showed a good correlation. But, there were regions in the measured heat plot where the data was not fully filled compared to simulation. The reason is that the CMUT didn’t receive enough power to start the uplink communication.

This work can be used as a basis to further develop a tracking algorithm that should be able to locate and follow the implant as either the probe or the implant is moved.

# 5

# General conclusion and recommendations

## 5.1. Conclusion

Ultrasound has been used to wireless power deep implants. In this work, first, a simple low power uplink telemetry circuit that can establish initial contact with the implant was designed. This circuit sends information on the implant's supply voltage using pulse width modulation and amplitude modulation of the ultrasound echo. A pre-charged CMUT was used as the ultrasound energy scavenger. It was found that the pulse width variation has a more or less linear relationship with the storage capacitor voltage in the uplink telemetry circuit. Therefore, it was possible to successfully determine the voltage of the storage capacitor based on the pulse width. The variation in load impedance, which constituted the amplitude modulation occurred due to a change in the reflection coefficient of the acoustic energy. Secondly, the effect of impedance on acoustic energy was investigated and a significant change in reflection of upto 40% was observed between matched and mismatched load conditions. Finally, a good alignment between probe and the receiving transducer is necessary to establish a robust power link, therefore, a 'heat plot' was generated using the Verasonic by sweeping the focus depth and the steering angle to find the location at which maximum power transfer takes place. It was found that the optimum power transfer is very critically dependent on the steering angle and less of the focus depth.

## 5.2. Future work

Recommendations for the future work:

- To even further reduce the power consumption and the size of the circuit it is recommended to design a dedicated application specific integrated circuit (ASIC) rather than to use off the shelf components;
- Based on the findings in this thesis a tracking algorithm can be developed that can actively track the implants when either the ultrasound probe or the implants in the patient is moving;

- After initial contact is made to the implants a communication protocol needs to be developed to send and receive data to and from the implant.

### 5.2.1. New uplink telemetry protocol

Once the optimization of the focus depth and the steering angle are done by performing the localization algorithm, it can be concluded that the implant now receives enough energy. At this point, the circuit should autonomously decide to switch to another circuit (digital) that could take over the uplink communication to send information. A pulse width modulation scheme similar to the one used in the initial circuit can be used to accomplish this telemetry protocol. The receiver outside the body must be able to differentiate if the received signal is from the simple circuit or the digital circuit. Normally, it can be assumed that the pulse width variation in the simple circuit will only have a short difference between two sets of consecutive echoes, given the probe is not abruptly moved. For the new telemetry protocol, a simple header consisting of four pulses with short, long, short, long pulse width duration can represent the beginning of the data being sent from the digital circuit. So, the receiver can check for this header to know from which circuit the data is coming. If the digital circuit is working, then there are always four pulses which constitute the header followed by eight pulses of data (for instance) which could be the information regarding implant's stimulation status or physiological sensing data. Therefore, defining a unique header can be a way to identify the circuit. The receiver can identify this using the protocol shown in Fig.5.2. For instance, it can constantly check if there is large difference of pulse width between twelve pulses. If yes, then it mostly originates from the new circuit and therefore it waits and checks for a header. Once the header has the said duration of pulses, then it starts to receive data for the next eight pulses. If the header does not exist, then it waits for another 12 set of pulses and checks again. In case the twelve pulses do not have much pulse width variation between each other, then it can be concluded that the data is from the initial telemetry circuit. It could happen that the communication is lost and an automatic reset could be programmed to look for the data again.

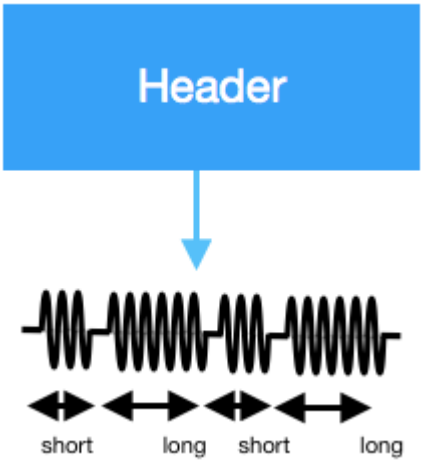


Figure 5.1: An example of a header that is sent from implant as a pre-cursor for identification of upcoming data transfer from the digital circuit.

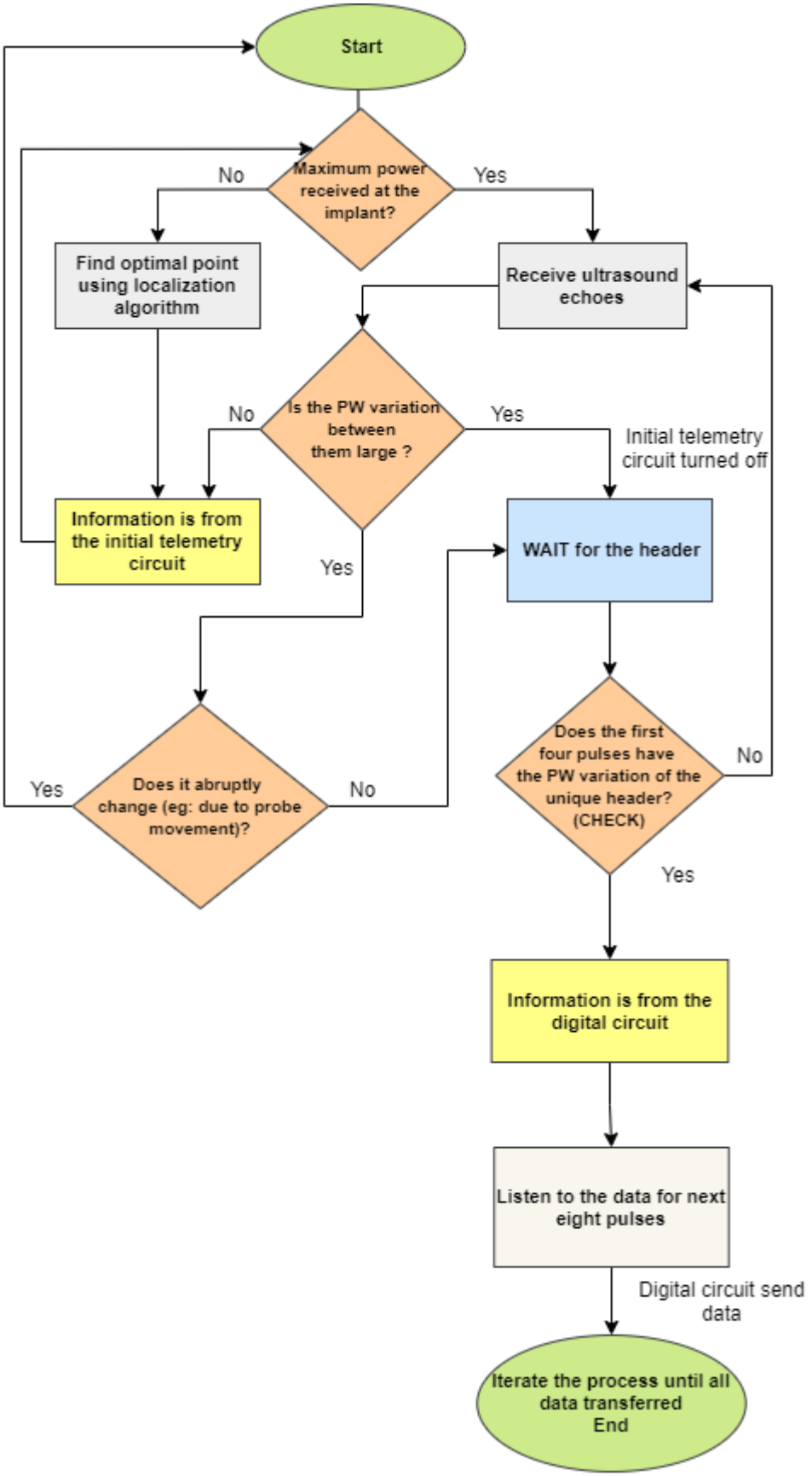


Figure 5.2: The proposed tracking algorithm that can form a closed loop system.

### 5.2.2. Proposed localization algorithm

A tracking algorithm that can follow the implant to find the optimal point should be implemented such that any movement made due to a person's breathing or due to the probe, does not affect the power transfer efficiency, given the probe is in the vicinity of the implant. A heat plot created in this work shows maximum power transfer location and the area around this point can be further tracked down by steering and focusing the ultrasound beam around that value. Figure 5.3 shows the flowchart for the proposed tracking algorithm.

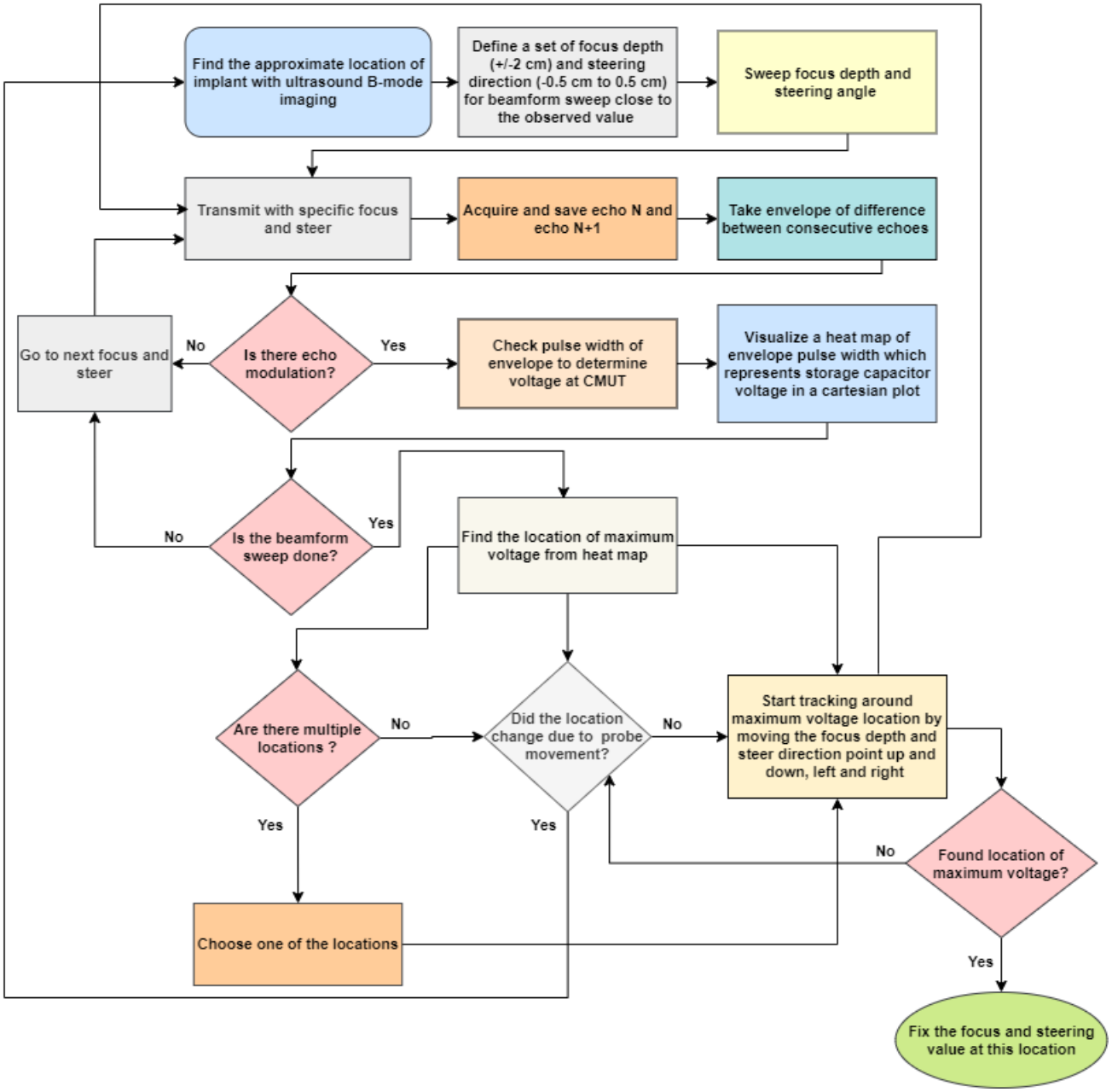


Figure 5.3: Proposed algorithm for localization of an implant using the uplink data telemetry circuit.

# A

# Appendix

## A.1. PCB schematic and layout

In this section, the schematic and layout design done for the uplink data telemetry circuit is given (see Fig.A.1 and Fig.A.2). The dimensions of the final PCB is 35.56 mm * 10 mm.

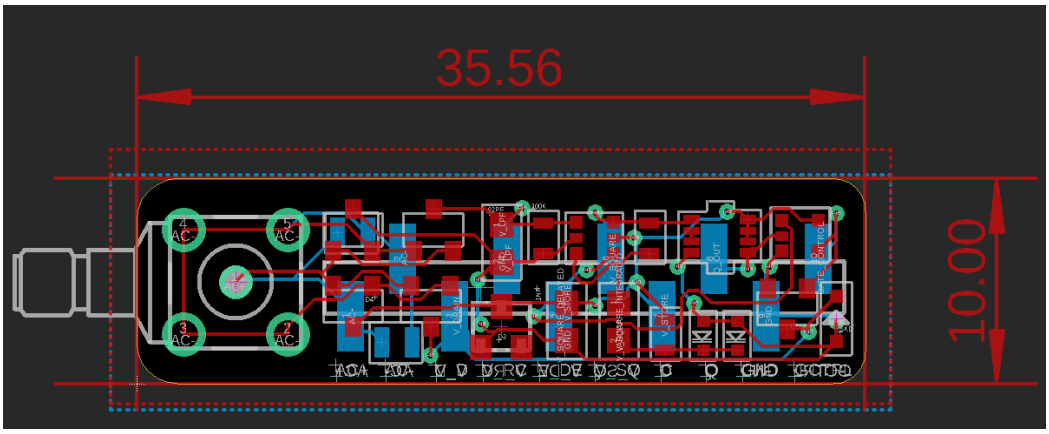


Figure A.1: PCB layout for the uplink data telemetry circuit.

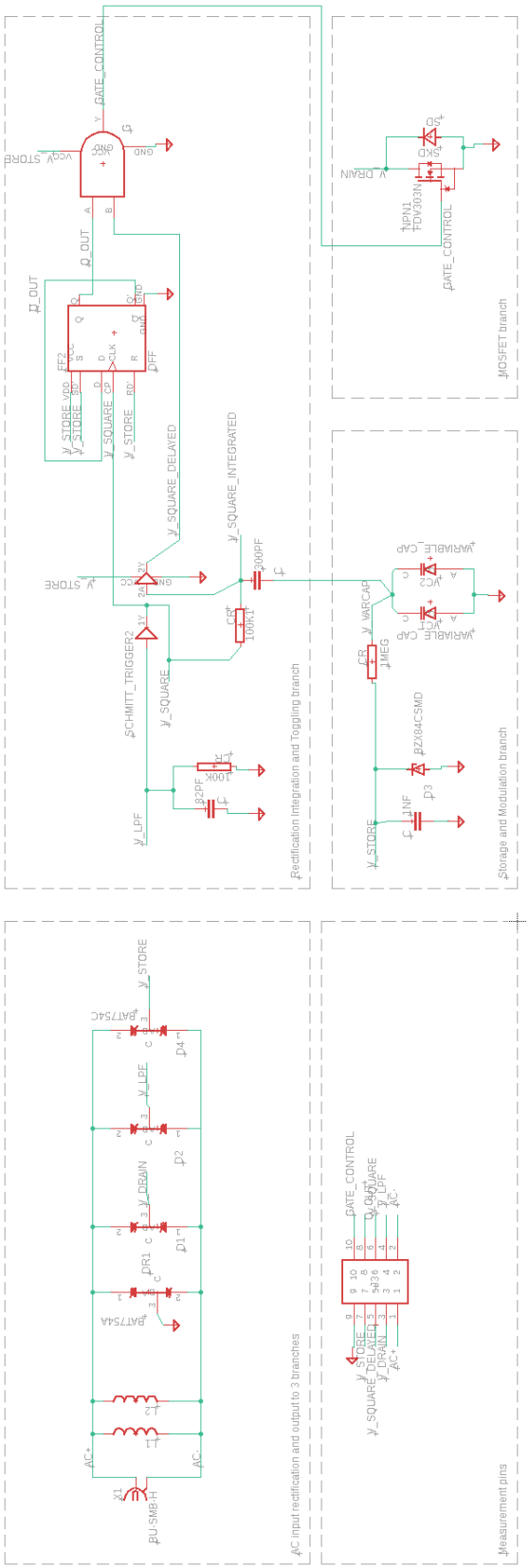


Figure A.2: Schematic for circuit done in EAGLE PCB design software.

## A.2. Waveforms from the telemetry circuit

Figure A.3 shows the output of ST1 ans ST2 from the circuit. Figure A.4 shows AND gate output where it is high only for one of the two burst signals.

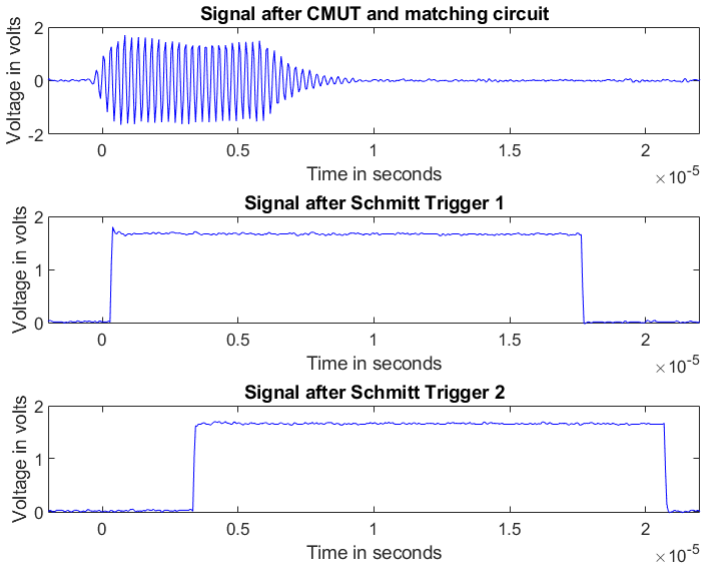


Figure A.3: a) Input burst signal b) Schmitt trigger (ST1) output c) Schmitt trigger output (ST2) after the integrator.

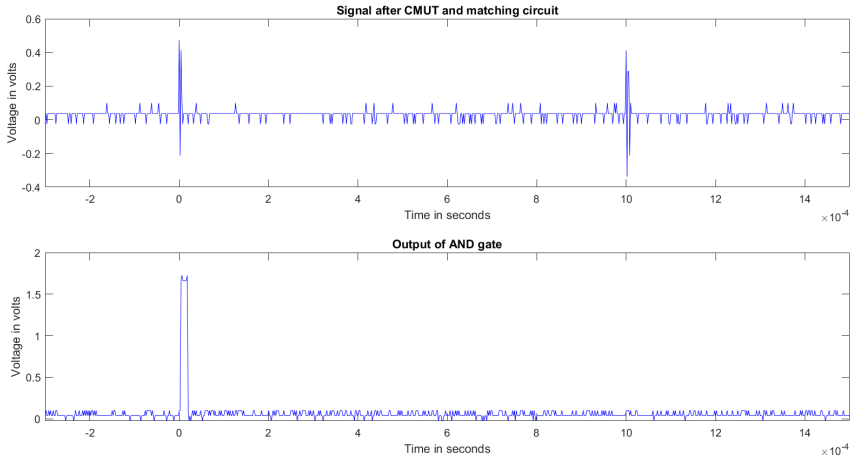


Figure A.4: a) Input burst signal b) AND gate output with PRF of 1 kHz.

## A.3. Power consumption in uplink data telemetry circuit with HWR

The initial circuit was built on the perforated board with half wave rectifier (HWR). The power consumption of HCT series of logic circuits was 1.4 µW. Figure A.5 and its picture is given in Fig.A.6.

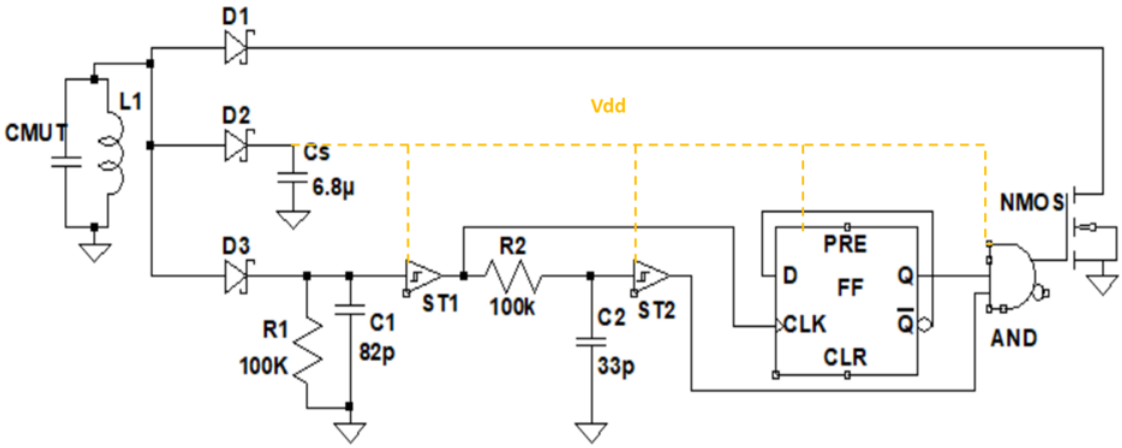


Figure A.5: Circuit diagram for the half wave rectifier

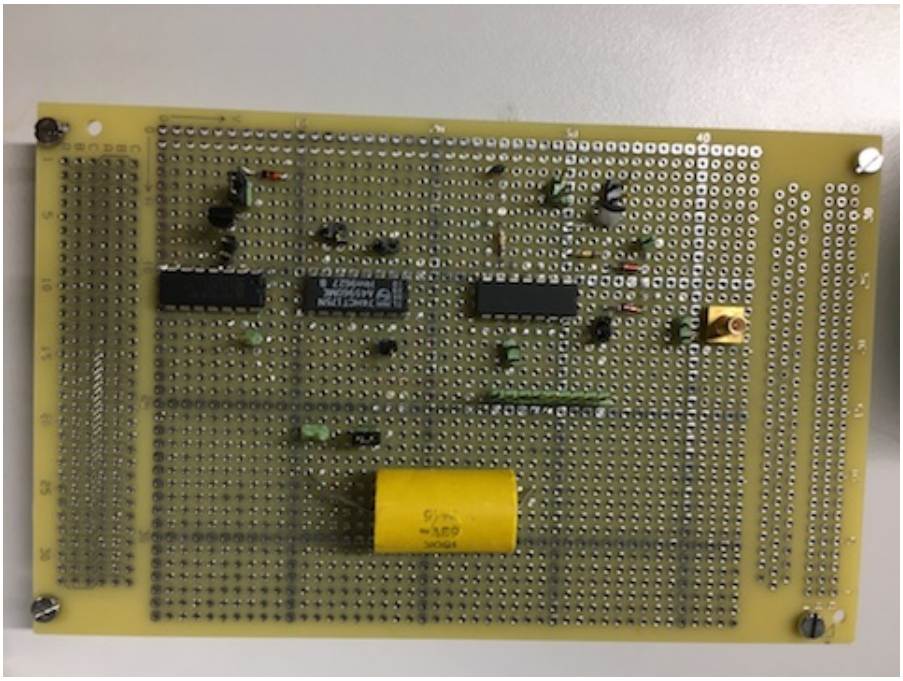

Figure A.6: Photograph of the circuit.

# B

# Appendix

Table B.2, B.3, B.4, B.5, B.1 shows an overview of publications which were part of the literature research.

Table B.1: Comparison of deep implants powered by ultrasound [12], [13]

| Author | Depth (mm) | Telemetry | Data transferred | Modulation scheme | Medium | Method for uplink | Beamforming and implant localization method (if any) | Transmitting system | Transmitting transducer | f (MHz) | PW (µs) | Receiving transducer | Functionality | Bio-compatibility | Implant size |
|---|---|---|---|---|---|---|---|---|---|---|---|---|---|---|---|
| Gulick 2012 | 65 | no | voltage at implant | none | pork | volume conduction from dipole- detection of evoked skin potential and imaging using ultrasound | yes | TTL pulse generator | piezoelectric disc | 1 | not provided | piezoelectric | nerve stimulation | no | 9.9 $mm^2$ |
| Chang 2017 | 85 | yes, duplex, 95 kB/s | pseudo random binary sequence , 1 and 0 | OOK | castor oil, animal tissue @ 6 cm | backscatter depending on FSM and frequnecy generator | yes, manual transmit beamforming | signal generator | external PZT | 1 | burst | PMN-PT | closed loop system for therapies | no | 30.5 $mm^3$ |

Table B.2: Comparison of deep implants powered by ultrasound [14], [15], [16], [17], [18]

| Author | Depth (mm) | Telemetry | Data transferred | Modulation scheme | Medium | Method for uplink | Beamforming and implant localization method (if any) | Transmitting system | Transmitting transducer | f (MHz) | PW (µs) | Receiving transducer | Functionality | Bio-compatibility | Implant size |
|---|---|---|---|---|---|---|---|---|---|---|---|---|---|---|---|
| Ghanbari 2020 | 20 | yes | echo amplitude | AM | oil | load modulation, 100 Ω and 800 kΩ | yes, location known | ultrasound pulser (Maxim, MAX14808), function generator | single-element external transducer (Olympus V323-SU) | 1 | 10 | piezoceramic resonator | bio-sensing | no | 0.32 $mm^2$ |
| Chen 2020 | 30 | yes | digital information 1 and 0 | ASK | oil, porcine tissue | load modulation | already known | signal generator | piezoelectric | 1 | 56 | triboelectric | power delivery and uplink communication | no | 50 um diameter |
| Chang 2019 | 65 | yes | voltage at implant | OOK | castor oil | notch detection due to pseudo random binary sequence generated at implant | yes, depending on voltage at implant | pulser controlled by a Xilinx Zynq SoC | PZT | 0.97 | 50 | PMN-PT-rx, PZT4-tx | networking between multiple implants | no | 0.25 $mm^2$ |
| Zhang 2019 | 71 | yes, bi-directional | ASCII data such as device ID | ASK | castor oil | load modulation | yes, through ultrasound imaging | Verasonic ultrasound research system | L3-12 linear array PZT probe | 4 | 1 | piezoelectric | bio-sensing | no | 11 $mm^2$ |
| Wang 2019 | 60 | yes, uplink | echo intensity | AM | mineral oil | load modulation | yes, using TDoA and uplink information | Verasonic vantage 256 scanner | P4-1 linear array PZT probe | 1 | 25 | PZT4 | implant localization for power transfer | no | mm range |

Table B.3: Comparison of deep implants powered by ultrasound [19], [20], [21], [22], [23]

| Author | Depth (mm) | Telemetry | Data transferred | Modulation scheme | Medium | Method for uplink | Beamforming and implant localization method (if any) | Transmitting system | Transmitting transducer | f (MHz) | PW (µs) | Receiving transducer | Functionality | Bio-compatibility | Implant size |
|---|---|---|---|---|---|---|---|---|---|---|---|---|---|---|---|
| Weber 2018 | 120 | yes | digital information 1 and 0 - time multiplexed | OOK | castor oil | load modulation | yes, location known | signal generator | single element PZT transducer | 1 | burst | piezoelectric | pressure sensing | no | 30.498 $mm^3$ |
| Song 2015 | 200 | no | none | – | water | – | no, omnidirectional | not provided | PZT | 2.3, 1.15 | 0.15 | piezoelectric | power delivery | no | 11 $mm^2$ |
| Mazzilli 2016 | not provided | yes, 50 kB/s | echo intensity | OOK/ASK | not provided | load modulation | location known | not provided | PZT | 1 | not provided | PZT | power delivery | no | not provided |
| Larson 2011 | 100 | no | none | – | sciatic nerve of a rat | – | yes, perpendicular positioning of probe to implant | TTL pulse and function generator | PZT | 1 | 100 | PZT-5A | nerve stimulation | no | 8 mm long |
| Ghanbari 2019 | 50 | yes, uplink | neural recording state | AM | tissue phantom | linear analog echo modulation through change in impedance | unfocused beam | pulser | single element PZT transducer | 1.78 | not provided | PZT | neural recording, code division multiplexing for data telemetry | no | 0.8 $mm^3$ |

Table B.4: Comparison of deep implants powered by ultrasound [24], [25], [26], [27], [28]

| Author | Depth (mm) | Telemetry | Data transferred | Modulation scheme | Medium | Method for uplink | Beamforming and implant localization method (if any) | Transmitting system | Transmitting transducer | f (MHz) | PW (µs) | Receiving transducer | Functionality | Bio-compatibility | Implant size |
|---|---|---|---|---|---|---|---|---|---|---|---|---|---|---|---|
| Piech 2017 | 14 | yes, uplink | ASCII data to prove data transmission | PAM | rodent | change in acoustic impedance through digitally controlled switch | yes, location already known | ARM Cortex-M4 based microcontroller with ASIC,DSP | piezoelectric | 1.8 | 3.3 | piezocrystal | generic digital encoding scheme intended for transmitting neural information | no | 18 $mm^2$ |
| Charthad 2018 | 105 | yes, downlink | stimulation parameters | PWM-AM | castor oil | – | yes | programmable signal generator | focused single-element external ultrasound transmitter (Olympus A392S) | 1.3 | ~14 - 470 | piezo- barium titanate | peripheral nerve stimulation and power delivery | yes | 39 $mm^3$ |
| Charthad 2016 | 60 | no | – | – | mineral oil | – | yes | signal generator | external ultrasonic transmitter (Olympus A303S-SU) | 1 | – | piezoelectric | localized drug delivery on electrical stimulation of drug-loaded polypyrrole nanoparticles | no | 15 $mm^2$ |
| Baltsavias 2020 | varied | yes | echo intensity | OOK | rat | load modulation | location known, focused ultrasound | signal generator | external PZT | 0.8 | 1000 | piezoelectric | gut redox monitoring | no | 72.8 $mm^2$ |
| Mazzilli 2014 | 105 | no | – | – | water, tissue phantom | – | not provided | not specified | spherical PZT array | 1 | – | PZT | wireless energy transmission | no | 50 $mm^2$ |

Table B.5: Comparison of deep implants powered by ultrasound [29], [30], [31], [32], [33]

| Author | Depth (mm) | Telemetry | Data transferred | Modulation scheme | Medium | Method for uplink | Beamforming and implant localization method (if any) | Transmitting system | Transmitting transducer | f (MHz) | PW (µs) | Receiving transducer | Functionality | Bio-compatibility | Implant size |
|---|---|---|---|---|---|---|---|---|---|---|---|---|---|---|---|
| Shi 2020 | 22 | yes, uplink | temperature data | FM | de ionized water, 3 mm thick chicken thigh | frequency component of echo corresponding to temperature data | yes, imaging | Verasonic ultrasound research system | L12-3v PZT linear array | 8.3 | 0.48 | PZT-5H | in vivo real-time monitoring of body temperature | no | 0.065 $mm^3$ |
| Wang 2017 | 60 | yes | not mentioned | FM | caster oil | transmitted data at multiple modulation frequencies from 10 kHz to 100 kHz | yes, manual transmit beamforming | Zynq system on chip (SoC). The SoC integrates an ARM processor with hardware programmable logic (FPGA) | 32-element linear phased array | 1.1 | 18 | PZT | closed loop neural recording system | no | 1.44 $mm^3$ |
| Johnson 2018 | 21.5 | yes, uplink | stimulation parameters | AM | rat tissue | load modulation | location known, unfocused high intensity beam | ASIC with microcontroller | external PZT | 1.85 | burst | single piezocrystal | wireless peripheral nerve stimulator | no | 6.5 $mm^3$ |
| Piech 2020 | 21.5 | yes, bi-directional | stimulation parameters | AM | mouse, ex vivo porcine tissue | ultrasound backscatter | location known, focused ultrasound | high-performance microcontroller (NXP LPC4370) | V306-SU-F0.85IN-PTF, Olympus NDT | 1.85 | burst | piezoceramic | rat sciatic nerve stimulation | no | 1.7 $mm^3$ |
| Luo 2013 | 50 | yes, downlink | stimulation current | OOK | rat tissue | na | yes, already known | signal generator | na | 1 | not provided | PZT | neural stimulation | no | 4.4 $mm^2$ |

# Bibliography


[1] V. W. P. Farah Laiwalla, "Next Generation Microscale Wireless Implant System for High-Density, Multi-areal, Closed-Loop Brain Computer Interfaces," in *Brain-Computer Interface Research.*, T. M. Guger C., Allison B.Z., Ed. SpringerBriefs in Electrical and Computer Engineering.: Springer, 2021. [Online]. Available: https://doi.org/10.1007/978-3-030-60460-8_4

[2] A. Fomenko, C. Neudorfer, R. F. Dallapiazza, S. K. Kalia, and A. M. Lozano, "Low-intensity ultrasound neuromodulation: An overview of mechanisms and emerging human applications," *Brain Stimulation: Basic, Translational, and Clinical Research in Neuromodulation*, vol. 11, no. 6, pp. 1209–1217, nov 2018. [Online]. Available: https://doi.org/10.1016/j.brs.2018.08.013

[3] M. Mischi, "Ultrasound beamforming," 2018. [Online]. Available: https://indico.cern.ch/event/542674/contributions/2250532/attachments/1312424/1964410/MM_Ultrasound_beamforming_Mischi.pdf

[4] R. K. Panda, "Development of novel piezoelectric composites by solid freeform fabrication techniques," Ph.D. dissertation, Rutgers The State University of New Jersey - New Brunswick, Jan. 1998.

[5] J. Charthad, M. J. Weber, T. C. Chang, and A. Arbabian, "A mm-sized implantable medical device (imd) with ultrasonic power transfer and a hybrid bi-directional data link," *IEEE Journal of Solid-State Circuits*, vol. 50, no. 8, pp. 1741–1753, 2015.

[6] H. Basaeri, D. B. Christensen, and S. Roundy, "A review of acoustic power transfer for bio-medical implants," *Smart Materials and Structures*, vol. 25, no. 12, p. 123001, nov 2016. [Online]. Available: https://doi.org/10.1088%2F0964-1726%2F25%2F12%2F123001

[7] "Capacitive micromachined ultrasonic transducers," Jun 2020. [Online]. Available: https://www.innovationservices.philips.com/looking-expertise/mems-micro-devices/mems-applications/capacitive-micromachined-ultrasonic-transducers-cmut/

[8] S. Kawasaki, Y. Westhoek, I. Subramaniam, M. Saccher, and R. Dekker, "Pre-charged collapse-mode capacitive micromachined ultrasonic transducer (cmut) for broadband ultrasound power transfer," in *2021 IEEE Wireless Power Transfer Conference (WPTC)*, 2021, pp. 1–4.

[9] "Vantage systems," Oct 2020. [Online]. Available: https://verasonics.com/vantage-systems/

[10] “Bb202 low-voltage variable capacitance diode,” January 2008. [Online]. Available: https://www.nxp.com/docs/en/data-sheet/BB202_N.pdf

[11] “The vantage advantage,” May 2018. [Online]. Available: https://verasonics.com/the-vantage-advantage/

[12] D. W. Gulick and B. C. Towe, “Method of locating ultrasound-powered nerve stimulators,” in *2012 Annual International Conference of the IEEE Engineering in Medicine and Biology Society*, 2012, pp. 887–890.

[13] T. C. Chang, M. L. Wang, J. Charthad, M. J. Weber, and A. Arbabian, “27.7 a 30.5mm3 fully packaged implantable device with duplex ultrasonic data and power links achieving 95kb/s with <10−4 ber at 8.5cm depth,” in *2017 IEEE International Solid-State Circuits Conference (ISSCC)*, 2017, pp. 460–461.

[14] M. M. Ghanbari and R. Muller, “Optimizing volumetric efficiency and backscatter communication in biosensing ultrasonic implants,” *IEEE Transactions on Biomedical Circuits and Systems*, vol. 14, no. 6, pp. 1381–1392, 2020.

[15] C. Chen, Z. Wen, J. Shi, X. Jian, P. Li, J. T. W. Yeow, and X. Sun, “Micro triboelectric ultrasonic device for acoustic energy transfer and signal communication,” *Nature Communications*, vol. 11, no. 1, p. 4143, 2020. [Online]. Available: https://doi.org/10.1038/s41467-020-17842-w

[16] T. C. Chang, M. Wang, and A. Arbabian, “Multi-access networking with wireless ultrasound-powered implants,” in *2019 IEEE Biomedical Circuits and Systems Conference (BioCAS)*, 2019, pp. 1–4.

[17] M. L. Wang, T. C. Chang, and A. Arbabian, “Ultrasonic implant localization for wireless power transfer: Active uplink and harmonic backscatter,” in *2019 IEEE International Ultrasonics Symposium (IUS)*, 2019, pp. 818–821.

[18] Y. Zhang and K. L. Shepard, “A 0.6-mm2 powering and data telemetry system compatible with ultrasound b-mode imaging for freely moving biomedical sensor systems,” in *2019 IEEE Custom Integrated Circuits Conference (CICC)*, 2019, pp. 1–4.

[19] M. J. Weber, Y. Yoshihara, A. Sawaby, J. Charthad, T. C. Chang, and A. Arbabian, “A miniaturized single-transducer implantable pressure sensor with time-multiplexed ultrasonic data and power links,” *IEEE Journal of Solid-State Circuits*, vol. 53, no. 4, pp. 1089–1101, 2018.

[20] S. H. Song, A. Kim, and B. Ziaie, “Omnidirectional ultrasonic powering for millimeter-scale implantable devices,” *IEEE Transactions on Biomedical Engineering*, vol. 62, no. 11, pp. 2717–2723, 2015.

[21] F. Mazzilli and C. Dehollain, “184 mu w ultrasonic on-off keying/amplitude-shift keying demodulator for downlink communication in deep implanted medical devices,” *Electronics Letters*, vol. 52, no. 7, pp. 2. 502–503, 2016. [Online]. Available: http://infoscience.epfl.ch/record/219349

[22] P. J. Larson and B. C. Towe, “Miniature ultrasonically powered wireless nerve cuff stimulator,” in *2011 5th International IEEE/EMBS Conference on Neural Engineering*, 2011, pp. 265–268.

[23] M. M. Ghanbari, D. K. Piech, K. Shen, S. Faraji Alamouti, C. Yalcin, B. C. Johnson, J. M. Carmena, M. M. Maharbiz, and R. Muller, “A sub-mm3 ultrasonic free-floating implant for multi-mote neural recording,” *IEEE Journal of Solid-State Circuits*, vol. 54, no. 11, pp. 3017–3030, 2019.

[24] D. K. Piech, J. E. Kay, B. E. Boser, and M. M. Maharbiz, “Rodent wearable ultrasound system for wireless neural recording,” in *2017 39th Annual International Conference of the IEEE Engineering in Medicine and Biology Society (EMBC)*, 2017, pp. 221–225.

[25] J. Charthad, T. C. Chang, Z. Liu, A. Sawaby, M. J. Weber, S. Baker, F. Gore, S. A. Felt, and A. Arbabian, “A mm-sized wireless implantable device for electrical stimulation of peripheral nerves,” *IEEE Transactions on Biomedical Circuits and Systems*, vol. 12, no. 2, pp. 257–270, 2018.

[26] J. Charthad, S. Baltsavias, D. Samanta, T. C. Chang, M. J. Weber, N. Hosseini-Nassab, R. N. Zare, and A. Arbabian, “An ultrasonically powered implantable device for targeted drug delivery,” in *2016 38th Annual International Conference of the IEEE Engineering in Medicine and Biology Society (EMBC)*, 2016, pp. 541–544.

[27] S. Baltsavias, W. Van Treuren, M. J. Weber, J. Charthad, S. Baker, J. L. Sonnenburg, and A. Arbabian, “In vivo wireless sensors for gut microbiome redox monitoring,” *IEEE Transactions on Biomedical Engineering*, vol. 67, no. 7, pp. 1821–1830, 2020.

[28] F. Mazzilli, C. Lafon, and C. Dehollain, “A 10.5 cm ultrasound link for deep implanted medical devices,” *IEEE Transactions on Biomedical Circuits and Systems*, vol. 8, no. 5, pp. 738–750, 2014.

[29] C. Shi, T. Costa, J. Elloian, Y. Zhang, and K. L. Shepard, “A 0.065-mm3 monolithically-integrated ultrasonic wireless sensing mote for real-time physiological temperature monitoring,” *IEEE Transactions on Biomedical Circuits and Systems*, vol. 14, no. 3, pp. 412–424, 2020.

[30] M. L. Wang, T. C. Chang, T. Teisberg, M. J. Weber, J. Charthad, and A. Arbabian, “Closed-loop ultrasonic power and communication with multiple miniaturized active implantable medical devices,” in *2017 IEEE International Ultrasonics Symposium (IUS)*, 2017, pp. 1–4.

[31] B. C. Johnson, K. Shen, D. Piech, M. M. Ghanbari, K. Y. Li, R. Neely, J. M. Carmena, M. M. Maharbiz, and R. Muller, “Stimdust: A 6.5mm3, wireless ultrasonic peripheral nerve stimulator with 82% peak chip efficiency,” in *2018 IEEE Custom Integrated Circuits Conference (CICC)*, 2018, pp. 1–4.

[32] D. K. Piech, B. C. Johnson, K. Shen, M. M. Ghanbari, K. Y. Li, R. M. Neely, J. E. Kay, J. M. Carmena, M. M. Maharbiz, and R. Muller, "A wireless millimetre-scale implantable neural stimulator with ultrasonically powered bidirectional communication," *Nature Biomedical Engineering*, vol. 4, no. 2, pp. 207–222, 2020. [Online]. Available: https://doi.org/10.1038/s41551-020-0518-9

[33] Y.-S. Luo, J.-R. Wang, W.-J. Huang, J.-Y. Tsai, Y.-F. Liao, W.-T. Tseng, C.-T. Yen, P.-C. Li, and S.-I. Liu, "Ultrasonic power/data telemetry and neural stimulator with ook-pm signaling," *IEEE Transactions on Circuits and Systems II: Express Briefs*, vol. 60, no. 12, pp. 827–831, 2013.

[34] D. Neren, M. D. Johnson, W. Legon, S. P. Bachour, G. Ling, and A. A. Divani, "Vagus Nerve Stimulation and Other Neuromodulation Methods for Treatment of Traumatic Brain Injury," *Neurocritical Care*, vol. 24, no. 2, pp. 308–319, 2016. [Online]. Available: https://doi.org/10.1007/s12028-015-0203-0

[35] H. Dinis, I. Colmiais, and P. M. Mendes, "Extending the Limits of Wireless Power Transfer to Miniaturized Implantable Electronic Devices," *Micromachines*, vol. 8, no. 12, 2017. [Online]. Available: https://www.mdpi.com/2072-666X/8/12/359

[36] A. Ben Amar, A. B. Kouki, and H. Cao, "Power Approaches for Implantable Medical Devices." *Sensors (Basel, Switzerland)*, vol. 15, no. 11, pp. 28 889–28 914, nov 2015.

[37] J. Hornberger, K. Kumar, E. Verhulst, M. A. Clark, and J. Hernandez, "Rechargeable Spinal Cord Stimulation Versus Nonrechargeable System for Patients With Failed Back Surgery Syndrome: A Cost-Consequences Analysis," *The Clinical Journal of Pain*, vol. 24, no. 3, 2008. [Online]. Available: https://journals.lww.com/clinicalpain/Fulltext/2008/03000/Rechargeable{_}Spinal{_}Cord{_}Stimulation{_}Versus.10.aspx

[38] F. Duck and T. Leighton, "Frequency bands for ultrasound, suitable for the consideration of its health effects," *The Journal of the Acoustical Society of America*, vol. 144, no. 4, pp. 2490–2500, 2018. [Online]. Available: https://doi.org/10.1121/1.5063578

[39] W. D. O'Brien Jr, "Ultrasound-biophysics mechanisms," *Progress in biophysics and molecular biology*, vol. 93, no. 1-3, pp. 212–255, 2007. [Online]. Available: https://pubmed.ncbi.nlm.nih.gov/16934858https://www.ncbi.nlm.nih.gov/pmc/articles/PMC1995002/

[40] H. Shankar, P. Pagel, and D. Warner, "Potential Adverse Ultrasound-related Biological Effects: A Critical Review," *Anesthesiology*, vol. 115, no. 5, pp. 1109–1124, nov 2011. [Online]. Available: https://doi.org/10.1097/ALN.0b013e31822fd1f1

[41] K. E. Neumann D, "Chapter 11," in *Ultrasound Medical Imaging Systems: An Introductory Guide [Internet]*. Cham: Springer, 2018. [Online]. Available: https://www.ncbi.nlm.nih.gov/books/NBK546144/doi:10.1007/978-3-319-96520-8_11

[42] M. Helguera, “An introduction to ultrasound.” [Online]. Available: https://www.cis.rit.edu/research/ultrasound/ultrasoundintro/ultraintro.html

[43] V. T. Rathod, “A review of acoustic impedance matching techniques for piezoelectric sensors and transducers,” Jul 2020. [Online]. Available: https://www.ncbi.nlm.nih.gov/pmc/articles/PMC7411934/

[44] OpenStax, “Physics.” [Online]. Available: https://courses.lumenlearning.com/physics/chapter/17-7-ultrasound/

[45] M. Peisino, “Deeply implanted medical device based on a novel ultrasonic telemetry technology,” *Lausanne, EPFL*, 2013. [Online]. Available: http://infoscience.epfl.ch/record/186391

[46] Dance, *Diagnostic radiology physics: a handbook for teachers and students*. IAEA, 2014. [Online]. Available: https://www-pub.iaea.org/mtcd/publications/pdf/pub1564webnew-74666420.pdf

[47] 2021. [Online]. Available: https://www4.uwsp.edu/physastr/kmenning/Phys115/Link5-09_acoustic_impedance.pdf

[48] H. Krim and M. Viberg, “Two decades of array signal processing research: the parametric approach,” *IEEE Signal Processing Magazine*, vol. 13, no. 4, pp. 67–94, 1996.

[49] Wikipedia, “Beamforming,” Aug 2021. [Online]. Available: https://en.wikipedia.org/wiki/Beamforming

[50] L. Demi, “Practical Guide to Ultrasound Beam Forming: Beam Pattern and Image Reconstruction Analysis,” *Applied Sciences*, vol. 8, no. 9, 2018. [Online]. Available: https://www.mdpi.com/2076-3417/8/9/1544

[51] D. Seo, H.-Y. Tang, J. M. Carmena, J. M. Rabaey, E. Alon, B. E. Boser, and M. M. Maharbiz, “Ultrasonic beamforming system for interrogating multiple implantable sensors,” in *2015 37th Annual International Conference of the IEEE Engineering in Medicine and Biology Society (EMBC)*, 2015, pp. 2673–2676.

[52] R. Zemp and M. F. Insana, “Imaging with unfocused regions of focused ultrasound beams,” *The Journal of the Acoustical Society of America*, vol. 121, no. 3, pp. 1491–1498, mar 2007. [Online]. Available: https://pubmed.ncbi.nlm.nih.gov/17407886https://www.ncbi.nlm.nih.gov/pmc/articles/PMC2715557/

[53] O. T. Von Ramm and S. W. Smith, “Beam steering with linear arrays,” *IEEE Transactions on Biomedical Engineering*, vol. BME-30, no. 8, pp. 438–452, 1983.

[54] M. Mahmood, S. Mohammed, and S. Gharghan, “Ultrasound sensor-based wireless power transfer for low-power medical devices,” *Journal of Low Power Electronics and Applications*, vol. 9, p. 20, 07 2019.

[55] S. Vaezy, “Marketing clearance of diagnostic ultrasound systems and transducers,” 2019. [Online]. Available: https://www.fda.gov/media/71100/download

[56] N. Iliev and I. Paprotny, “Review and comparison of spatial localization methods for low-power wireless sensor networks,” *Sensors Journal, IEEE*, vol. 15, pp. 5971–5987, 10 2015.

[57] I. Culjak, Z. Lucev Vasic, H. Mihaldinec, and H. Dzapo, “Wireless body sensor communication systems based on uwb and ibc technologies: State-of-the-art and open challenges,” *Sensors*, vol. 20, no. 12, 2020. [Online]. Available: https://www.mdpi.com/1424-8220/20/12/3587

[58] D. M. Mills and L. S. Smith, “Real-time in-vivo imaging with capacitive micromachined ultrasound transducer (cmut) linear arrays,” in *IEEE Symposium on Ultrasonics, 2003*, vol. 1, 2003, pp. 568–571 Vol.1.

[59] B. T. Khuri-Yakub and O. Oralkan, “Capacitive micromachined ultrasonic transducers for medical imaging and therapy,” *Journal of micromechanics and microengineering : structures, devices, and systems*, vol. 21, no. 5, pp. 54 004–54 014, may 2011. [Online]. Available: https://pubmed.ncbi.nlm.nih.gov/21860542https://www.ncbi.nlm.nih.gov/pmc/articles/PMC3158704/

[60] Brenner, Firouzi, Stedman, and B. T. Khuri-Yakub, “Advances in capacitive micromachined ultrasonic transducers,” *Micromachines*, vol. 10, no. 152, p. 054004, apr 2019. [Online]. Available: https://doi.org/10.3390/mi10020152

[61] X. Zhang, Y. D. Cui, C.-M. J. Tay, and B. C. Khoo, “Ultrasound generated by alternating current dielectric barrier discharge plasma in quiescent air,” *Plasma Sources Science and Technology*, vol. 29, no. 1, p. 015017, jan 2020. [Online]. Available: https://doi.org/10.1088%2F1361-6595%2Fab5733

[62] N. Lamberti, G. Caliano, A. Iula, and A. S. Savoia, “A high frequency cMUT probe for ultrasound imaging of fingerprints,” *Sensors and Actuators A: Physical*, vol. 172, no. 2, pp. 561–569, 2011. [Online]. Available: http://www.sciencedirect.com/science/article/pii/S0924424711005528

[63] T. L. Szabo, “Chapter 5 - Transducers,” in *Szabo, Thomas L B T - Diagnostic Ultrasound Imaging: Inside Out (Second Edition)*. Boston: Academic Press, 2014, pp. 121–165. [Online]. Available: http://www.sciencedirect.com/science/article/pii/B9780123964878000057

[64] R. J. McGough, “Rapid calculations of time-harmonic nearfield pressures produced by rectangular pistons,” *Journal of the Acoustical Society of America*, vol. 115, no. 5, pp. 1934–1941, 2004.

[65] D. Chen and R. J. McGough, “A 2d fast near-field method for calculating near-field pressures generated by apodized rectangular pistons,” *Journal of the Acoustical Society of America*, vol. 124, no. 5, pp. 1526–1537, 2008.

[66] R. Sanders, “Sprinkling of neural dust opens door to electroceuticals,” Aug 2016. [Online]. Available: https://news.berkeley.edu/2016/08/03/sprinkling-of-neural-dust-opens-door-to-electroceuticals/